# Simulations of Narrow-Angle Tail Radio Galaxy Evolution and Shock Interactions

**A DISSERTATION**
**SUBMITTED TO THE FACULTY OF THE GRADUATE SCHOOL**
**OF THE UNIVERSITY OF MINNESOTA**
**BY**

**Brian John O'Neill**

**IN PARTIAL FULFILLMENT OF THE REQUIREMENTS**
**FOR THE DEGREE OF**
**Doctor of Philosophy**

**Thomas W. Jones, Advisor**

**August, 2019**

## Abstract

We present the results of three-dimensional magnetohydrodynamic (MHD) simulations of radio galaxy (RG) outflows interacting with active galaxy cluster environments. The goal of these simulations was to analyze the consequences of these interactions such that observations of cluster radio emission can provide a more effective proxy for understanding the dynamical states of intracluster media (ICM).

We conducted the first high-resolution numerical study dedicated to the evolution of a narrow-angle tail (NAT) RG utilizing 3D MHD and energy-dependent transport of cosmic ray electrons (CRe). We verify existing theoretical models of the jet bending process and, in an appendix, extend them into an empirical formalism that allows us to model the jet trajectories that develop from arbitrary jet-wind orientations. We observe that the early development of our NAT consists of an extended formation period, during which the evolving RG goes through a transient phase where it is more reminiscent of a more gently bent wide-angle tail RG. Once the jets are fully bent, we note the jet trajectories do not remain static, but episodically "flap" in response to instabilities that develop in the surrounding ICM wind. This occasional disruption of the jets enhances magnetic fields via dynamical stretching, and is critical to the state of the plasma in the tails that develops. Synthetic observations show that once plasma released early in the NAT's evolution has faded, the observed morphology of the NAT is very nearly steady-state with a roughly constant brightness distribution and a steady, self-similar, curved integrated spectrum.

We then used the evolved NAT we created to run multiple simulations to explore the interactions between the tail plasma and shock fronts characteristic of those generated by a major cluster merger. Our primary motivation in conducting these simulations is to explore the possibility that CRe populations recently released from a NAT could be seed relativistic electrons necessary to explain observations of radio relics. We analyze the character the shock front develops within our simulated tails with a theoretical treatment based on a Riemann problem analysis. We note the development of vortical motions induced by the shock passage through the low-density plasma of the tails, and the resulting magnetic field amplification over and above amplification from shock

compression. We examine synthetic observations of our shocked tails and compare to common properties of emission from radio relics.

# Contents

# List of Tables

# List of Figures

# Chapter 1

# Introduction

## 1.1 Galaxy Clusters and the Intracluster Medium

The current canonical cosmological model achieved wide consensus about twenty years ago, and explains well the large-scale evolution of the Universe from inception in the Big Bang to the structure and accelerating expansion observed in the present Universe. Dubbed the Λ-CDM model, it describes how the force of gravity, dominated by the distribution of dark matter, condenses mass from the quantum fluctuations seeded in the primordial soup of particles into the galaxy clusters, cosmic filaments and voids we see today. As a consequence of cold dark matter (i.e., nonrelativistic; the "CDM"), galaxy clusters form via a hierarchical, bottom-up scenario clustering around the primordial fluctuations, with smaller systems merging into larger and larger ones. Consequently, the massive clusters in the present Universe are the product of many mergers, and structure formation is an on-going, observable process. This general picture is largely confirmed by large-scale, cosmological simulations (see, e.g., the IllustrisTNG project; Nelson et al. 2019).

Rich clusters of galaxies are located at the intersection of cosmic filaments and host 100's to $\sim 1000$ member galaxies. Such clusters are the largest and most massive gravitationally bound structures in the Universe, with radii in excess of a megaparsec ($\lesssim 10^{25}$ cm) and masses approaching $\sim 10^{15}$ $M_\odot$. Baryonic matter accounts for on the order of $\sim 10\%$ of the mass in clusters, with the vast majority of that baryonic matter

($\sim 90\%$) distributed throughout the cluster in a hot ($T \gtrsim 1$ keV), diffuse ($n \sim 10^{-2}$ - $10^{-4}$ cm$^{-3}$) plasma called the intracluster medium (ICM). The high temperatures in the ICM result from sitting deep in the cluster's dark matter-dominated gravitational well and the dissipation of energy from the merger history of the cluster via shock heating. Cluster mergers are the most energetic events in the Universe aside from the Big Bang itself, releasing up to $\sim 10^{64}$ ergs of gravitational potential energy on Gyr timescales. Most of this energy is dissipated via low-Mach number shocks that heat the plasma and generate turbulent flows in the ICM. Accretion of dark and baryonic matter from cosmic filaments along with energetic outflows from starburst galaxies and active galactic nuclei (AGN) can also drive motions in the ICM. In between major energetic releases, galaxies and diffuse matter virialize and the ICM plasma cools radiatively. Clusters therefore exhibit a range of dynamical states from "relaxed" to "active".

The high temperatures in the ICM cause the plasma to emit thermal bremsstrahlung (German for "braking radiation") in the X-ray part of the spectrum. This type of radiation is also known as "free-free emission" as it takes place in an ionized plasma and results from a free particle, an electron usually, scattering off the electric field of an ion but remaining free after the interaction, emitting a photon in the process. Galaxy clusters are extremely luminous in X-rays, with emitting powers up to $\sim 10^{45}$ erg s$^{-1}$, allowing us to directly observe the ICM plasma. Observations of thermal X-rays have provided most of what we know of the dynamics of the ICM. Total X-ray luminosities provide a proxy for the mass of the ICM, especially when combined with spectral information, and in bright, low-redshift clusters X-ray brightnesses can reveal distributions of density, temperature and entropy.

Structures $\gtrsim 100$ kpc such as shocks, cold fronts and AGN-inflated cavities can be identified in X-ray brightness distributions, but smaller scale features in the ICM are generally undetectable. Additionally, the emissivity of thermal bremsstrahlung is proportional to the square of the local ICM density, so the strength of X-ray emission decreases rapidly in the periphery of galaxy clusters. X-ray resolving capability is not going to dramatically improve anytime soon, so developing new tools is necessary for gaining further understanding of the physics of the ICM. Clusters are frequently host to nonthermal radio synchrotron emission, from the radio-bright outflows of AGN embedded in the ICM or from diffuse, extended emission in the ICM itself, and with the

advent of arrays like LOFAR, $\sim$ kpc scale structures at cosmological distances can be resolved across a broad range of the radio spectrum. Cluster radio emission therefore offers a potential means of studying ICM dynamics on smaller scale.

## 1.2 Radio Galaxy Outflows

The primary engine of an AGN is widely accepted to be energy released by matter accreting onto the supermassive black hole at the center of the host galaxy. Emission from AGN has been observed across the electromagnetic spectrum from radio to gamma rays. Radio-loud AGN are also referred to as radio galaxies (RG), and their outflows consists of hot, magnetized plasma populated by relativistic cosmic ray electrons (CRe). The source of their radio emission is synchrotron radiation released by relativistic electrons gyrating about magnetic fields. The radio-bright plasma released by AGN is collimated into bipolar jets. When RG sit in quiescent environments, they can be seen to deposit their energy into what theoretically should be symmetric lobes. The low-density, hot plasma released by the RG inflates bubbles in the host galaxy cluster that can appear as cavities of reduced X-ray emission compared to the surrounding, denser ICM. Outflows from AGN can also affect global ICM properties, depositing momentum, energy, magnetic fields and cosmic rays.

Outflows from RGs are also observed to respond to bulk flows in the ICM. If a persistent, asymmetric ram pressure acts on a RG as a result of winds, the host galaxy's orbital motion or a combination of the two, the plasma and CRe that might have inflated radio lobes is carried downstream and the source may appear as a "head-tail" RG, with the host galaxy at the head and the outflows swept back in a tail or two discernible tails. If the ram pressure acts perpendicular, or nearly so, to the RG's jet axis, the resulting outflows may appear as a wide-angle tail (WAT), with gently bent tails of radio plasma emanating from the RG source, or as a narrow-angle tail (NAT), where the jets are strongly bent into practically parallel tails. Presumably, the difference that gives rise to a WAT or a NAT structure is the intensity of that ram pressure. The basic theoretical picture of the ram pressure bending of a jet has been understood for decades (Begelman et al., 1979; Jones & Owen, 1979) and has been confirmed numerically many times (e.g., Williams & Gull 1984; Balsara & Norman

1992), but an in-depth numerical investigation of the formation and evolution of a NAT in high resolution utilizing 3D magnetohydrodynamics (MHD) with self-consistent energy transport of CRe populations does not yet exist in the literature.

## 1.3 Diffuse Radio Emission in the Intracluster Medium

An ever growing number of galaxy clusters are known to host diffuse radio emission that does not appear directly tied to a particular RG. Observations of synchrotron radio emission imply the presence of magnetic fields with strengths of $\sim 0.1$ to a few $\mu$G and $\gtrsim 1$ GeV CRe. These sources frequently appear extended with physical sizes up to megaparsec scales. The long diffusion times across such distances ($\gtrsim 1$ Gyr) and relatively short radiative lifetimes ($\sim 100$ Myr) require in situ acceleration mechanisms to sustain observed sources. Many (but not all) diffuse radio sources in clusters are easily sorted into two categories: radio halos and radio relics. Both of these classes tend to be correlated with active galaxy clusters.

Radio halos are sources with regular morphology that are generally co-located with the thermal X-ray emission of the ICM, though so-called mini-halos also are observed which tend to be confined more toward the cluster core. The emission associated with radio halos generally have relatively steep integrated spectral indices and has no significant polarization. The existence of mini-halos in contrast to giant radio halos has led to proposals that they represent a transitory stage, i.e., they represent a stage in evolution in between an inactive state and a fully developed giant radio halo. The radiation from radio halos requires the production of relativistic CRe throughout the vast volume of the ICM. Two primary scenarios for the source of these CRe have been debated on for years, each with their own set of problems.

The hadronic model presumes that cosmic ray protons, with significantly longer lifetimes than CRe, are produced en masse by shocks or AGN, diffuse throughout the ICM, and collide with thermal protons producing pions which decay into relativistic leptons that emit synchrotron. The most significant problem with the hadronic model is the necessary level of pion production would also generate observable levels of gamma rays in clusters that host radio halos, like the Coma cluster. The lack of gamma ray observations from Coma in particular, a massive, nearby cluster with a bright radio

halo, places very tight constraints on this model. Models based on second-order Fermi acceleration (Fermi-II) tend to be favored over purely hadronic models. In these models CRe are energized by scattering off magnetic perturbations driven by MHD turbulence, perhaps induced by merger activity. Fermi-II is a stochastic process, so the CRe diffuse in momentum space with a slight preference towards gaining momentum. Since it is based on a random process, MHD turbulence-based models are inefficient, particularly in accelerating electrons from the thermal plasma to relativistic energies. The primary issue is thus the source of mildly relativistic seed electrons for the Fermi-II process. Among the potential sources, AGN outflows may again prove important. CRe electrons released by RGs and then cooled radiatively to mildly relativistic energies (e.g., $\sim$ 50 Mev) can persist in the ICM for a few Gyr, and could provide a fossil population to be reaccelerated by MHD turbulence.

Radio relics tend to be elongated, thin sources frequently found in the periphery of galaxy clusters. They often emit radiation with relatively flatter spectra that is strongly polarized. A number of radio relics have been found to coincide with shock fronts identified in ICM X-ray emission. This, along with their morphology leads to the natural presumption that the CRe responsible for the radio emission are energized at the shock front by diffusive shock acceleration (DSA), a form of the first-order Fermi process. Multiple radio relics have been identified in pairs on opposite sides of a merging system of clusters, which would be expected for an ideal binary merger system where opposing shock fronts would propagate back into each ICM from the point of contact. A number of theoretical problems in explaining radio relic observations do still exist. The energy spectrum of a particle population produced by DSA is a function of the strength of the shock involved, and large discrepancies exist in several relics between the Mach numbers required by radio spectral properties and the Mach numbers measured via X-ray observations. As well, most relics appear in the outskirts of galaxy clusters where plasma densities are low, and theoretically the weak shocks predicted from merger events should have relatively low efficiency in accelerating electrons from the thermal population. The exceptional brightness of many observed relics strains the plausibility that CRe necessary were injected into the relativistic population from the thermal pool by weak merger shocks. Moreover, the relative scarcity of radio relics compared to the number expected based on the theoretical frequency of edge-on merger shocks in

the local Universe, in addition to observations of X-ray shocks with no coincident radio emission suggests that a shock alone is not enough to generate a radio relic. The presence of cooled, fossil populations of CRe can address some of these issues, and the natural tendency of a NAT to spread CRe over an extended area of the ICM makes the outflows of a recently active NAT an obvious candidate for seed electrons to be reaccelerated by a merger shock.

# Chapter 2

# A Fresh Look at Narrow-Angle Tail Radio Galaxy Dynamics, Evolution and Emissions

*Submitted to The Astrophysical Journal by Brian J. O'Neill, T. W. Jones, Chris Nolting & P. J. Mendygral*

**Abstract**

We present a numerical study of the development of a narrow-angle tail (NAT) radio galaxy (RG). Utilizing a three-dimensional magnetohydrodynamic simulation with cosmic ray electrons, we follow the formation and evolution of a NAT from the inception of a bipolar jet RG in a persistent crosswind through hundreds of Myr of steady jet activity. We confirm well-known theoretical models of the jet bending dynamic, while noting early in its development that our NAT has a phase when the morphology is reminiscent of a wide-angle tail RG. Once bent, we observe the jets to remain internally stable, but to be regularly driven unstable and disrupted by external disturbances induced in the wind by the NAT itself. The disruption process enhances magnetic fields in the jets and their effluence. Disrupted jet plasma is heterogeneously mixed with denser wind plasma, yielding patchy, filamentary tails that grow longer at a rate greater than the wind speed.

Such fast tail extension could, for example, allow NAT tails to overtake extraneous ICM features, such as shocks and shear layers, downwind of where the tails first form. Those events, in turn, could generate enhanced radio emissions within the ICM features themselves that do not follow geometrical extension of the tails past the encounter. Analysis of synthetic radio observations reveals an extended time period once the NAT has developed in which it displays a nearly steady-state morphology with integrated fluxes that are roughly constant along with a self-similar, curved integrated spectrum. In an Appendix, we outline a simple empirical formalism including explicit jet trajectories that extends the classic jet bending model to arbitrary jet-wind orientations.

## 2.1 Introduction

Radio galaxies (RGs) are jet powered, "radio mode" manifestations of active galactic nuclei (AGNs) commonly found at both low and high redshift in a variety of astrophysical environments from voids to rich galaxy clusters. Although RG jets at their sources (super massive black holes in the centers of galaxies) should physically be bipolar and nearly axisymmetric, they frequently appear on kpc scales and beyond to be obviously distorted from this morphology (e.g., Garon et al., 2019). One of the common distorted forms shows them bent into so-called "head-tail" (HT) shapes with the AGN anchoring the head (e.g., Burns et al., 1979). Often these HT sources appear roughly "C" or "U" shaped with extended, "twin-tailed" morphologies. In case the twin tails asymptote to roughly parallel trajectories away from the head they are labeled "narrow-angle tail" (NAT) RGs (Rudnick & Owen, 1977). Our purpose in this paper is to examine in some detail the dynamical elements that lead to the NAT morphology and to explore in simple terms potentially observable behaviors that might help to isolate the essential underlying physics.

NAT morphologies have long been modeled as the consequence of ram pressure from a crosswind, $\rho_w v_w^2$, producing a transverse pressure force that deflects the AGN jets "downwind" (Begelman et al., 1979; Jones & Owen, 1979). Here $\rho_w$ is the density of the wind, while $v_w$ is the transverse velocity of the wind relative to the AGN jet.

The crosswind may represent motion of the AGN host galaxy through its external environment, "weather" motions within that environment, or a combination of the two. The detailed bending dynamics depends, for instance, on whether a wind interacts directly with the jet, or, perhaps, the jet responds to a strong ambient pressure gradient induced by a wind or some other large scale ambient structure (e.g., Jones & Owen, 1979; Gan et al., 2017). Our focus here is on direct cross-wind interactions. The inclination between the wind and the jet velocity also influences the jet trajectory (see §A.1). However, a simple but effective cartoon of the bending comes from noting that the above ram pressure applied to an element of jet with longitudinal momentum density, $T_j$, channel radius, $r_j$ and differential length, $\delta\ell$ for a time interval, $\delta t$, transfers a transverse momentum to the jet element comparable to its original longitudinal momentum if $\delta t \sim r_j T_j/(\rho_w v_w^2)$. If the jet velocity is $v_j$, the jet element being deflected will have propagated a length $\ell_b \sim \delta t v_j$ during $\delta t$. This leads to a characteristic bending length, $\ell_b \sim r_j\ (T_j v_j)/(\rho_w u_w^2)$[1] (e.g., Jones et al, 2017). Written this way, the expression for $\ell_b$ would apply to a supersonic, relativistic mass dominated jet using $T_j = w_j \Gamma_j^2 v_j/c^2$, where $v_j$ is the (rest frame) jet enthalpy density, and $\Gamma_j$ is the Lorentz factor of the jet motion. For a Poynting-flux-dominated jet, $T_j = S_j/c^2$, where $S_j$ is the Poynting energy flux, while $v_j = c$. Then $\ell_b \sim r_j S_j/(c\rho_w v_w^2)$ (Gan et al., 2017). In the case of a non-relativistic, supersonic mass-dominated jet, such as we simulate in the present work, $T_j = \rho_j v_j$, which then leads to the commonly cited bending length, $\ell_b \approx r_j\ (\rho_j v_j^2)/(\rho_w v_w^2)$ (cf. also §A.1).

We note, as well, that the above derivation makes obvious the somewhat counter-intuitive fact that all of the momentum in the deflected jets transverse to their original propagation direction is derived from the transverse wind, even though the wind velocity can be orders of magnitude smaller than the jet velocity. That is, the wind effectively transfers momentum to the jets, concentrating it in order to deflect their motions. We shall see below that once the jets have been deflected, there remains a complex momentum exchange in both directions between the jets and the wind that embeds them.

For a non-relativistic, supersonic jet, it is trivial from the above derivation to show,

[1] The Appendix outlines a quantitative treatment of jet bending, revealing that, while $\ell_b$ provides a reliable bending length standard, the shape and full extent of a bent jet structure depend on additional dynamical factors.

using the standard Mach number relation $M^2 = v^2/c_s^2$, that when the jet and wind plasmas have the same adiabatic index, then $\ell_b \approx r_j(M_j^2 P_j)/(M_w^2 P_w)$, where $c_s$ is the sound speed. In this expression $M_j$ and $M_w$ are the internal jet and wind Mach numbers, while $P_j$ and $P_w$ are the respective pressures. If the jet is in pressure balance with the surrounding wind ($P_j = P_w$), it is thus evident that $\ell_b/r_j \sim (M_j/M_w)^2$. This last, simple scaling relation actually applies even if the jet is relativistic, provided one uses an appropriate, relativistic definition of the jet Mach number (e.g., Jones et al, 2017).

We point out that the only length scale needed to express wind-blown jet trajectories, so the physical scales of a RG formed in this way, is $\ell_b$. Thus, for example, the physical size of the RG in our simulation described in §2.2 & §2.3 could be scaled arbitrarily up or down for fixed ratio $\mathcal{M}_j/\mathcal{M}_w$, by resetting the jet radius, $r_j$. Alternatively, $\ell_b$, so the physical size and shape of the simulated RG, could be kept fixed while $r_j$ was rescaled, by varying $\mathcal{M}_j/\mathcal{M}_w \propto 1/\sqrt{r_j}$. One should keep in mind, however, that the associated dynamical time to reach a given stage in morphological development scales as $t_{dyn} = \ell_b/v_w$. So, if, for example, $\mathcal{M}_j/\mathcal{M}_w$ is kept fixed, while $\ell_b$ is reduced by reducing $r_j$, then $t_{dyn}$ is reduced in proportion to $r_j$. As we shall see below, bent jets become episodically unsteady with timescales related not only to $t_{dyn}$, but also to shorter times connected to the jets. Consequently, time-dependent structural details can be complex. In addition, since synchrotron spectral aging effects depend also on time, resizing details of the radio spectral distributions to match a structural rescaling would require adjusting the aging timescales the same as $t_{dyn}$.

The validity of the above "cross-wind-ram-pressure-bending" cartoon has been confirmed in multiple simulation studies involving non-relativistic plasma jets (e.g., Williams & Gull, 1984; Balsara & Norman, 1992; Loken et al., 1995; Heinz et al., 2006; Porter et al., 2009; Morsony et al., 2013; Jones et al, 2017). Simulations of Poynting-flux-dominated "magnetic tower" jets in dynamically active cluster media have shown analogous behaviors (Gan et al., 2017). "Aligned-wind"-based scenarios that lead to single-tailed HT sources have also been discussed in Jones et al (2017) and Nolting et al. (2019a) although those outcomes are outside the scope of the present paper.

While the basic picture of the ram pressure deformation model for twin tailed RGs is established, there is surprisingly little discussion in the literature exploring such important physics as the post-bending dynamical properties of the jets, the dynamical

characteristics of the tails themselves, or the behaviors of magnetic fields and relativistic cosmic ray electrons (CRe) that are responsible for radio emissions used to establish the nature of observed sources presumed to represent such events. Nor has there been much discussion of the dynamical transitioning from relatively straight jets to the final HT morphology. Our purpose in this paper is to explore a number of these physical behaviors in the specific context of NATs using high resolution (non-relativistic) MHD simulations incorporating energy-dependent transport of passive relativistic electrons (CRe), in order to provide a better basis for comparisons between observations and predicted model behaviors. Many of the same issues would apply qualitatively in some less-strongly-bent "wide-angle tail" (WAT) sources. In fact, we see below that our reference simulated NAT actually passes through a dynamical stage where it would be difficult to distinguish it from a WAT source.

As an extension of the NAT RG formation context that is our focus in this paper we mention that multiple, deformed RGs have been observed in the vicinity of X-ray, cluster merger shocks whose appearances suggest pre-shock HT morphologies (e.g., Bonafede et al., 2014; Shimwell et al., 2015). At the same time, the detailed surface brightness and spectral distributions of some giant radio relics (elongated diffuse radio sources in cluster peripheries), as well as the relative infrequency of these radio relics compared to expected presence of merger shocks, present an apparent theoretical problem if the relics represent CRe accelerated directly from ICM plasma by merger shocks (e.g., van Weeren et al., 2017). The plausible association of RG with some relics has, in fact, led to the suggestion that the relic radio emissions may be explained by populations of "fossil" CRe that were released by the RG, cooled radiatively, and then reaccelerated by the passing shock (e.g., Shimwell et al., 2015; Kang & Ryu, 2016). The highly elongated morphologies common to NATs make them obvious candidate RGs for such a scenario.

The present paper is part of a simulation study inspired by such possibilities as these. We analyze from simulations NAT formation in a steady crosswind. In a companion paper (O'Neill et al., 2019b) this NAT then provides initial conditions for simulations of cluster merger shocks overrunning NATs, providing probes of the NAT-cluster-relic scenario. In additional, related work, Nolting et al. (2019a) and Nolting et al. (2019b) study simulations of merger shocks running over lobed RGs formed in initially stationary ICMs.

The remainder of this paper is organized as follows: §2.2 details the simulation setup. In §2.3 , we analyze the dynamical evolution of our simulated NAT. In §2.4, we examine synthetic observations of our NAT. A summary of conclusions is presented in §2.5. We also include an Appendix (§A.1) that outlines a simple analytic dynamical model for ram pressure jet bending for arbitrary alignment between a crosswind and the AGN jet axis and compares it to 3D simulation results.

## 2.2 Simulation Details

The work presented here is based on 3D MHD simulations carried out with the WOMBAT code described in Mendygral (2011). The code utilizes the Roe-based, 2nd order accurate total variation diminishing scheme for solving the ideal non-relativistic MHD equations (MHDTVD) described by Ryu & Jones (1995) along with the "constrained transport" method of Ryu et al (1998) to maintain a divergence-free magnetic field.

Before listing specific physical model parameters we remind readers that, as outlined in the §2.1, dynamical lengths and times associated with morphological properties of our simulated flows can all be scaled relative to the bending length, $\ell_b$ and the dynamical time, $t_{dyn} = \ell_b/v_w$. In particular, $\ell_b$ can be made smaller or larger than the nominal value ($\approx 35$ kpc) that results from the parameters listed below. *As a reflection of this scalability, lengths and times given in figures, which are based on nominal parameter values to follow, are marked by* $^*$. In principle, it is also possible to rescale radiative loss timescales through adjustments in redshift and magnetic field strength normalization, although those adjustments would be more complex.

The simulation discussed below, which we label our "reference NAT simulation" used a Cartesian, Eulerian grid with cells, $\Delta x = 0.5$ kpc on a domain spanning $x, y, z = \pm 513, \pm 121.5, \pm 283.5$ kpc. This simulation domain was filled with a uniform, adiabatic, $\gamma = 5/3$, and unmagnetized ICM ("the wind") with density, $\rho_w = 5/3 \times 10^{-28}$ g cm$^{-3}$ and pressure, $P_w = 10^{-12}$ dyne cm$^{-2}$, (sound speed, $c_{s,w} = \sqrt{\gamma P_w/\rho_w} = 1000$ km s$^{-1}$). While a homogeneous, unmagnetized ICM is not very realistic, those attributes allow us to isolate cleanly behaviors explicitly related to the magnetized jets that form the NAT. The ICM wind was given an initial flow velocity, $\vec{v}_w$, along $\hat{x}$. The wind was maintained by continuous boundary conditions at the $-x$ domain boundary. For our reference run

$v_w = 900$ km s$^{-1}$ (Mach number, $\mathcal{M}_w = v_w/c_{s,w} = 0.9$).

The simulation also included a light, bidirectional, steady and supersonic jet pair oriented along the $\hat{z}$ axis (so orthogonal to the ICM wind) initialized at the start of the simulation ($t = 0$) and maintained until it was switched off towards the end of the simulation at $t = 546.5$ Myr. The jet flow was created in a stationary launch cylinder 24 grid cells, so 12 kpc, long. aligned with $\hat{z}$ (orthogonal to $\vec{v}_w$) and centered at position $(-390, 0, 0)$ kpc. Plasma conditions were maintained inside the cylinder in pressure equilibrium with its surroundings ($P_j \approx P_w$) and emerging as collimated, supersonic flow from each end. The outer radius of the launch cylinder was 4.5 kpc, including a 3 cell, coaxial "transition collar" to the ambient conditions. Reflecting boundaries for magnetic field and velocity were applied to the periphery of the launch cylinder.

The jet plasma (adiabatic index, $\gamma = 5/3$) in this simulation emerged with density and velocity, $\rho_j = 10^{-2}\rho_w$ and $v_j = 2.5 \times 10^4$ km s$^{-1}$, giving an internal, emergent jet Mach number, $\mathcal{M}_j = 2.5$. Tests of these jets analogous to those discussed in §A.1 established that their dynamics matched jets with the same density and velocity having radii, $r_j = 4.5$ kpc, so we, henceforth, use that radius for the jets in this simulation; i.e., $r_j$ matches the full radius of the launching cylinder. The resulting nominal jet bending length, $\ell_b \approx (2.5/0.9)^2 r_j \approx 7.7 r_j \approx 35$ kpc (matching the analytic trajectory discussed in §A.1). For use below we also define $r_{jc}$ as the jet core radius excluding the transition collar. In this case $r_{jc} = 3$ kpc.

A toroidal magnetic field, $B(r) = B_0(r/r_{jc})$ (uniform poloidal electric current inside $r_{jc}$) was maintained inside the launch cylinder, which transitioned to the ambient field (which could include previously launched jet fields) though the transition collar (there was a balancing effective return current inside the transition collar). The peak jet magnetic field strength, $B_0 = 1$ $\mu$G, yielded a fiducial $\beta_{pj} = 8\pi P_j/B_0^2 = 25$. The simulation incorporated a passively advected diagnostic scalar field, $C_j$, with $C_j = 1$ maintained inside the launch cylinder, but initialized to $C_j = 0$ elsewhere. In cells developing a mix of jet and ambient fluid $0 < C_j < 1$. Thus, $C_j$ represents the jet mass fraction in a given computational cell at a given time. Heuristically, $C_j$ acts like a jet pigment, whose intensity decreases as it becomes mixed with non-jet fluid. With this in mind, we, henceforth sometimes refer to $C_j$ as "jet color".

Passive, relativistic, cosmic ray electrons (CRe) injected from the jet launch cylinder

were transported in space and momentum ($p \approx E/c = \Gamma_e m_e c$) using the "coarse grained momentum volume" (CGMV) transport algorithm (Jones & Kang, 2005) for the CRe distribution function, $f(\vec{r}, p, t)$, in the range 5 MeV $\leq \Gamma_e m_e c^2 = pc \leq 85$ GeV, $10 \lesssim \Gamma_e \lesssim 1.7 \times 10^5$. The CRe momentum (energy) range was spanned by 8 uniform bins in $\ln p$. At launch, $f(p) \propto p^{-q_o}$, with $q_o = 4.5$. CRe adiabatic energy gains and losses were tracked, along with synchrotron and inverse Compton (iC) radiative losses off the CMB. CRe passing through shocks were subjected to standard test-particle diffusive shock acceleration (DSA), for which the equilibrium downstream electron distribution is a power law, $f \propto p^{-q_s}$, with slope $q_s = 4M_s^2/(M_s^2 - 1)$. Since the typical timescale for DSA in the energy range being tracked is $\sim$ yr (e.g., Brunetti & Jones, 2014), while simulation time steps, $\Delta t \sim \Delta x / v_{max} > 10^4$ yr, DSA was assumed to occur instantaneously at shock crossings. Shock strengths were measured at run time using methods similar to those presented in Miniati et al. (2001). The CRe spectrum in each momentum bin was set to $q = min(q_i, q_s)$, where $q_i$ is the distribution slope in that bin upstream of the shock. The CRe spectrum emergent from the jet launch cylinder matches that behind a shock of Mach number, $M_s = 3$. We note that except for a very small population needed to avoid numerical singularities, the ICM itself ($C_j = 0$) did not contain CRe. This simplification helps facilitate isolation of physics related to the jets themselves.

In order to track CRe iC losses off the CMB, it was necessary to fix the redshift, $z$, of the simulated RG. The iC and synchrotron losses are equal when the magnetic field is $B = B_{CMB} \approx 3.24(1+z)^2 \mu$G. In our simulations $z = 0.2$, for which $B_{CMB} \approx 4.67 \mu$G. Consequently, for the parameters outlined above iC losses usually, although not always, exceeded synchrotron losses.

The Appendix is focused on the dynamics of jet deflection by obliquely impacting winds. While primarily intended to outline a simple analytic model for jet bending, it presents results from multiple test simulations very similar to the reference case, but using somewhat smaller grids appropriate for their shorter dynamical times. The jet launch cylinder orientation, while remaining in the $x - z$ plane, was tilted for those simulations with respect to the wind flow at various angles, $0 < \theta_{ji} < 90°$. Additionally, ICM and jet parameters (e.g., densities and flow Mach numbers) were varied to confirm the general validity of analytic scaling relations and their dependence on $\ell_b$ derived in

§A.1.

## 2.3 NAT Evolution Overview

### 2.3.1 Dynamic Stages Outline

Our reference NAT RG is, by design, kept as simple as possible in order to help isolate core behaviors that will likely contribute in real-world situations, but can easily be obscured in complex settings. In that context, we note that the RG is powered by jets that remain on and unchanged for a prolonged time period and mention again that the jets (which are magnetized) penetrate an unmagnetized and homogeneous wind blowing orthogonally to the jet launching axis.

Obviously, if AGN activity is highly intermittent, the history is made more complex and the dynamical phases outlined below can be intermingled and even interacting. Such issues are outside our present scope. For introduction to NAT evolution in more complex wind environments see, e.g., Morsony et al. (2013), who simulated NAT formation in a dynamical galaxy group, or Porter et al. (2009), who simulated NAT formation in a moderately turbulent, magnetized, obliquely propagating ICM wind. The ICM turbulence and magnetization in the simulation reported in Porter et al. (2009) led to less distinct transition between the RG head and its tails and to enhanced tail radio emissions compared to what we see in the reference simulation, here, as one would expect. A wind more strongly turbulent, but turbulent on similar scales in comparison to the Porter et al. (2009) study, would possibly modify the forms of the bent jets in the RG head if the bending length, $\ell_b$, and the bending plane varied significantly within the head of the NAT, while the tails could become fatter and potentially more luminous, if, for instance the pre-existing and magnetized turbulence dominated motions within the tails (especially if the wind contained a population of CRe). Very much larger scale and long lasting pre-formed ICM turbulent structures could also lead to evident "external" radio features linking to the NAT if the encounters were "glancing", so did not disrupt those ICM structures. These more complex issues will be addressed in a future paper, but we do mention here the obvious point that the presence or absence of such features could possibly provide constraints on ICM turbulence properties.

The history of our steady jets interacting with a homogeneous crosswind to form

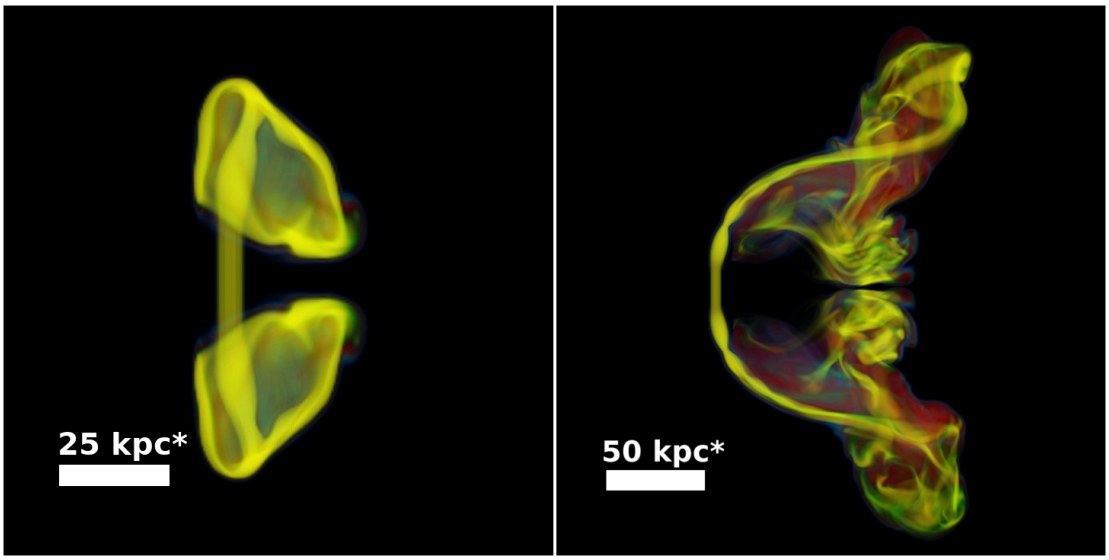


Figure 2.1 Volume rendering at early times of jet color, $C_j$, viewed along $\hat{y}$. Yellow identifies volume elements that are predominantly jet plasma followed by, in terms of decreasing mass fraction, green, red, and blue. Left: Close up at $t = 16.4$ Myr*. Distorted jet terminus plumes are evident. Right: $t = 98.4$ Myr*. The transition towards NAT morphology is clear, along with the plume structures bridging between the tails and remnants of the initial jet flapping event. The * in labels serves as a reminder that the nominal length (and time) scales can be increased or decreased by adjustment of the bending length, $\ell_b$.

a NAT can be divided into two distinct phases while the jets are active, followed by a third, post-activity, decay phase. The initial, first stage evolution begins as the light, but fast, AGN jets penetrate into the dense ICM and undergo deflection downwind by the crosswind flow as outlined in §2.1 and in somewhat more general terms in §A.1 (see also figures 2.1, 2.2), or potentially even within the host galaxy ISM embedded in the same wind (Jones & Owen, 1979). The ICM plasma in the downwind wakes of the transverse jets quickly becomes turbulent, even when the incident wind is not. By the time the jets have extended to lengths comparable to the nominal bending length, $\ell_b$, they show preliminary signs of transition towards NAT morphology, although that transformation turns out to be rather prolonged and complex.

The clearest initial signs of the transformation come before the jet trajectories themselves begin to resemble their eventual arcs. Specifically, as illustrated in figure 2.1, jet

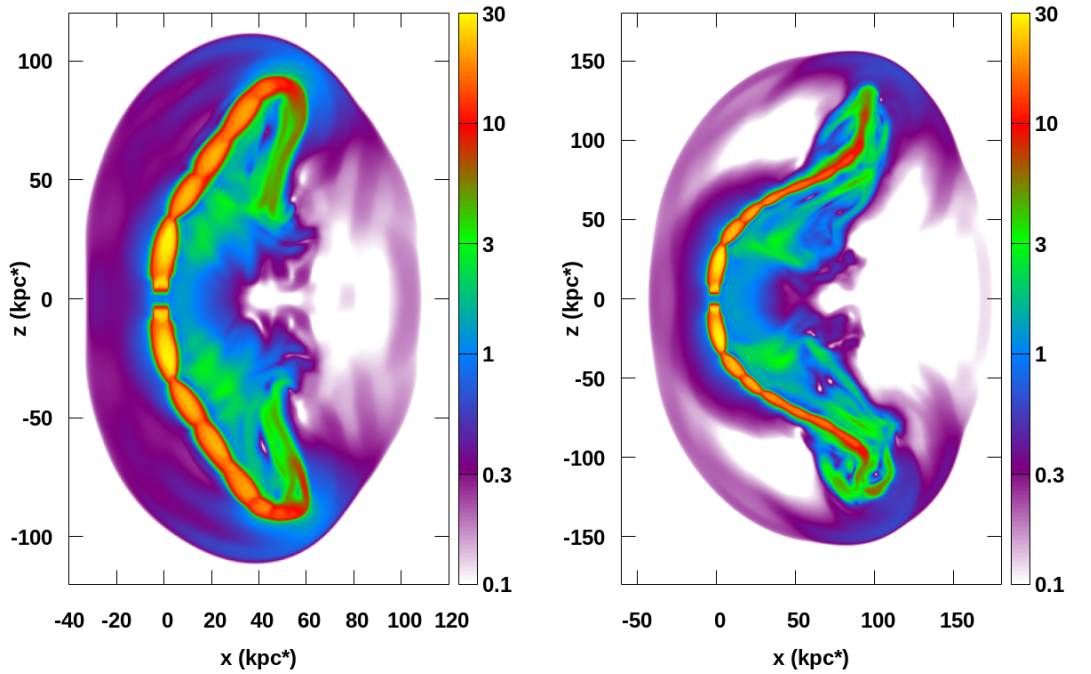


Figure 2.2 Flow velocity (in units of $v_w$) in the $x$-$z$ plane at y = 0 measured in the undisturbed wind rest frame during the so-called transition phase. Left: $t = 49.2$ Myr*. Right: $t = 82.0$ Myr*. The * in labels serves as a reminder that the nominal length (and time) scales can be increased or decreased by adjustment of the bending length, $\ell_b$.

plasma shed from each jet terminus is blown downwind, producing plume structures that eventually develop into distinctive and persistent NAT components. As the jets continue to extend, they actually undershoot their nominal equilibrium trajectory (they are less deflected than in their equilibrium trajectories). Subsequently, they abruptly "over correct" towards their equilibrium paths and are mostly pinched off (disrupted). This initiates long term, episodic "flapping" of the downwind jets that can become very large amplitude (figures 2.2, 2.3). When one of the jets is initially aimed upwind coming from its source, this trajectory over-correction-disruption event can be especially dramatic (see §A.1). Even in our reference simulation with jets launched orthogonally to the wind the consequence of the undershoot just described leads to transient transverse extents approaching 150 kpc ($t \sim 80$ Myr), compared to the nominal bending length, $\ell_b \approx 35$ kpc (see figure 2.2). The morphology at that stage is effectively that of a WAT. Subsequent jet disruptions after $t \gtrsim 100$ Myr (see figure 2.3) isolate these extensions as

the jets adjust towards the long-term NAT morphology. The remnants of these transition structures develop into distinctive vortex plumes at the end of each tail (see figure 2.9). As we see in §2.4, however, their radio emissions fade over time.

Over longer times the jet trajectories do average close to the simple analytic, equilibrium paths outlined in the Appendix; i.e., expected NAT morphologies develop. However, jet flapping/disruption events continue to punctuate the dynamical evolution of the tails so long as the jets remain active. Over time both the tails and embedded jets extend farther downwind (see figure 2.3).

As a preliminary insight into the long term tail dynamics we make the obvious but significant point here that for jets initially orthogonal to the wind (as in our reference simulation) virtually all of the momentum in the downwind-directed jet has been extracted from the wind. More generally, interaction between the jets and the wind in the head region transfers and concentrates wind momentum into the fast-moving jet plasma, which then transports that momentum downwind. The "stolen" momentum is eventually re-deposited in the tails downwind from where it is first extracted. Although on average the net momentum transfer should balance, as we shall see in §2.3.2, the plasma density in the tails is generally less than in the undisturbed wind. Consequently, the NAT tail plasma gets a net velocity boost out of the exchange. That is, the NAT tails are not passively advected in the wind, but actually propagate downwind faster than the wind. Our simulated scenario in this paper involves only a steady wind. *But, if, as in the scenario simulated by Nolting et al. (2019b), the wind generating the NAT is a post shock wind, a consequence of the NAT velocity boost can be that the NAT tails actually overtake the shock.* This, in fact, happens in the ICM-shock-generated NAT discussed in Nolting et al. (2019b). That, in turn could enable NAT magnetic fields and CRe to become engaged in physics associated with the ICM shock transition (e.g., diffusive shock acceleration).

Once the NAT morphology is fully developed, its structure can be spatially divided into distinct, dynamical regions. Proceeding from the AGN source into the tails these are: **(1)** the U-shaped coherent jet structure defining the head, **(2)** a low pressure, low density turbulent wake inside the "U", **(3)** a dynamical transition region connecting the head region jets to the extending tails, which we dub the "disruption zone", and within which the jets continue to be episodically disrupted, then reformed as they extend,

and finally, **(4)** the extending, heterogeneous and turbulent tails, which also connect to prominent plumes developed relatively early in the source evolution and discussed in the next section. Although those plumes form out of the transition towards NAT behavior, they persist in association with the tails until the end of our simulation. However, their radio emissions fade over time as the CRe within them age.

### 2.3.2 Jet Dynamics

#### Early Evolution

In simple terms a supersonic, AGN plasma jet behaves as a low density "beam" driving into the denser background ICM. In the case of a static ambient ICM, the jet plasma, after passing through a jet termination shock, would flow back around the propagating jet, displacing the ICM to form a classic, low density radio lobe. In the NAT context, with a strong ICM crosswind, the plasma emerging from the jet terminus is unable to form such a lobe. Initially, when the jets still propagate roughly straight and the terminal flow is across the incident wind, highly distorted "mushroom cap" terminal plasma plumes form as shown in figure 2.1[2] . Upwind portions of these terminal plumes are pressed against the jet. Some of the expelled plasma is entrained again in jet flow. Some of that becomes trapped just downwind, near the head of the source so long as the jets are active. The rest becomes incorporated into prominent, persistent vortex features creating a bridge-like structure between the two tails as NAT morphology develops (figures 2.1, 2.3). We will discuss in §2.4 synthetic radio observations of this structure. In short, it is relatively radio luminous as it first forms, but, because it becomes isolated from jet-provided fresh CRe, synchrotron emissions fade over time.

Propagation of the launched jets also generates a pair of merging bow shocks in the ICM, just as for a RG forming in a static ICM. In a static environment the combined, bounding "RG cocoon shock" would be roughly axisymmetric. That symmetry is broken in the NAT context, of course. Either way, the bow shock Mach numbers just beyond the jet termini roughly match the Mach number of the extension rate of the jet termini with respect to the local ambient medium. This depends, in turn, on the internal Mach number of the jet and the local ambient flow properties (e.g., Nolting et al.,

[2] See Nolting et al. (2019a) for the analogous analysis of jet propagation into a quasi-aligned ICM wind

2019a). On the other hand, the lateral portions of these shocks are generally weak, with Mach numbers only slightly more than unity (e.g., Jones et al, 2017). In the NAT reference simulation under examination here the wind velocity relative to the AGN is only slightly subsonic, $\mathcal{M}_w = 0.9$. Consequently, even before the jets are strongly bent downstream by the wind, the weak lateral shock structure barely propagates upwind from the AGN (the jet launch cylinder in the simulation), while it propagates downwind at roughly twice the wind speed in the AGN frame. Once the jet terminations are deflected downstream, the bow shock Mach number is substantially reduced by geometry alone. Jet-associated ICM shocks become largely indiscernible from other features in the ICM flow.

There also is an ICM bow wave upwind of the jet launch cylinder and the transverse jet portions. In the reference simulation, where $v_w$ is subsonic, this bow wave never becomes a shock, so does not establish a stationary standoff location. Immediately upwind of the launch cylinder the ICM compression remains $\sim 50\%$. In a more realistic setting, the ISM of the host galaxy might provide an obstacle roughly comparable to the launch cylinder in our simulation.

**Transition of the Jets Towards a NAT Configuration**

As outlined at the beginning of §2.3.1 the jets initially extend with somewhat less bending than predicted by the simple models utilizing an equilibrium bending length, $\ell_b$. But, they then adjust towards that trajectory, becoming unsteady, with episodic "flapping". As already noted, the scale and amplitude of jet flapping can substantially exceed the nominal bending scale, $\ell_b$. In the case of our reference simulation object, this transition phase includes a period when the RG morphology is essentially that of a WAT. As also noted above, the abrupt trajectory corrections associated with flapping are associated with jet disruption events; the jets become pinched where they bend sharply. The momentum within the pinched-off jet segments propagates inwards, towards the other jet flow region. On a timescale comparable to, or a bit less than the ICM sound crossing time between the two forming tails, the disrupted flow impacts the other jet, initiating a subsequent disruption event for that jet. In our reference simulation that time interval is $\sim 50$ Myr, which then roughly measures the interval between "flapping events" of each jet. In the reference simulation, where the two jet trajectories are

qualitatively similar, the jet flapping/disruption events occur at very roughly the same times for the two jets. On the other hand, for obliquely launched jets associated with the NAT formations outlined in §A.1, the two jet behaviors can be quite different. We mention this here especially in the context of transition towards the NAT morphology, although this behavior continues into the subsequent NAT phase of the source evolution.

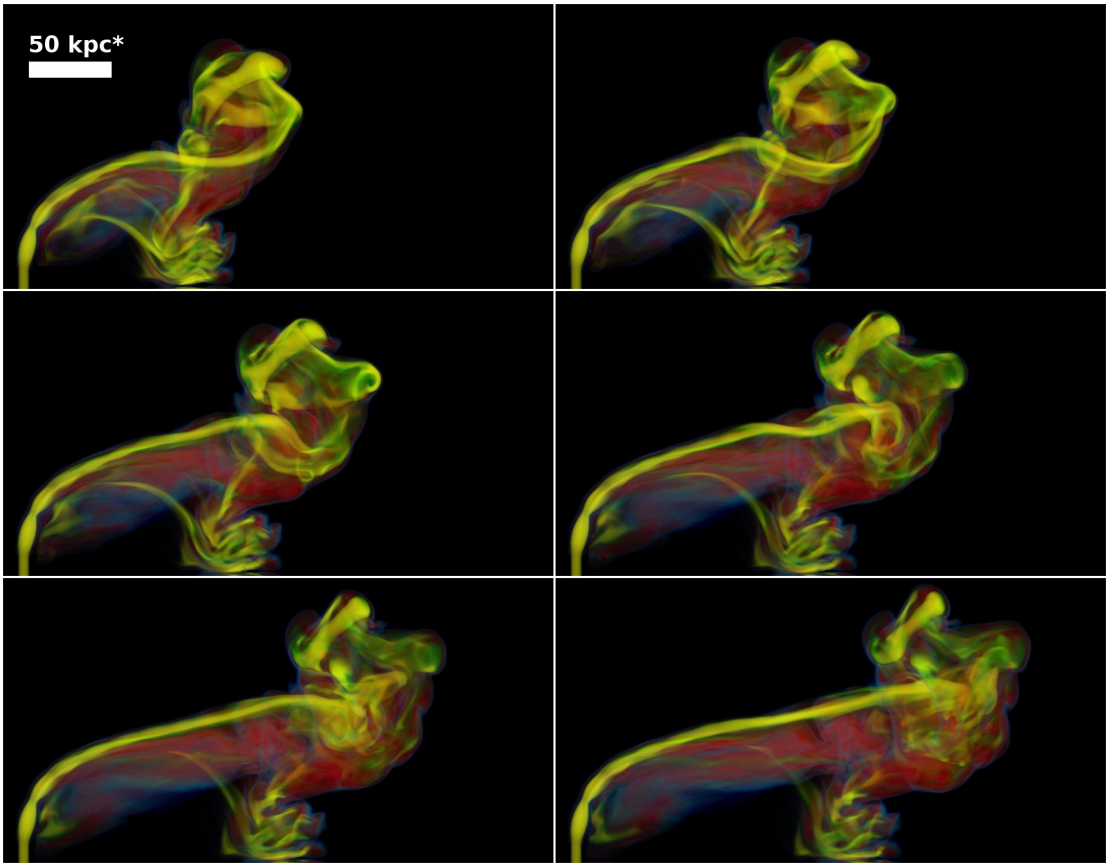


Figure 2.3 Volume renderings of jet color, $C_j$, demonstrating the sequence of a disruption event. The upper left image is at $t = 114.8$ Myr*, with successive images separated by 16.4 Myr*. So, the bottom right image corresponds to $t = 196.8$ Myr*. Color scale is the same as figure 2.1. The * in labels serves as a reminder that the nominal length (and time) scales can be increased or decreased by adjustment of the bending length, $\ell_b$.

**NAT Phase Jet Dynamics**

The above transition behaviors do ultimately lead to NAT morphologies in our simulations. We emphasize again that the episodic jet flapping and disruption events continue in the NAT phase. In fact, the disruption events are instrumental in defining the turbulent behaviors that develop in the tails. Roughly speaking the resulting outer turbulence scale in the tails is $\ell_t \sim \ell_b$ so in the reference simulation $\ell_t \sim 30$ kpc. The associated turbulent velocity is $\delta v \sim v_w$, giving a characteristic eddy time $\tau_{eddy} \sim \ell_t/v_w \sim (r_j/v_w)(M_j/M_w)^2$. In the reference simulation, $\tau_{eddy} \sim 35$ Myr. We mention in passing that turbulence in the wake region immediately downwind of the jets in the head region is driven on smaller scales closer to the jet diameter, and, although it does contribute to unsteady jet behaviors, does not appear to be their dominant driver.

There are two additional features of long term jet propagation worthy of mention here. First, our simulated jet flows expand as they emerge from the launch cylinder, then re-focus. This repeats along the jet quasi-periodically within the head region, leading to a series of steady and stationary, successively weaker "recollimation shocks" (analogous to "shock diamonds" in engineering contexts) that extend down each jet (e.g., Norman et al. (1982); Perucho (2013); Bodo & Tavecchio (2018)) (see also, e.g., figure 2.2, where these features appear as jet constrictions), In the synchrotron images in figures 2.8, 2.9, 2.10 and 2.11 the recollimation features show as "jet hotspots" in the source head region. The recollimation shocks closest to the source can be moderately strong. In the reference simulation the innermost recollimation shock Mach numbers, $\mathcal{M} > 3$, with $\mathcal{M} \sim 6$ on the jet axis. DSA in the strongest shock sections harden the spectra of CRe populations passing through them (see §2.3.4)[3] . Shocks further down the jets in this case, where the jet flow begins to deflect, are too weak (mostly $\mathcal{M} < 1.5$) to lead to significant DSA. We comment in passing that, although recollimation shocks are a common, natural occurrence in jet flows, they are typically associated with transitions within ambient conditions. In this simulation that transition comes at the end of the launch cylinder, while the analogous transition in a real RG would be on much smaller scales. Such a transition in the scales simulated here could in principle relate, for example, to jet emergence from the host galaxy ISM. We also mention that superficially

[3] Recall that the distribution slope of the CRe population emerging from the launch cylinder corresponds to DSA from a $\mathcal{M} = 3$ shock.

similar features on the scales relevant here might result from time variations in the jet flow velocity, although those would not be stationary.

### NAT Phase Tail Dynamics

Inherent to the nature of NAT tail formation, much of the AGN plasma becomes mixed with ambient, ICM plasma. That is evident in our reference simulation from jet color images in figures 2.1 and 2.3. Mixing comes about through a combination of three processes, beginning with intermittent jet disruption events that rapidly deposit the content of pinched jet segments. In addition to direct jet-ICM mixing from that, the turbulence driven by these events mixes plasma that continues to exit the termini of the active jets. Consequently, most mixing takes place in what we called the disruption zone, and most of the jet material is in volumes with intermediate jet color values, $C_j \sim 0.3 - 0.7$. Between disruption events, jets burrow further into the tails (e.g. figure 2.3), injecting momentum, magnetic flux and CRe. In the process they also populate the tails with clumps of more pristine jet plasma ($C_j \sim 1$). In addition, even as they propagate through quiescent environments, the jets entrain some ambient plasma through their boundaries. In our simulations that last entrainment is largely a consequence of numerical diffusion, although analogous, real jets are thought to entrain ambient plasma by, for example, jet surface instabilities (e.g., Bicknell, 1994; Laing & Bridle, 2008).

Together these processes cause the tails to become highly heterogeneous blends of ICM and jet plasma. In our reference simulation the ICM is unmagnetized and free of CRe, so these mixing processes are essential to seeding the NAT tails with magnetic fields and CRe responsible for its radio synchrotron emissions. The mass distribution in the NAT tails is also highly heterogeneous. This is evident in figure 2.4, which displays the projected mass density along $y$ through a 15 kpc thick slab centered on $y = 0$, just before the AGN jets turn off. That heterogeneous density distribution will play a prominent role when, in a subsequent paper in preparation O'Neill et al. (2019b), we study simulated interactions between this NAT and cluster merger shocks.

The lowest projected density regions visible in figure 2.4 highlight tail volumes of mostly jet material ($C_j \sim 1$), and reveal that, well downwind from where the jets become unsteady, substantial tail volumes are dominated by identifiable pinched off jet segments that here project areas $\gtrsim 10$ kpc wide and $\sim 50$ - 100 kpc long. As one would

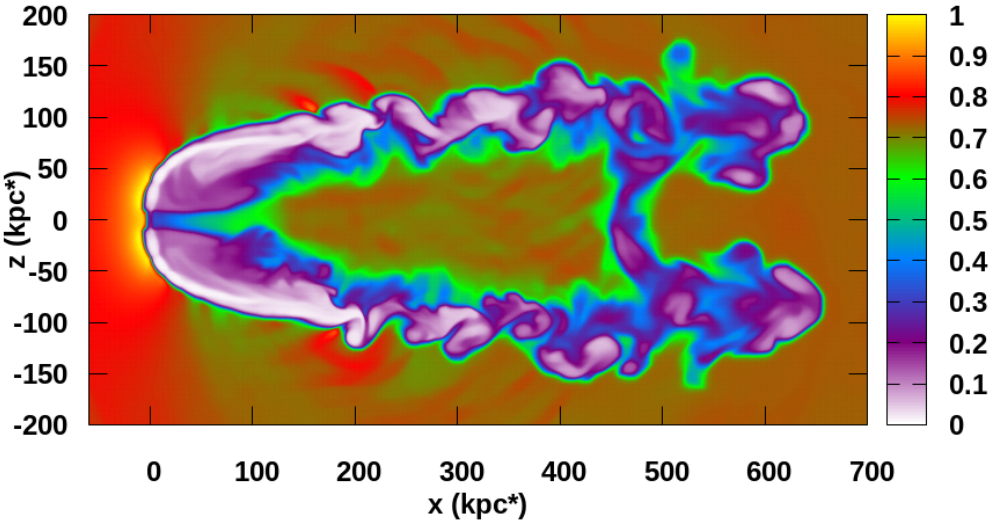


Figure 2.4 Projected mass density at $t = 541.1$ Myr* through a slab 15 kpc thick centered in $y$ on the simulation midplane. The projected mass density is scaled to the maximum value. In those units the undisturbed background ICM projected mass density $\approx 0.71$. The * in labels serves as a reminder that the nominal length (and time) scales can be increased or decreased by adjustment of the bending length, $\ell_b$.

expect, these features show obvious distortions derived from both jet flapping episodes and tail turbulence. On the other hand there is a generally positive column density gradient along each tail that reveals ongoing mixing between jet and ICM plasma. Also in figure 2.4 we can see a bridging channel between the two tails that is the outcome of the initial, transient plume described in §2.3.2. In addition and downstream (to the right) of that feature are the remnants of the early jet disruption underway in figures 2.1, 2.2 and 2.3. By the time of figure 2.4, iC radiative cooling has caused these early disruption features to become virtually invisible through radio emissions.

The density distribution evident in Figure 2.4 also provides a simple way to understand the point made in §2.3.2 that the NAT tails extend downwind at speeds greater than that of the driving wind, $v_w$; the tail plasma is not passively advected in the wind. The underlying physics alluded to there was that in the head regions of the source jets extract momentum from the wind as they are deflected downwind, then return that momentum downwind into the tails. The net momentum transfer should balance on average. But, since the density of the tail plasma is less than the density in the wind itself,

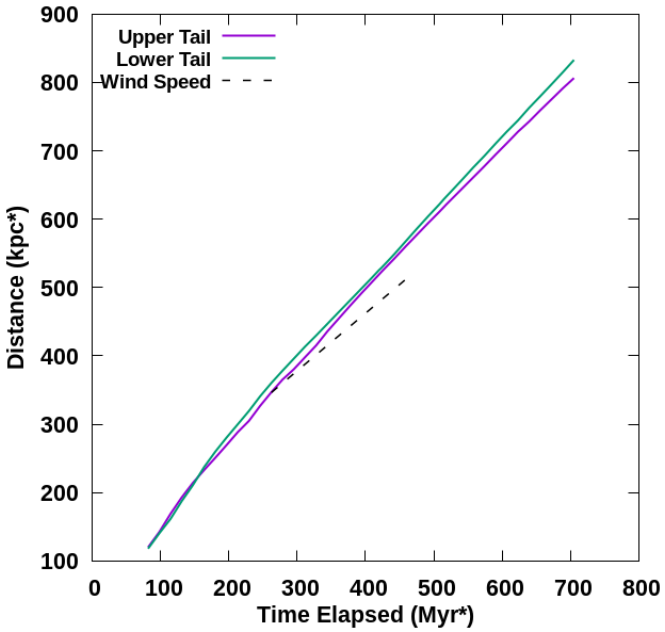


Figure 2.5 Distance (along $x$) vs time from the AGN to the end of each tail, compared with $x = v_w\ t$. The * in labels serves as a reminder that the nominal length (and time) scales can be increased or decreased by adjustment of the bending length, $\ell_b$.

the resultant downwind velocity of the tail plasma exceeds that of the wind. Quantitatively, the difference should depend on both the density contrast and the effective cross section ratio, so is not trivial to calculate. The outcome in our reference simulation is illustrated in figure 2.5, where we can see that the (mean) tail extension rate is $\sim 10\%$ faster than the background, wind flow[4] . As already mentioned, for a NAT formed in a post shock wind (Nolting et al., 2019b), significant consequences of this enhanced tail extension rate would likely include long term interactions between the initiating shock and the NAT tails, possibly leading to transfer of CRe from the tails to the shock. More generally, this would enable the NAT tails to overtake extraneous ICM features, such as shear layers akin to "sloshing fronts" and, conceivably, "light them up" by transferring CRe. Such events might account for some sharp bends that have been noted in NAT tails (e.g., Hoang et al., 2017).

[4] For analyses of this kind we define "tail plasma" as plasma with jet color $0.01 < C_j < 1$

Finally, we mention for use below that analysis of 2nd order velocity structure functions in the tails indicates that tail turbulence has a characteristic velocity of about half the wind speed ($\delta v \sim v_t \approx 0.5 v_w = 450$ km s$^{-1}$) with an outer scale roughly the jet bending length, $\ell_b \approx 35$ kpc. The eddy turnover time associated with this scale in this simulation is, therefore, $\tau_{eddy} \sim \ell_b / v_t \sim 80$ Myr . We do emphasize, however, that turbulence in the tails is neither homogeneous, nor steady.

### 2.3.3 Magnetic Field Dynamics

The magnetic field in our jet launch cylinder is toroidal and increases linearly in strength towards the cylinder perimeter with peak value, $B_0 \approx 1\mu$G. Upon emergence from the launch cylinder the magnetic field is governed by the magnetic induction equation. In the ideal MHD limit, that can be written

$$\frac{\partial \vec{B}}{\partial t} = \vec{\nabla} \times \left( \vec{v} \times \vec{B} \right). \tag{2.1}$$

Applying standard vector identities, $\nabla \cdot \vec{B} = 0$ and the mass continuity equation, $\nabla \cdot \vec{v} = -D \ln \rho / Dt$, this can be expressed simply in terms of Lagrangian time derivatives, $D/Dt = \partial/\partial t + \vec{v} \cdot \nabla$, as

$$\frac{D\vec{B}}{Dt} = \frac{D \ln \rho}{Dt} \vec{B} + (\vec{B} \cdot \nabla)\vec{v}. \tag{2.2}$$

The first RHS term in equation 2.2 accounts for plasma compression, while the second accounts for stretching of magnetic flux lines. Although both terms contribute to the evolution of the magnetic field in our simulation, the second, stretching term is usually predominant, especially during jet disruption. The distribution of magnetic energy in figure 2.6 at $t \sim 100$ Myr demonstrates the importance of this dynamic. The fast moving jets are put under great dynamical stress when their velocities change abruptly, and these stresses convert some of the jet's kinetic energy into magnetic energy. During the early dynamical phase, the rapidly extending jets experience larger stresses than later on, so the plumes that cap the ends of the tails contain strongly magnetized plasma (see right side of figure 2.1, figure 2.6).

In the ideal MHD limit the force equation of relevance to us, including the Maxwell

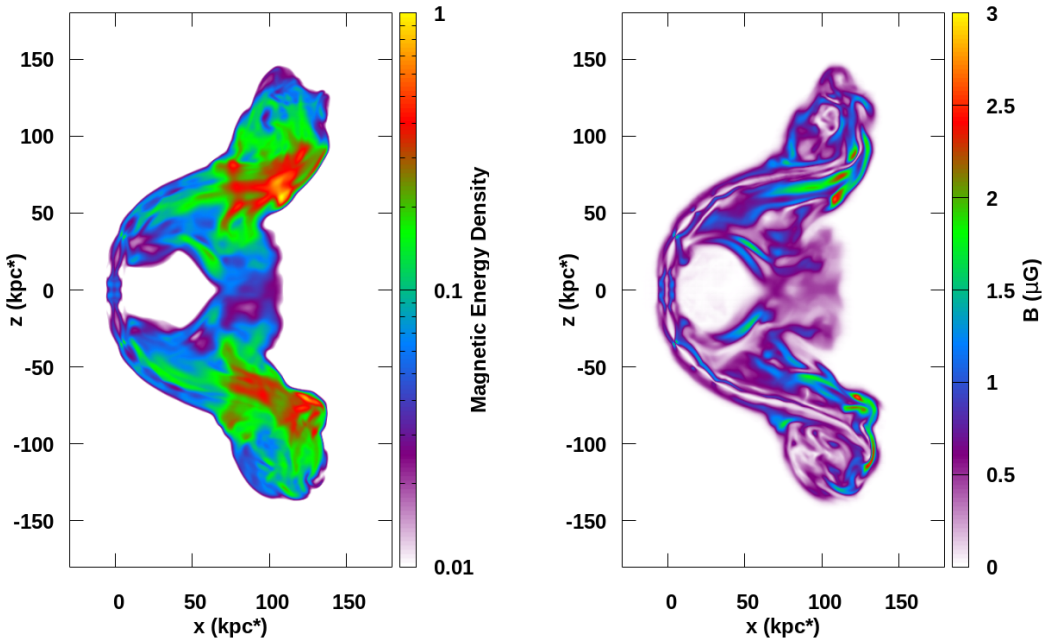


Figure 2.6 Magnetism at $t = 98.4$ Myr. Left: Projection along y of magnetic energy density (arbitrary units). Right: Plane ($y = 0$) slice of magnetic field strength ($\mu$G). The associated distribution of jet color, $C_j$, is displayed on the right side of figure 2.1. The * in labels serves as a reminder that the nominal length (and time) scales can be increased or decreased by adjustment of the bending length, $\ell_b$.

stress term in rationalized units, is

$$\rho \frac{D\vec{v}}{Dt} = \rho \left( \frac{\partial \vec{v}}{\partial t} + \vec{v} \cdot \nabla \vec{v} \right) = -\nabla P_g + \vec{J} \times \vec{B} = -\nabla (P_g + P_B) + \left( \vec{B} \cdot \nabla \right) \vec{B}. \qquad (2.3)$$

The last RHS term in equation 2.3 accounts for magnetic tension. The relative importance of gas pressure and magnetic pressure is generally expressed by $\beta_p = P_g/P_B$, while the relative role of magnetic tension compared to plasma inertial stresses, $\propto \rho v^2$, is expressed through the Alfvenic Mach number, $M_A = v/v_A = \sqrt{5\beta_p/6}\ M$, where $v_A = B/\sqrt{\rho}$ and $M = v/c_s$ is the sonic Mach number. Only when both $\beta_p$ and $M_A$ are large can we be confident that Maxwell stresses are subdominant.

The jet plasma is initialized with a moderately large fiducial plasma beta, $\beta_{pj} = 25$. The analogous Alfvenic Mach number of the emergent jet is $M_{Aj} \sim 14$. Consequently, magnetic fields in the emergent jets are minor dynamical contributors. Nevertheless, as

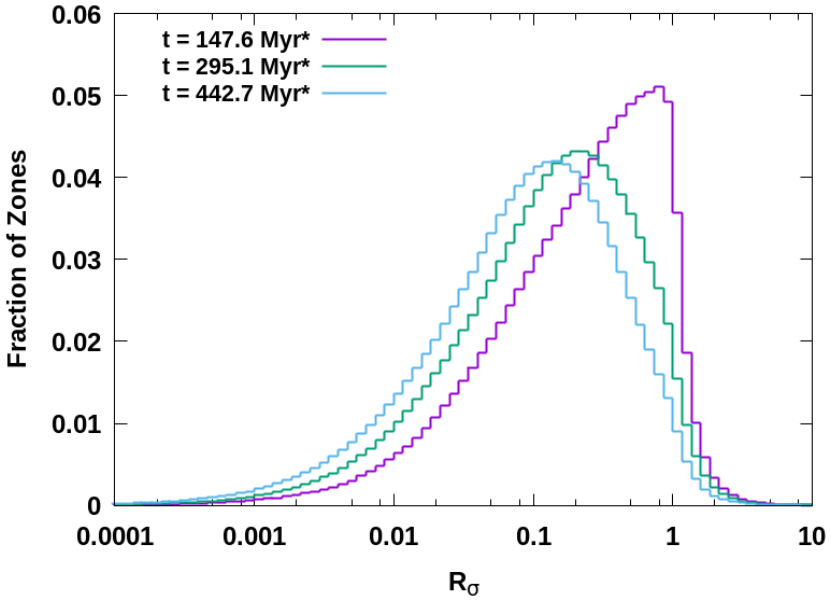


Figure 2.7 Log-linear histogram of the distribution of $R_\sigma$ in computational cells with significant jet mass fraction, $C_j \geq 1\%$, at three times during evolution of the reference NAT.

the jets propagate and disperse, regions quickly develop that are obviously influenced by Maxwell stresses nearly as much or more so than hydrodynamic stresses, particularly near regions of jet disruption. To explore this more fully we compute in each jet or tail simulation cell, $R_\sigma$, the ratio of Maxwell to hydrodynamical stresses; i.e.,

$$R_\sigma = \frac{\left|\vec{J} \times \vec{B}\right|}{\left|\nabla P_g + \rho\left(\vec{v} \cdot \nabla\right)\vec{v}\right|} = \frac{\left|\left(\vec{B} \cdot \nabla\right)\vec{B} - \nabla P_B\right|}{\left|\nabla P_g + \rho\left(\vec{v} \cdot \nabla\right)\vec{v}\right|}. \tag{2.4}$$

Values of $R_\sigma \gtrsim 1$ indicate strong Maxwell stress influence. As plasma emerges from the jet launch cylinder, $R_\sigma \lesssim 1/M_{Aj}^2 \lesssim 0.01$. Figure 2.7 shows the full distribution of $R_\sigma$ at three times in cells that have $C_j \geq 0.01$ (that is, at least 1% of the mass in the cell originated in one of the jets, which are the only sources of magnetic field in the simulation). The total number of cells included in the histograms increases from roughly 1% to 4% of the simulation domain over the time span sampled. The $R_\sigma$ distribution at the earliest time shown, $t = 147.6$ Myr, when the NAT phase is becoming clearly established (see figure 2.3), resembles a log-normal curve for low values of $R_\sigma$ and peaks

around $R_\sigma \approx 0.8$. The fraction of cells with $R_\sigma \geq 0.3$ in the distribution at this time is $\approx 45\%$ of those included, although there are relatively few with $R_\sigma \geq 1$. Throughout the early NAT phase, we find a similar distribution in $R_\sigma$ that peaks just below one, then drops sharply at higher $R_\sigma$ values. Such a distribution is consistent with a plasma that is threaded with magnetic fields that are stretched and strengthened by fluid motions (cf. equation 2.2) until Maxwell stresses are strong enough that they inhibit those motions and stifles further field amplification (cf. equation 2.3); i.e., the magnetic field amplification saturates. Closer examination of the stresses shows that magnetic tension generally plays a larger dynamical role than magnetic pressure. At later times, as the NAT structure becomes more extended, but also as jet disruptions influence relatively less of the tail structures, the Maxwell stresses play less significant roles overall. This is evident from the $R_\sigma$ distributions at $t = 295.1$ Myr and at $t = 442.7$ Myr shown in figure 2.7.

### 2.3.4 Cosmic Ray Electron Dynamics

As outlined in §2.2, our simulation tracks a CRe population within the particle Lorentz factor range, $10 \lesssim \Gamma_e \lesssim 2 \times 10^5$. We explore below synthetic synchrotron observations at frequencies $\nu \lesssim 1$ GHz in the source frame (so, at z = 0.2, 20% above the observed frequency). Those emissions in our reference NAT come primarily from regions with magnetic field strengths very roughly, $B \sim 1 - 10\mu$G. Using standard synchrotron relationships ($\nu_{GHz} \sim \nu_c \sim 4 \times 10^{-9} B_{\mu\mathrm{G}} \Gamma_e^2$; $\nu_c \sim (3/2)\Gamma_e^2 \nu_B$, with $\nu_c$ the so-called critical synchrotron frequency and $\nu_B$ the nonrelativistic electron cyclotron frequency) brighter emissions in the band we model relate very roughly to $\Gamma_e \lesssim 10^4$ (e.g., Rybicki & Lightman, 1979).

After they emerge from the launch cylinder our CRe can gain and lose energy in several ways. They can be accelerated via DSA during any sufficiently strong shock passage, based on behaviors laid out in §2.2. Briefly reiterating, within energy bins spanning about a factor 3, the CRe particle momentum distribution emergent from a shock is assigned a power law slope that is the flatter of the incident slope and that defined by test-particle DSA at that shock ($q = 4M_s^2/(M_s^2 - 1)$). However, in the reference simulation under discussion, the only shocks strong enough to influence the CRe are shocks within the jets near their launch cylinder. More broadly, the CRe are

subjected to energy losses and gains from adiabatic expansion and contraction as well as losses by radiative cooling (synchrotron and iC off CMB photons). Since magnetic fields in our simulation are predominantly less than the radiatively equivalent field strength of the CMB ($B_{\rm CMB} \approx 4.7\mu$G at z = 0.2), iC losses mostly, but not universally, dominate synchrotron losses in our simulation. The iC cooling time at redshift, z = 0.2, is (Sarazin, 1999),

$$\tau_{rad}(\Gamma_e) \approx \frac{10^6}{\Gamma_e} \ \ {\rm Myr} = \frac{\tau_o}{\Gamma_e}. \tag{2.5}$$

This translates for $\Gamma_e \sim 10^4$ very roughly as $\tau_{rad} \sim 100$ Myr, so of the same order as the dynamical evolution timescale of our NAT ($\sim$ a few $\times\, \ell_{\rm b}/{\rm v_w} \sim 100$ Myr) and to our estimated turbulent eddy time, $\tau_{eddy} \sim 80$ Myr. The jet speed, $v_j \approx 25$ kpc/Myr, is more than an order of magnitude faster than the wind speed, $v_w$, in our simulation, so, while AGN plasma remains inside coherent jet flows, it can traverse the NAT structures in only a few Myr. Even accounting for jet disruptions that limit this direct transport, fast jet transport accounts for the obvious, ongoing CRe refreshment described in §2.4. On the other hand, the complex CRe histories within the object also explain quite naturally why the local CRe electron distributions, $f(p)$, are quite heterogeneous, and mostly not well described as power laws over broad energy ranges.

We did not model 2$^{\rm nd}$ order CRe reacceleration by NAT-tail turbulence ("Fermi II" reacceleration) in our simulation. As noted above, tail turbulence is highly inhomogeneous and unsteady. Given that the efficiency of Fermi II reacceleration depends sensitively on details of how turbulent kinetic energy cascades to wave energies on scales orders of magnitude smaller than we consider in our simulations (e.g., Brunetti & Lazarian, 2011; Lynn et al., 2014), and that the timescales for the energy cascades are comparable to those associated with jet disruption events, meaningful Fermi II models in this context would require considerable care.

Sophisticated Fermi II modelling is beyond our present scope. We will address the issue in future work. For now we refer only to a simple, crude relationship between the large eddy timescale, $\tau_{eddy} \sim \ell_t/\delta v_t$ and the Fermi II reacceleration time based on so-called "TTD" resonance between the CRe and MHD fast-modes; namely, $\tau_{acc} \sim \tau_{eddy}(c/v_t)(1/\Phi)$. Again, $v_t$ is the outer scale turbulent velocity, while $\Phi > 1$ is a model-dependent function that relates to the fast mode turbulent wave spectrum and

the smallest dissipation scale of fast mode turbulence in the medium of interest (e.g., Brunetti & Jones, 2014). From this we expect that $\tau_{acc} > \tau_{eddy}$, which reinforces our concern about the unsteady character of NAT-tail turbulence in evaluating the role of Fermi II acceleration in the current context.

## 2.4 Synthetic Radio Observations

We computed and analyzed synthetic radio synchrotron emissions of the reference NAT source in order to link the dynamical behaviors outlined above with associated observable properties. Spectral intensity, $I_\nu$, and associated polarization and spectral index, $\alpha_{\nu 1,\nu 2} = -log(I_{\nu 1}/I_{\nu 2})/log(\nu 1/\nu 2)$, maps were obtained by integrating spectral emissivity along lines of sight through the simulated volume. Emissivities, including linear polarization, were computed at a given frequency, $\nu$, utilizing full 3D vector information about the magnetic field and integrating the synchrotron emission kernels, $F(\nu/\nu_c)$ and $G(\nu/\nu_c)$, over $\nu_c$, where $\nu_c = (3/2)\Gamma_e^2 \nu_{B\perp}$, and $\nu_{B\perp} = \nu_B \sin\theta$, with $\theta$ the angle between the local magnetic field and the line of sight (e.g., Rybicki & Lightman, 1979). If the CRe distribution (assumed isotropic) is a pure power law, $f(p) \propto p^{-q}$, over a broad range $[p_1, p_2]$, and $\nu_{c1} \ll \nu \ll \nu_{c2}$, where $\nu$ is the frequency of observation while $\nu_{c1}$ and $\nu_{c2}$ are the critical synchrotron frequencies for $p_1$ and $p_2$, then $\alpha = (q-3)/2$. Under similar conditions, accounting for shifts in $\nu_c$ at fixed $\nu$, $I_\nu \propto \nu_{B\perp}^{(q-1)/2}$. As CRe in our simulation first emerge from the jet launch cylinder with $f(p) \propto p^{-4.5}$ over a wide momentum range. So, at radio frequencies we model here, the synchrotron emission has an index, $\alpha = \alpha_0 = 0.75$, while the nominal intensity-magnetic field relation is $I_\nu \propto \nu_{B\perp}^{1.75}$. However, due to a combination of non-adiabatic gains and losses (predominantly radiative losses), the CRe distributions in our simulated NAT are not well-described as power laws over relevant energy ranges, so it is important to compute the synchrotron spectrum more carefully, as described above. Of course, as is well known, when CRe populations cool radiatively, $f(p)$ steepens from the top down so the associated synchrotron spectra steepen most rapidly at higher frequencies; i.e., the spectra "age."

Synthetic synchrotron images, as well as associated spectral and polarization maps of our reference NAT at reference frequencies, 150 MHz, 325 MHz, 600 MHz, 950 MHz

and 1.4 GHz in the observer frame[5] are shown in figures 2.8, 2.9, 2.10, and 2.11. To facilitate connection of emission features to dynamical features, the simulation $x$-$z$ plane was placed in the plane of the sky. Bilinear-averaged observing beams 0.895 kpc diameter (spanning 1.79 grid cells) were applied. From these images we also computed integrated radio fluxes and spectra reported in figures 2.12, 2.13 and 2.14. The polarization calculations did not include Faraday rotation. They would not be meaningful for this simulation given our simplifying assumption that the ICM (including ICM mixed into the NAT) was unmagnetized.

### 2.4.1 Analysis of Synthetic Images

We examine here synthetic intensity and spectral index ($\alpha$) maps from three snapshots in time spaced through this RG's evolution; two from the early phase when the NAT structure is still being defined (§2.3.2) and the other from well into the NAT phase (§2.3.2).

The 150 MHz and 950 MHz intensity images in figure 2.8 from $t = 49.2$ Myr show how our RG appears from this observer's perspective relatively early in its evolution (see figure 2.2 for associated dynamical structures). Depending on spatial resolution (and orientation relative to the observer), the apparent radio jets and plumes could be interpreted as the gently bent lobes of a WAT RG. On the other hand the high surface brightness at the ends of the jets ("hot spots") is characteristic of a morphological class II Fanaroff-Riley radio galaxy. Viewed with the plane containing the tails significantly out of the plane of the sky it is likely this object would be so-labeled. So, at this stage the future NAT appearance of this RG is not at all obvious. The first two pairs of jet recollimation shocks mentioned in §2.3.2 are evident as bright spots in the intensity images of figure 2.8. In addition, flattening of both $\alpha_{150,325}$ and $\alpha_{950,1400}$ at the first (stronger) recollimation shock pair, and of $\alpha_{950,1400}$ at the second such shock pair provide evidence for DSA in those shocks ($\alpha_{950,1400}$ is more sensitive in this context, since it communicates properties of higher energy CRe.) It is notable that these shock features are the only locations in the images at this time that rival the brightest structures at the ends of the jets. Those latter features correspond to highly bent, "soon-to-be-disrupted"

[5] These would become 180 MHz, 390 MHz, 720 MHz, 1.14 GHz and 1.68 GHz in the source frame for z = 0.2.

jet segments discussed in §2.3.2. In addition, the magnetic fields in those regions have been strongly enhanced by stretching ($B > 3\mu$G).

Because jet propagation is fast ($v_j \approx 25$ kpc/Myr), the CRe populations in the brightest regions of the $t = 49.2$ Myr snapshot are quite young. Radiative cooling influences are negligible at the lower observing frequencies, especially because the magnetic fields in those regions are relatively large, meaning that at fixed observing frequency, the CRe that dominate the emission have lower $\Gamma_e$. Even observed near 1 GHz iC radiative spectral aging of the synchrotron spectrum at this time is modest where B is stronger and due mostly to depletion of higher energy CRe with $\nu_c$ above the observed frequencies. Accordingly, in these regions, the lower frequency spectral index, $\alpha_{150,325}$, is close to the 0.75 expected at jet launch. Even at the higher frequencies in these bright regions $\alpha_{950,1400} \lesssim 0.9$ at this time. Lower surface brightness regions in the image of $I_{\nu,950}$ from figure 2.8 with $\alpha_{950,1400} \gtrsim 1.1$ come from diffuse, less directly propagated portions of the plasma plumes stripped from the young jets as described in §2.3.2. These regions also have weaker magnetic fields, and thus emissions correspond to larger $\Gamma_e$ with somewhat more "aged" CRe than in the brightest places. At 1.4 GHz, the contributing CRe in weaker field regions ($B < 1\mu$G) have iC cooling timescales $\tau_{rad} \lesssim 30$ Myr, so the high frequency spectral map reveals patterns of CRe energy evolution in such regions reflecting the history of jet plasma deposition. This accounts for the clear $\alpha_{950,1400}$ gradient within the bridge between the tails. Specifically, the spectrum steepens from the youngest CRe near the jets to older CRe at the perimeters of the plumes, now near the central plane.

By the time of figure 2.9 ($t = 147.6$ Myr), near the end of the transition out of early source evolution, the basic NAT structure that characterizes this object at later times is evident (figure 2.3 offers some insights to the dynamical state around this time). Even though it would likely be identified by observers as a NAT, the synchrotron source at $t \approx 150$ Myr has some observable properties that distinguish it from its appearance at significantly later times. For example, CRe in the bridge between the tails that bounds the head wake (e.g., figure 2.6), still produce observable synchrotron emissions at 150 MHz. The brightness falls substantially later on. Even at this time the bridge feature has begun to fade at higher frequencies, since the CRe there have not been refreshed in over 100 Myr. There is a rim-like arc bounding the upwind side of this

plasma bridge that is still visible, although $\alpha_{950,1400} > 1.5$, so it is fading seriously.

The brightness distributions in figure 2.9 at both high and low frequencies are dominated by the downwind extremes of the source; i.e., the nascent tail extremes, where jet plasma has been relatively recently deposited by the jet disruption event that began around $t \sim 100$ Myr (see figures 2.1, 2.3). Not only are the CRe distributions there relatively young, but, as pointed out above, the magnetic fields in those regions tend to be strongly amplified by stretching. The brightest patches in each tail, which have relatively flatter $\alpha$, correspond to collections of strongly magnetized filaments that are obvious in figure 2.6. Indeed, at high spatial resolution, such as in figure 2.9, the intensity distributions of the tails is very filamentary, reflecting the magnetic field topology. This behavior continues through the NAT phase of the source evolution.

Figure 2.10 shows radio images of the NAT 442.7 Myr into the simulation, well into the NAT phase of evolution, and while the jets remain active. The jets have very recently undergone a significant disruption event. The brightness distributions and spectra strongly reflect the recent history of local AGN plasma, including CRe and magnetic fields. The recollimation features in the jets in the head region, with their fresh CRe at relatively high densities and compressed magnetic fields (cf. figure 2.6) are distinct. On the other hand, the tail-bridging "plumes" as well as more extreme tail sections that were apparent in figure 2.9 have not had their CRe replenished for a very long time, so have essentially faded away from visibility as a result of iC cooling, adiabatic expansion and magnetic field relaxation. Even what we called in §2.3.2 the "disruption zone" just downwind of the head that was once prominent, is relatively faint at this time. Disruptive jet actions that help to rejuvenate emissions have moved somewhat downwind. Indeed, the brightest radio emissions at this time are mid-tail and correspond to plumes of plasma from the most recent jet disruption events. The relatively flat spectra in those regions visible in images of $\alpha_{150,325}$ and $\alpha_{950,1400}$ from figures 2.10 attest to the youth of those CRe.

Figure 2.11 displays the polarization properties associated with the 150 MHz and 950 MHz intensities in figure 2.10. Faraday rotation is ignored. Polarized flux comes primarily from the brightest mid-tail plumes mentioned in the previous paragraph and from recollimation features in the jets. Coherent jet emissions in the head region are

highly polarized (mostly $\gtrsim 70\%$) at both frequencies, because of well-organized magnetic fields. Those field align with the jets (become poloidal) away from the launch cylinder due to stretching processes described in §2.3.3. Downwind of the disruption zone fractional polarization becomes patchy, and drops significantly in most areas. In the brightest regions discussed in the previous paragraph, fractional polarization is reduced even where the associated jets remain coherent. The jet flows are bent and twisted in this region, so most lines of sight pass through multiple, uncorrelated magnetic field alignments. The highest degrees of polarization in the tails are mostly on their edges, and, perhaps counter-intuitively, in fainter areas with short paths through emitting plasma. With good sensitivity and high spatial resolution, on the other hand, individual strongly magnetized and highly polarized filaments within the tails should still be observable.

### 2.4.2 Evolution of Integrated Synthetic Radio Emissions

Figures 2.12 and 2.13 display the time history of integrated synthetic radio emissions from our reference NAT. Figure 2.12 shows the evolution of source-integrated fluxes at 5 frequencies (150 MHz, 325 MHz, 600 MHz, 950 MHz and 1.4 GHz), while figure 2.13 illustrates the evolution of source-integrated spectral indices between pairs of these frequencies. The peak fluxes at the 5 frequencies are not simultaneous, but all come relatively early, before the NAT phase is established. There are obvious secondary and roughly coincident flux peaks at all 5 frequencies around $t \sim 420$ Myr, or shortly before the state represented in figure 2.10, i.e., coincident with a major jet disruption event. Perhaps the most notable property apparent in the integrated flux history is that following the initial early peaks, the fluxes at all 5 frequencies are relatively steady until jet activity ceases, $t \approx 550$ Myr. After that the fluxes drop roughly exponentially on a timescale $\sim 100$ Myr, consistent with our estimate for the iC cooling time, $\tau_{rad}$. The nearly steady fluxes over something close to 400 Myr is remarkable, and indicates a rough balance of radiative growth and decay factors.

That the fluxes at all 5 frequencies are approximately steady over a long time suggests, as well, that the integrated source spectra are not evolving dramatically during that time. Figures 2.13 and 2.14 allow a closer look at this issue. Over the initial $\sim 200$ Myr of source evolution, so from startup through the transition into initial development

of NAT morphology, there is significant steepening of the spectrum, increasing towards the higher frequencies; that is, the integrated spectrum ages during initial source development. The timescale for this is, not surprisingly, again comparable to the iC radiative cooling time. By $t \sim 200$ Myr, the spectral indices range between $\alpha_{150,325} \sim 1.2$ and $\alpha_{950,1400} \sim 1.5$. Subsequently, the slopes very slowly flatten slightly over the next $\sim 300$ Myr by amounts that are around $\sim 10\%$. Roughly speaking, the spectral shape of the source is, effectively self-similar from the time the NAT form develops until the jet activity ceases. This behavior is also apparent in figure 2.14, which presents the integrated source synchrotron spectra between 150 MHz and 1.4 GHz at 6 times between 49.2 Myr and 442.7 Myr.

A closer look at the events reveals the following relevant information. During the initial phase of the source evolution, the spectrum steepens from its injection form ($\alpha = 0.75$) mostly due to iC cooling of CRe in the initial, transient plumes, which dominate the emission during the first $\sim 200$ Myr. The subsequent spectral flattening comes as the initial plumes fade, and the structure transitions to an approximately steady-state NAT morphology for the duration of time the jet is active. After the jet activity ends, of course, the spectrum ages as CRe radiate away their remaining energy, most rapidly at high energies.

Additional insights to the spectral evolution of our source while it is a NAT driven by steady jets come from the classic treatment of synchrotron emissions from a CRe population that ages radiatively at a steady rate while maintaining an isotropic distribution and being refreshed at a steady rate. In particular, if an isotropic CRe population is injected with a constant power law momentum spectrum and uniform magnetic fields yielding a synchrotron emissivity spectral index $\alpha_0$, then above a critical frequency corresponding to CRe with radiative cooling time, $\tau_{rad} \approx t$, the integrated spectral index becomes $\alpha_0 + 0.5$, while below that frequency, the integrated spectral index remains the injection index, $\alpha_0$ (e.g., Pacholczyk, 1970). In this simple situation we would expect over a time span of several hundred Myr that our synthetic spectrum would steepen from $\alpha_0 = 0.75$ to a steeper power law with $\alpha = 1.25$ above some frequency decreasing over time. Interestingly, by the beginning of the steady phase of our NAT evolution, some 200 Myr in, $\alpha_{150,325} \sim 1.2$, then actually flattening slightly to $\alpha_{150,325} \sim 1.1$ by $t \sim 400$ Myr. These slope changes seem roughly in accord with the simple model just

mentioned. On the other hand, the integrated spectrum is actually somewhat convex, becoming steeper at higher frequencies. That is not in accord with the simple model, at least after the low frequency spectrum has become "aged."

To put that in context it is important to keep in mind that the spectrum of the simple aging model just outlined assumes not only that the rate of aging and injection are constant, which is approximately true in our NAT, but also that the emissions come from a region of uniform magnetic field. This is certainly not true in our NAT, and leads to spatial variations in the spectra, as discussed above. Indeed, during the NAT phase the emissions from weak field regions, such as large portions of the tails, have distinctly steeper spectra because the CRe there are not being refreshed. In particular they have spectra steeper than $\alpha \sim 1.5$ at the higher frequencies. Although the surface brightness in those regions is relatively low, they still can contribute a significant portion of the integrated fluxes. The prolonged existence of a steady, self-similar, curved spectrum, on the other hand, runs counter to use of spectral shape as a direct age metric.

## 2.5 Conclusions

We have reported on an investigation of a simulated RG undergoing a long-term interaction with a persistent, homogeneous ICM wind perpendicular to the axis of the source AGN jets. The RG evolution ultimately gives rise to a narrow-angle head-tail (NAT) morphology. Such objects have been observed by radio astronomers for decades, and there have been multiple, prior theoretical and computational model efforts. The present paper represents the first high-resolution numerical study focused on the detailed evolution of a NAT utilizing 3D MHD, including energy-dependent transport of relativistic CRe released by the AGN. This treatment allows us not only to follow detailed dynamics and topology of magnetic fields developed by the NAT coming from the AGN, but also to generate meaningful synthetic synchrotron observations allowing for energy evolution of the CRe. In the simulation studied here the ICM was unmagnetized in order to focus on the evolution of the AGN injected magnetic field. We also include in our report an Appendix exploring simple analytic treatments of the development of NAT morphology for a variety of wind-jet orientations. The key findings from this work are as follows.

1. The RG takes quite a long time, $\sim$ 100 Myr for this RG, to develop a NAT morphology. During the early phase, the jets grow transverse to the wind faster than the bending action by the wind ram pressure, and jet plasma is propelled to a transverse extent roughly twice the eventual equilibrium jet trajectory. This phase includes a transient stage where the jets are gently bent and the morphology resembles that of a WAT.

2. Post-bending, the NAT plasma supplied by the AGN jets, including CRe and magnetic fields, is not simply advected passively downstream. Rather, the deflected jets actively push downwind and power the growth of the tails, the ends of which extend faster than the wind speed so long as the jets remain active. For the geometry of this simulation all jet momentum pointing downstream has been transferred to the light jets from the heavier wind; momentum of the denser, slower wind has been concentrated into the lighter, faster jets. This momentum is then transferred to the mixed, intermediate density tails, leading to a net velocity boost of that flow over the undisturbed wind flow. This boost of the tail propagation could, in some situations lead to interactions between the AGN and regions well downwind of where interactions with the wind began, such as a pre-existing ICM shear layer or shock. This could include a shock that created the wind.

3. The jets themselves remain remarkably coherent once bent, although instabilities do arise that cause the jets to flap and sometimes disrupt on characteristic timescales determined by signal propagation between the tails, $\sim 25 - 50$ Myr in the NAT simulated here. These events are in our simulations mostly initiated by finite amplitude disturbances external to each jet, including chaotic motions in the jet wakes, and also from earlier disturbances propagated from flapping motions of the other jet. We speculate that this dynamical feedback between the two jets could be an essential element of NAT evolution.

4. The dynamical interaction between the jets and the wind greatly enhances magnetic fields coming from the AGN in the NAT, primarily via stretching behavior. The plasma emerging from our simulated AGN has a toroidal magnetic field that is initially dynamically insignificant (high plasma $\beta_p$). However, stresses coming from the bending process quickly give rise to a mostly poloidal magnetic field

with the strongest fields having $\beta_p \lesssim 1$. The jet disruption events further stretch the fields and increase magnetization of the deposited plasma. As a result, the strongest magnetic fields in the tails are found in magnetic filaments that in the simulations are comparable to the numerical resolution thick (so, $\sim$ kpc) and tens of kpc long.

5. Observationally, once CRe populations released early on have significantly aged via radiative losses, the synthetic synchrotron radiation produced by our NAT exhibits self-similar, steady-state spectral properties for 100's of Myr, until the AGN activity ceases. The integrated spectrum during this period appears slightly convex and remarkably steady. This combination of a steady, but curved form means the curvature does not provide a useful, direct age metric of the source.

This research was supported at the University of Minnesota by NSF grant AST1714205 and through resources provided by the Minnesota Supercomputing Institute. CN was supported by an NSF Graduate Fellowship under Grant 00039202. Thanks to our many colleagues, particularly Larry Rudnick and Avery F. Garon for their motivation and insight.

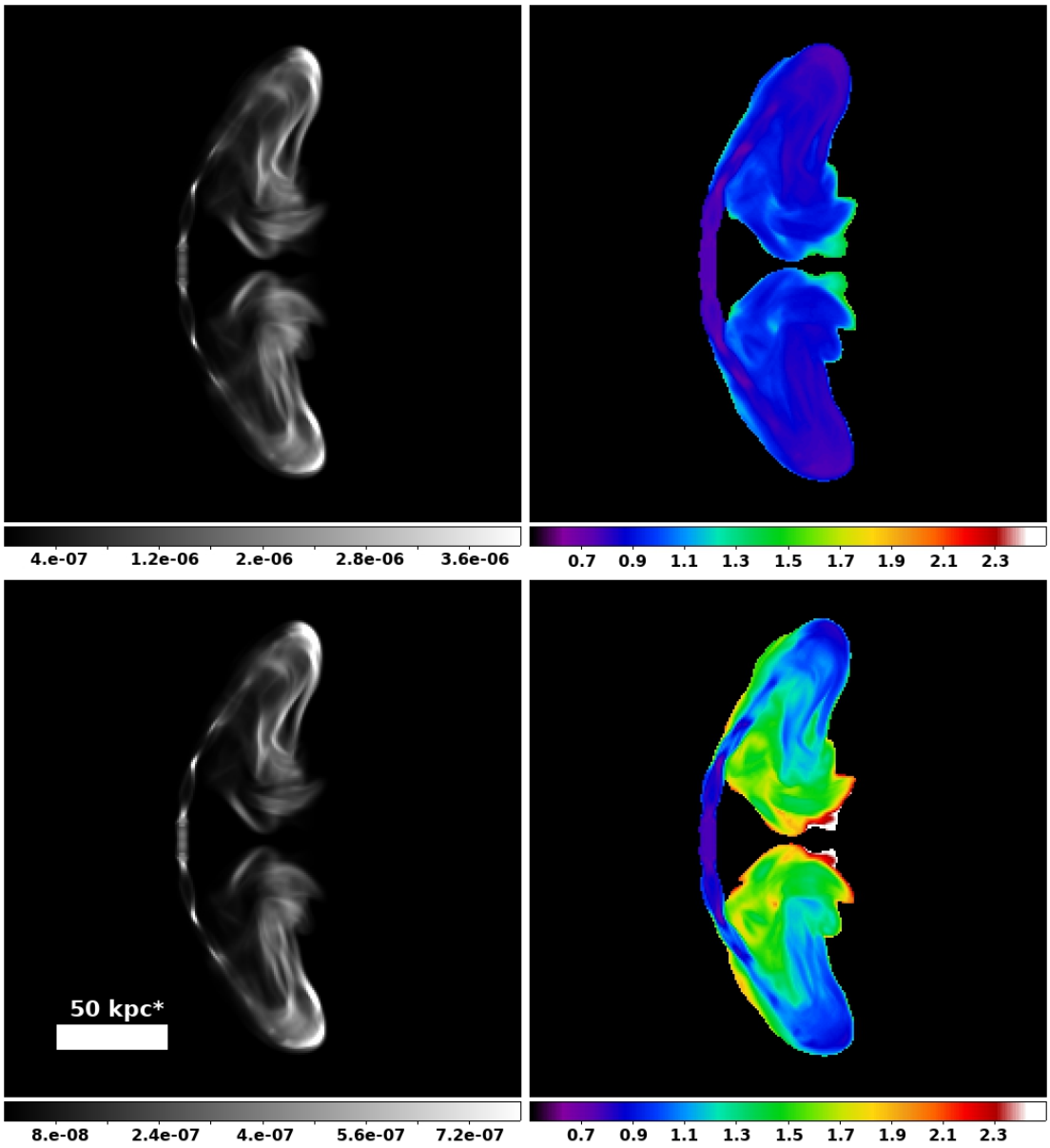


Figure 2.8 Radio images at $t = 49.2$ Myr*. Top Left: $I_{\nu,150}$. Bottom left: $I_{\nu,950}$. Top right: $\alpha_{150,325}$. Bottom right: $\alpha_{950,1400}$. Intensities are in arbitrary units. Brightest regions have been slightly saturated to reveal fainter features. Multiple jet hot spots in the head on either side of the launch cylinder correspond to recollimation features mentioned in the text. The $\alpha$ maps include only pixels having $I_\nu$ within a factor 500 of the brightest pixels at the higher frequency. The * in labels serves as a reminder that the nominal length (and time) scales can be increased or decreased by adjustment of the bending length, $\ell_b$.

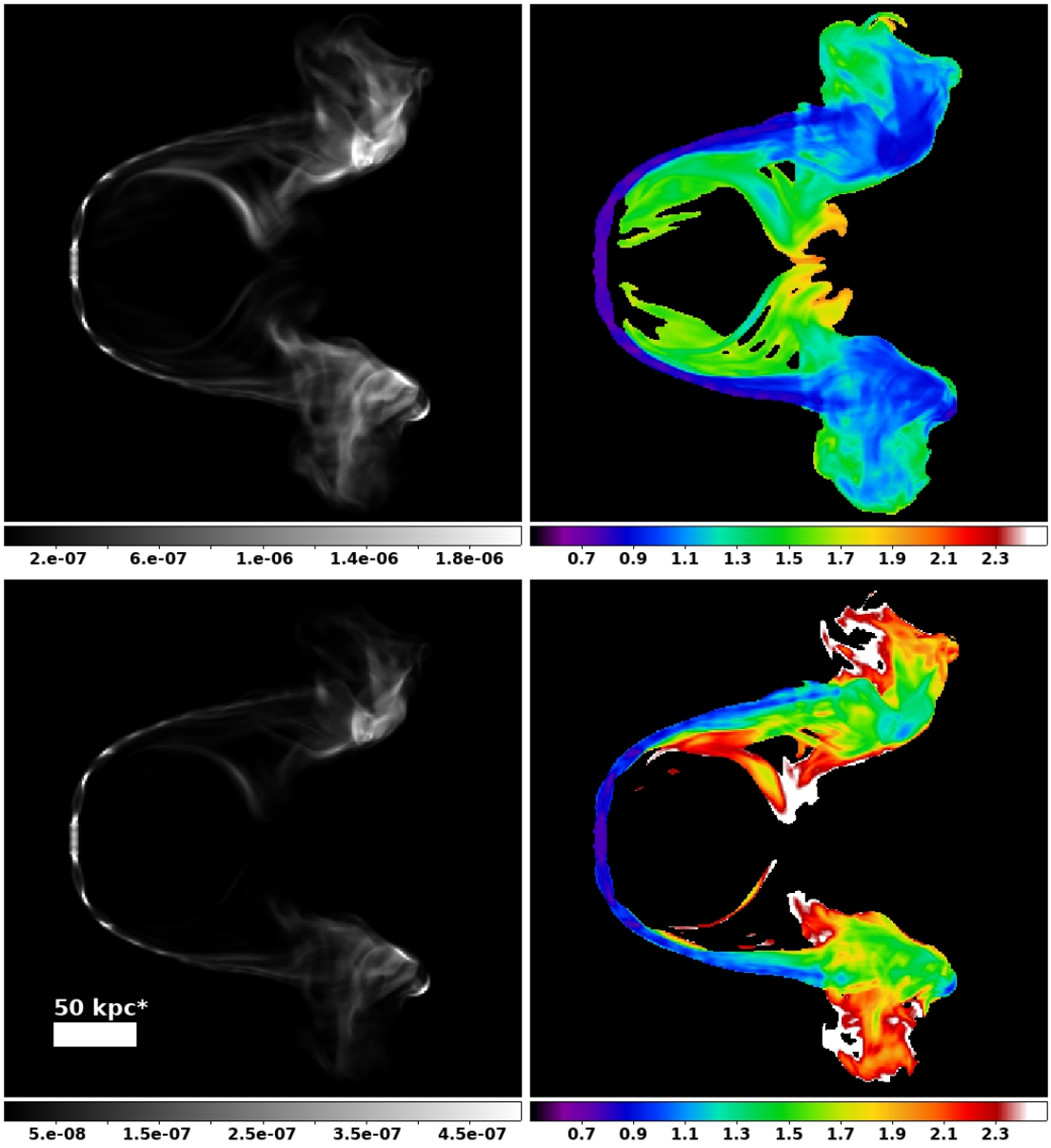


Figure 2.9 Same as figure 2.8 at $t = 147.6$ Myr*. The * in labels serves as a reminder that the nominal length (and time) scales can be increased or decreased by adjustment of the bending length, $\ell_b$.

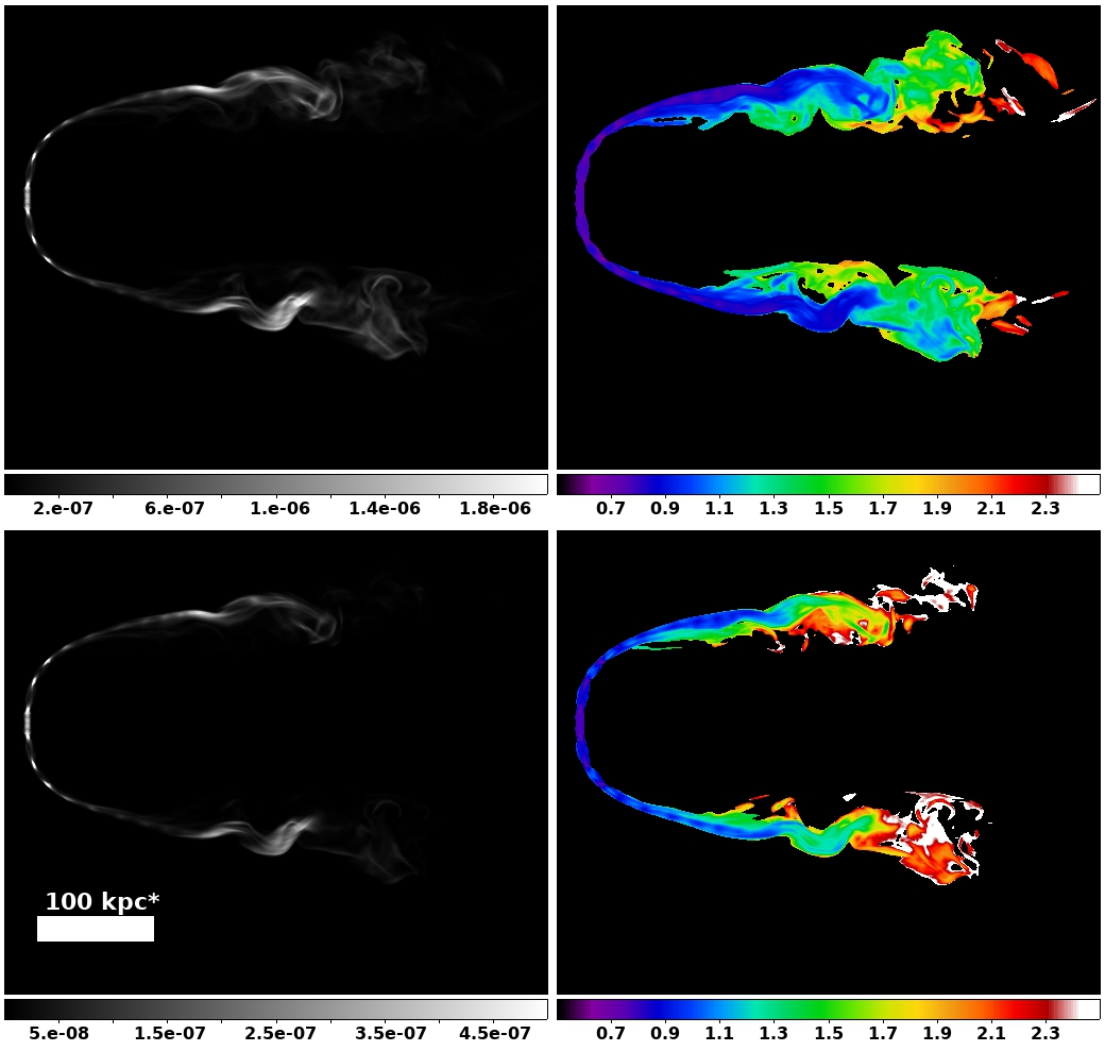


Figure 2.10 Same as figure 2.8 at $t = 442.7$ Myr*. The * in labels serves as a reminder that the nominal length (and time) scales can be increased or decreased by adjustment of the bending length, $\ell_b$.

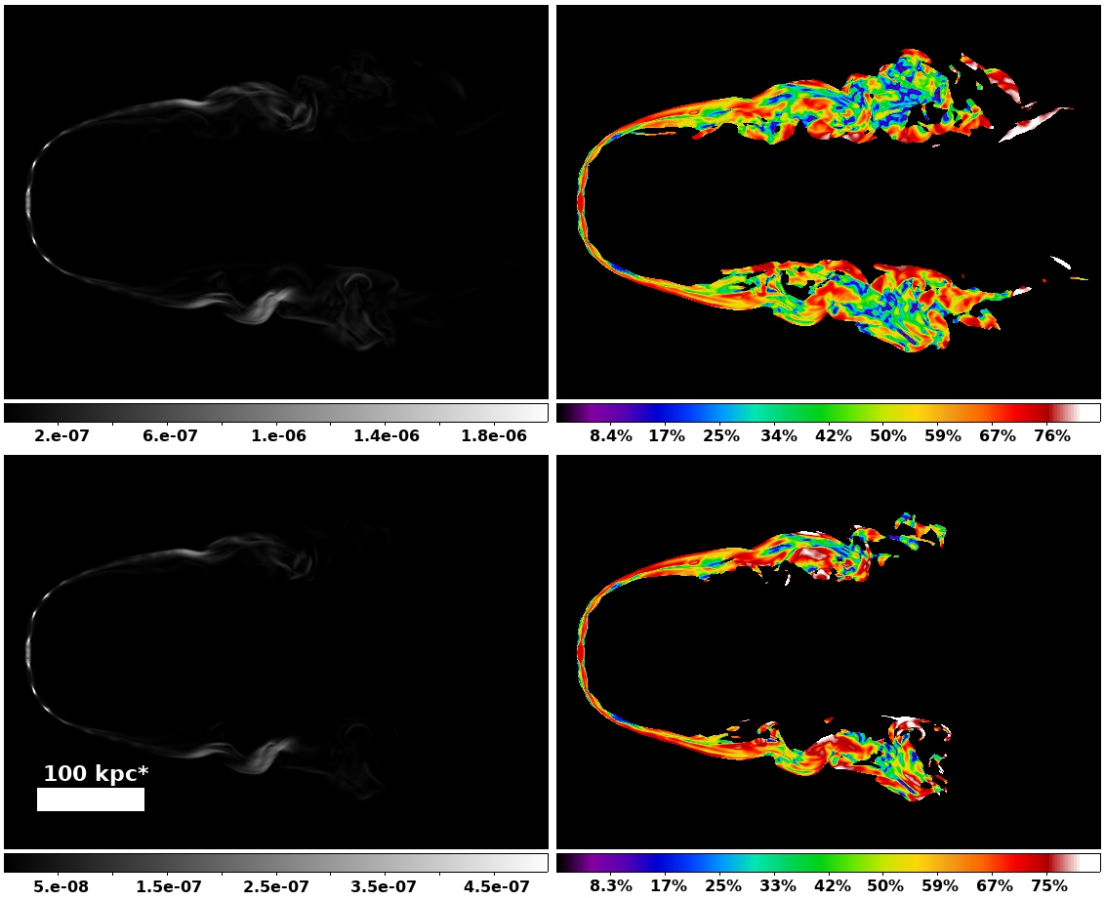


Figure 2.11 Polarized radio emission at $t = 442.7$ Myr*. Top left: polarized intensity at $\nu = 150$ MHz. Top right: fractional polarization at $\nu = 150$ MHz. Bottom left: polarized intensity at $\nu = 950$ MHz. Bottom right: fractional polarization at $\nu = 950$ MHz. Fractional polarization is computed in pixels with $I_\nu \geq 0.5\%$ of the peak at each frequency. Jet intensity hot spots near the head again reveal recollimation structures mentioned in the text. The * in labels serves as a reminder that the nominal length (and time) scales can be increased or decreased by adjustment of the bending length, $\ell_b$.

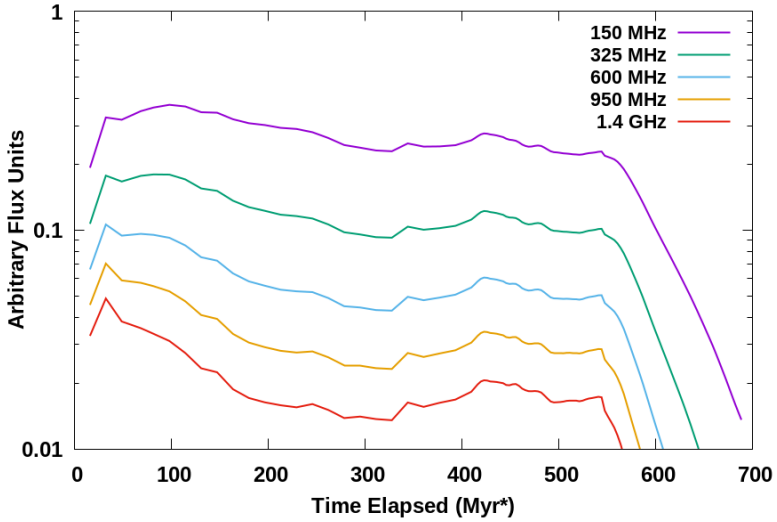


Figure 2.12 Time evolution of integrated fluxes (arbitrary units) at 150 MHz, 325 MHz, 600 MHz, 950 MHz and 1.4 GHz. Fluxes are sampled every 16.396 Myr* before 393.5 Myr*, then every 3.279 Myr* thereafter. Jets turn off at $t = 546.6$ Myr*. The * in labels serves as a reminder that the nominal length (and time) scales can be increased or decreased by adjustment of the bending length, $\ell_b$.

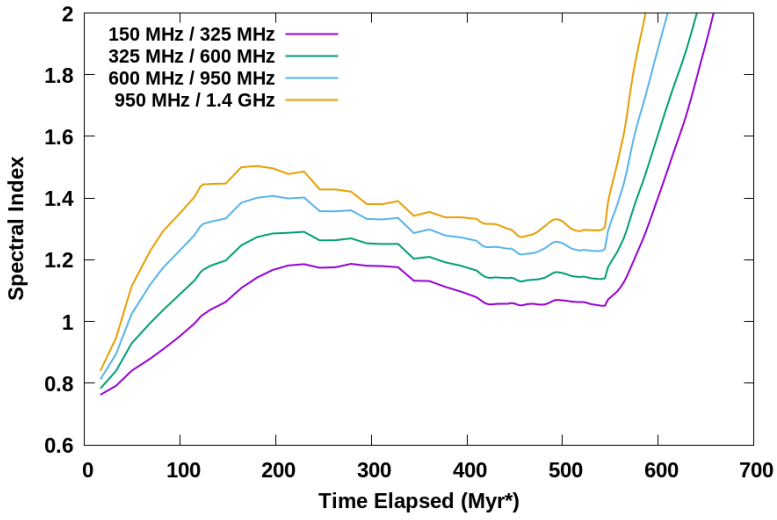


Figure 2.13 Time evolution of integrated spectral indices, $\alpha_{\nu 1,\nu 2}$, between adjacent frequencies in figure 2.12, sampled at the same time interval. The * serves as a reminder that the nominal time scale can be increased or decreased by adjustment of the bending length, $\ell_b$.

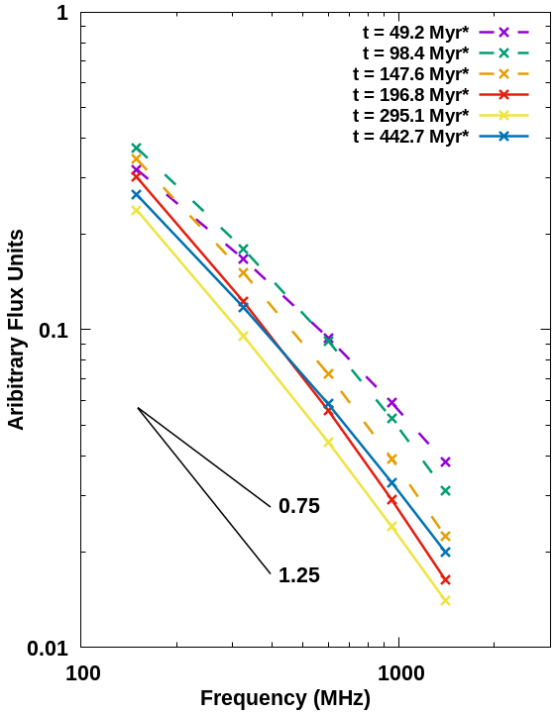


Figure 2.14 Integrated spectra from synthetic observations at selected times during simulation. The source population spectral slope, $\alpha_0$, and the fiducial $\alpha_0+0.5$ integrated spectral slope discussed in the text are shown for comparison. The * in labels serves as a reminder that the nominal time scale can be increased or decreased by adjustment of the bending length, $\ell_b$.

# Chapter 3

# Shocked Narrow-Angle Tail Radio Galaxy Simulations

*To be submitted to The Astrophysical Journal by Brian J. O'Neill, T. W. Jones, Chris Nolting & P. J. Mendygral*

**Abstract**

We report on a numerical investigation of the interaction between the elongated outflows representative of an evolved narrow-angle tail (NAT) radio galaxy and shock fronts typical of those induced by cluster merger activity. The simulations we run utilize a three-dimensional magnetohydrodynamic method with energy-dependent transport of cosmic ray electrons to carry out this study. We use a Riemann problem-based theoretical model to analyze the character of the shock front while passing through the heterogeneous plasma of our simulated tails. Shock-induced vortical motions are observed within the tails that contribute to coherent turbulent dynamo processes that continue to amplify the magnetic fields in the tails well after shock compression. We analyze synthetic observations throughout the duration of our NAT-shock interaction, and examine the brightness and spectral properties of our rejuvenated radio emission and the extent to which the pre-shock state of the plasma and particle populations in our tails influences the post-shock observations. Finally, we summarize our findings in the context of our

simulated tails providing the seed relativistic electron population for a radio relic.

## 3.1 Introduction

The cosmic assembly of galaxy clusters is an ongoing process that occurs via merger events of smaller clusters and groups, and accretion onto clusters from cosmic filaments. The state of the intracluster medium (ICM), the diffuse plasma between galaxies, reflects the history of a cluster's formation. The infall of dark and baryonic matter generates a dynamic environment in the ICM, driving winds, shocks, cold fronts, turbulence and sloshing motions to name a few consequences (e.g., Markevitch & Vikhlinin 2007; Brüggen et al. 2012; Schuecker et al. 2004; Simionescu et al. 2019). In particular, mergers of similarly sized clusters (referred to as "major mergers"), can generate large-scale ($\lesssim 1$ Mpc) shock fronts that propagate into each merger member (e.g., Shimwell et al. 2014; van Weeren et al. 2016). ICM plasma is generally very hot with high sound speeds, so merger shocks tend to be weak; simulations of cosmological structure formation suggest that shocks with $2 \lesssim M \lesssim 4$ play the dominant role in shock heating the ICM (e.g., Ryu et al., 2003; Kang et al., 2007). Outflows from active galactic nuclei (AGN) also play a role in the ICM dynamics of their host cluster; in particular, powerful jets from centrally located AGN are thought to play an important role in regulating cooling of the ICM in cluster cores (McNamara & Nulsen, 2007).

Temperatures in the ICM are on the order of $\sim 1$ - 10 keV, thus ICM plasma radiates X-rays via thermal bremsstrahlung. Shock fronts can be detected in X-ray emission, but the weak Mach numbers typical of these shocks, the fortuitous alignments needed and the low densities of the plasma they propagate through, particularly in the periphery of galaxy clusters, makes accurate detection and analysis of X-ray shocks difficult. The presence of hot plasma in clusters also makes an imprint on the cosmic microwave background (CMB) via the Sunyaev-Zeldovich (S-Z) effect, providing an indirect means of probing the densities and temperatures in the ICM (Mroczkowski et al., 2019). Much has been learned of the energetics and the dynamical states of cluster plasma from X-ray and S-Z observations, but smaller scale (down to $\sim 1$ kpc) flows and structures are generally not detectable with these techniques.

Nonthermal synchrotron radio emission from relativistic cosmic ray electrons (CRe) provide another set of beacons for studying the properties of the ICM with higher resolutions. The jet powered outflows of radio mode AGN, or radio galaxies (RGs), are locally bipolar and symmetric, but are often seen deformed on scales $\sim$ 10 - 100 kpc in response to relative RG-ICM motions (Garon et al., 2019). For instance, a strong persistent ram pressure, from a combination of winds and the RG's motion, aligned perpendicular to the jet axis will draw the radio luminous outflows into long, nearly parallel tails classified as a narrow-angle tail (NAT) RG (Rudnick & Owen, 1977). Additionally, thin, diffuse, frequently warped radio filaments with lengths up to $\sim$ 100's of kpc that are not obviously connected to a particular AGN outflow are being detected more and more as observational sensitivities and resolutions improve (e.g., Pizzo & de Bruyn 2009; Owen et al. 2014; Clarke et al. 2019).

Diffuse radio emission on scales up to $\sim$ 1 Mpc has been observed in a large number of clusters and tends to correlate with active clusters (see, e.g., van Weeren et al., 2019 for a comprehensive list). Radio relics, bright sources with elongated morphologies usually found in the cluster periphery, are notable in particular as a number have been identified to coincide with shocks detected in X-ray observations (e.g., Shimwell et al. 2015; van Weeren et al. 2016), suggesting the CRe responsible for the radio emission are accelerated from the bulk ICM plasma via diffusive shock acceleration (DSA). However, the remarkable brightness and spectral properties of observed radio relics combined with their tendency to be located in the outskirts of galaxy clusters strains the tenability that they are simply the product of DSA from weak shocks propagating through the low density plasma in cluster peripheries. In addition, the frequency of observed radio relics is perhaps an order of magnitude smaller than the expected prevalence of merger shocks (Ha et al., 2018) and X-ray shocks have been detected with no accompanying radio emission (see, e.g., Russell et al. 2011), implying a shock alone is not sufficient to produce a relic. The presence of pre-existing populations of "fossil" CRe, i.e. relativistic electrons that were released by an AGN and then cooled radiatively to non-luminous energies, may provide a remedy. Observations of RGs in close proximity to radio relics (e.g., Shimwell et al. 2015) and deformed head-tail RGs apparently in the midst of shock reacceleration (e.g., van Weeren et al. 2017; de Gasperin et al. 2017) lend credence to the plausibility of this framework.

The elongated morphology of a NAT provides an obvious prospective source of fossil CRe for a fortunately aligned shock front to reaccelerate into a radio source reminiscent of a radio relic. This scenario is the primary inspiration for this study, which is an extension of simulations performed in a companion paper (O'Neill et al., 2019a). In that work, we evolved a NAT RG for 100's of Myr and analyzed the formation and growth of $\sim$ 500 kpc long tails composed of a heterogeneous mixture of ICM and jet plasma containing CRe. In this paper, we use simulation data from that previous work to analyze the observable properties and the interaction between the evolved tails and shock fronts characteristic of those induced by merger events. These two papers, along with a set of related works that study the interaction of shocks with radio lobes formed in initially quiescent environments (Nolting et al., 2019a,b), together seek to advance understanding of the properties of RGs in active environments so that such sources can serve as diagnostic probes of "cluster weather".

The rest of the paper is organized as follows: In § 3.2, we outline the numerical simulations performed. In § 3.3, we present relevant details of the state of the unshocked tails and analyze the dynamics of the NAT-shock interaction. In § 3.4, we examine observations from throughout each of the NAT-shock interactions. We end with a summary of our conclusions in § 3.5.

## 3.2 Simulation Details

This is a continuation of a previous work, see O'Neill et al. (2019a) for full details on the domain and algorithmic methods used. We used simulation data from three unique timepoints 100's of Myr into the evolution of the NAT in that work: $t_{M2} = 409.9$ Myr, $t_{M3} = 508.3$ Myr and $t_{M4} = 557.5$ Myr. These timepoints serve as the initial conditions for simulations where planar shock waves of different strengths are initialized on a boundary and move through the domain with the shock normal parallel to the jet axis. The timepoints are chosen such that the total age of the NAT is roughly the same after shock fronts with initial Mach numbers of $M_w = 2$, 3 and 4 have completed passing over the NAT. These shocks are intended to represent the large-scale galaxy cluster shock fronts associated with merger events, so we refer to them as "merger shocks". Each merger shock is initialized on the $-z$ boundary utilizing the Rankine-Hugoniot shock

jump conditions of the desired Mach number:

$$\rho_2 = \frac{4M^2}{M^2+3}\ \rho_1 \tag{3.1}$$

$$P_2 = \frac{5M^2-1}{4}\ P_1 \tag{3.2}$$

$$v_2 = \frac{3}{4}\frac{M^2-1}{M}\ \sqrt{\frac{5P_1}{3\rho_1}}, \tag{3.3}$$

where subscripts 1 and 2 refer to unshocked and shocked background ICM and assuming adiabatic index $\gamma = 5/3$ everywhere. The zones on the $-z$ boundary were given density, pressure and $z$ velocity according to equations 3.1, 3.2 and 3.3. Transverse velocity is continuous across a shock, so these boundary zones were given the same $x$ velocity as the background wind. The inflowing shocked plasma is also unmagnetized, like the undisturbed ICM. Populations of CRe passing through shocks are subjected to standard, test-particle DSA, but as in O'Neill et al. (2019a), there is no injection of new particles into the CRe population from the thermal plasma at shocks in these simulations; the jet cylinder is the source of all CRe, aside from an insignificant non-zero population throughout the domain needed to avoid numerical singulaities.

| Name | Restart time (Myr) | AGN off time (Myr) | Shock Strength (Mach #) | Shock Speed (kpc/Myr) | Shock Compression |
|---|---|---|---|---|---|
| M2 | 409.9 | 518.1 | 2 | 2.045 | 2.286 |
| M3 | 508.3 | 546.6 | 3 | 3.068 | 3.000 |
| M4 | 557.5 | 586.0 | 4 | 4.091 | 3.368 |
| N2 | 409.9 | 518.1 | N/A | N/A | N/A |
| N3 | 508.3 | 546.6 | N/A | N/A | N/A |
| N4 | 557.5 | 586.0 | N/A | N/A | N/A |

Table 3.1 Simulation parameters for different runs in this work. Ages are measured from when the AGN source was activated. Shock attributes are representative of the shock in the background ICM.

We applied two different scenarios to each of the merger shock setups described above (see also table 3.1). In the primary scenario, the jet cylinder is shut off when the shock front first encounters the $-z$ tail, or shortly thereafter ($\lesssim 50$ Myr). In the second scenario, we do not introduce the merger shock at the boundary, but we still deactivate

the jet cylinder at the same time as in the primary scenario and allow the NAT to evolve and CRe populations to decay undisturbed. These runs serve as a control group to isolate the effects of the merger shock on the NAT.

## 3.3 NAT-Shock Interaction Dynamics

### 3.3.1 State of the Unshocked NAT

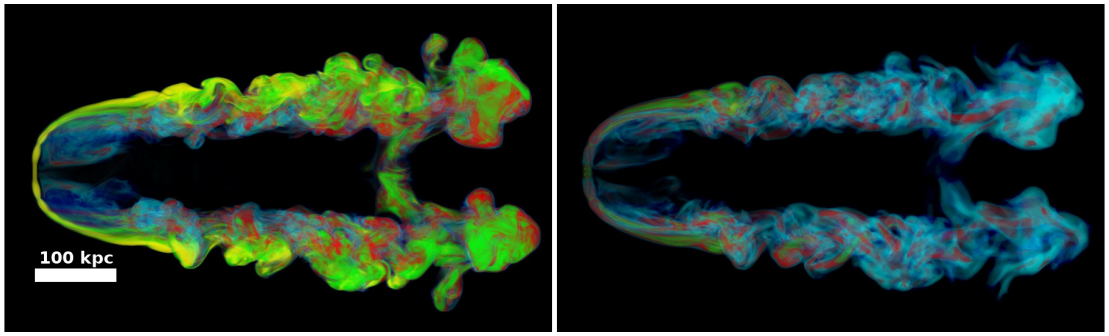


Figure 3.1 Volume renderings from **N3** at $t = 541.1$ Myr. On the left: Color variable, $C_j$ – blue: $C_j < 0.2$; aqua: $0.2 < C_j < 0.4$; red: $0.4 < C_j < 0.6$; green: $0.6 < C_j < 0.8$; yellow: $C_j > 0.8$. On the right: Magnetic field strength, $B$ – blue: $B < 0.2$ $\mu$G; aqua: $0.2$ $\mu$G $< B < 0.5$ $\mu$G; red: $0.5$ $\mu$G $< B < 1$ $\mu$G; green: $1$ $\mu$G $< B < 2$ $\mu$G; yellow: $B > 2$ $\mu$G.

The tails are a complex, turbulent environment whose motions are powered by the chaotic interaction between the jets and wind (cf. § 3 in O'Neill et al. 2019a). The volume rendering of the passive tracer of jet mass fraction ($C_j$) in the left side of figure 3.1 shows the distribution of the tails when they are well evolved and the jets are still active and feeding the tails. They begin roughly $\sim$ 100 kpc downstream of the AGN source, where the stable jets succumb to surrounding turbulent forces and begin to break apart. The coherent jets are separated by $\sim$ 150 kpc when they are intermittently disrupted by the onset of a "flapping" motion. Immediately downstream of the disruption region, the width of each tail is $\sim$ 60 kpc, about equal to the bending radius. The lateral extent grows as the plasma moves downstream; on the interior the separation between the tails remains $\sim$ 90 kpc (aside from remnants of the startup phase on the downstream end of the tails), while the width of each tail tends to grow

about 1 kpc for every 4.5 kpc in length. The plasma in the tails is essentially in two "phases": there are regions of predominantly jet plasma corresponding to parts of the coherent jets (we will refer to as "clumps") that have broken off and been bent and twisted by turbulent stresses, and a surrounding medium that is a mixture of varying proportions of jet and ICM plasma (which we will call the "diffuse" region). As the clumps travel downstream, they tend to mix more and more with ICM plasma, so $C_j$ values in the clumps decline as they evolve. The diffuse region begins even before the jets are disrupted as a consequence of wind shearing material off the coherent jets (see interior of the jets in figure 3.1). The diffuse tail plasma tends to dominate the interior of the tails, while the clumps maintain their initially high $z$-momentum which carries them towards the outside of the structure.

Magnetic fields in our simulations all originate from the AGN source, so only the jets and the tails have any significant magnetism. The interaction between the jets and the wind enhances magnetic field strengths, primarily through stretching. Strong fields in the tails tend to correlate with the clumps, oriented mostly in filaments running along the length of the clumps. These filaments are apparent in the volume rendering of magnetic field strength on the right side of figure 3.1. The fields are generally strongest just after disruption, and tend to diffuse as they move downstream. This diffusion is a result of turbulence in the tails as well as some numerical diffusivity inherent to the algorithmic methods used.

Our merger shocks are initialized with speeds ($v_{s,w}$) of 2, 3 and 4 times the sound speed of the undisturbed background wind, $c_w = 1000$ km/s, but the consequences of the shock interaction obviously depend on the state of the tail plasma being shocked. The particulars of shocking the tails are more complex (see § 3.3.2), but analyzing the sound speed in the unshocked tails is still informative of how the shock behaves within the tail plasma. Looking at the sound speeds in the **N3** simulation at $t = 541.1$ Myr, of all zones in the tails with $C_j \geq 0.01$, 50% have $c \geq 2c_w$, 11.6% have $c \geq 3c_w$ and 4% have $c \geq 4c_w$. Very roughly, we can expect the merger shock to have a Mach number half the initial value while passing through much of the tails. The plasma in the tails is largely in pressure equilibrium with the background, so the sound speed variations for the most part track density variations. The same sample of tail plasma has a median density compared to the background of $\sim 0.31\rho_w$, with about half the zones between

$0.1\rho_w$ and $0.5\rho_w$. The region between the tails has fluctuating densities slightly less than the undisturbed background (at most $\sim 5\%$ lower), so sound speeds in this middle region approach the initial ICM value. There is also a bridge between the tails on the right side of the images in figure 3.1 (a remnant of the early stages of the NAT's evolution), wherein the shock front pulls ahead while the rest of the front is slowed by the denser ICM plasma.

Turbulence in the tails is also relevant to the character of the shock front as it passes through. Structure functions of the velocity in the tails suggest an eddy speed in the tails of approximately half the background wind ($\Delta v \approx 0.5 v_w$), though the character of this turbulence is clearly not homogeneous or steady. The wind travels at $v_w = 0.9 c_w$, so this eddy speed is significant compared to the speeds at which our merger shocks travel. At any given moment, there will be regions of plasma in the tails with peculiar velocities oriented mostly towards or away from the shock front. Therefore, the relative velocity between tail plasma and the merger shock can significantly strengthen or weaken the shock felt by sections of the tail plasma.

### 3.3.2 Shock Strengths in the Tails and Shock Induced Vorticity

The shock-tail interaction is very complex, but very broadly it can be stated the merger shock travels faster but becomes weaker when propagating through the lower density tail plasma. Some insights can be gained from Pfrommer & Jones (2011), who investigated how an ICM shock traversing a low density bubble will transform the bubble into a toroidal vortex ring, analogous to a smoke ring. They investigated this interaction utilizing an analytic 1D Riemann problem model. When a shock travelling through the denser medium at speed $v_{s,i} = M_i c_i$ encounters a bubble, a weakened shock travelling at speed $v_{s,b} = M_b c_b$ propagates forward into the bubble with the initial bubble-ICM contact discontinuity (CD) trailing behind travelling at speed $v_{\mathrm{CD}}$, while a rarefaction wave propagates backwards into the post-shock medium. Assuming an initial pressure equilibrium between the ICM and the bubble as well as an adiabatic index of $\gamma = 5/3$ in both media, Riemann invariants and the shock jump conditions can be utilized to derive the following equation relating the bubble-ICM density ratio $\delta = \rho_b/\rho_i$, the initial Mach

number $M_i$ and the Mach number ratio $\mu = M_b/M_i$:

$$1 = \frac{\mu^2 M_i^2 - 1}{\mu\delta^{1/2}\left(M_i^2 - 1\right)} - \frac{\left(5M_i^2 - 1\right)^{1/2}\left(M_i^2 + 3\right)^{1/2}}{M_i^2 - 1}\left[1 - \left(\frac{5\mu^2 M_i^2 - 1}{5M_i^2 - 1}\right)^{1/5}\right]. \quad (3.4)$$

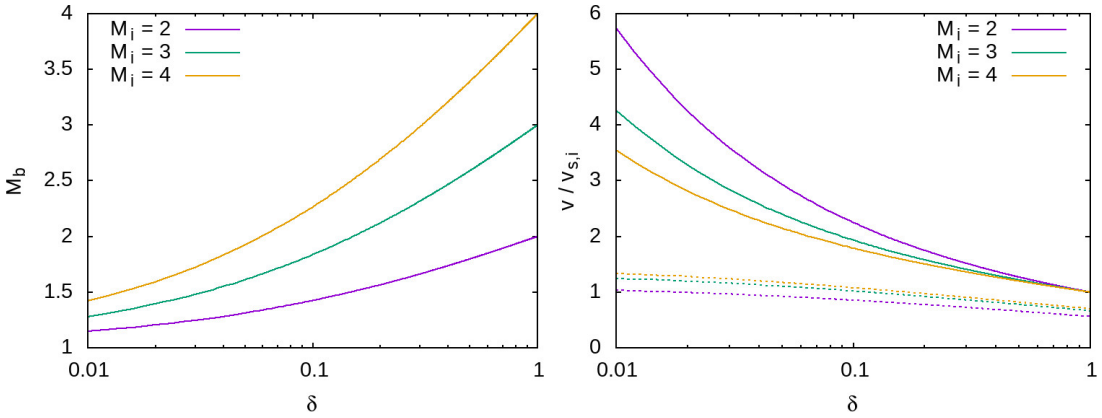


Figure 3.2 Properties of the shock strengths we use within a low density bubble as a function of the density ratio $\delta = \rho_b/\rho_i$. On the left: shock strength within the bubble $M_b$. On the right: wave speeds in the bubble relative to ICM shock speeds. Solid lines are shock speeds in bubble ($v_{s,b}$), dotted lines are the speed of the CD ($v_{\rm CD}$).

On the left side of figure 3.2, we numerically solve this equation as a function of the density ratio to show the modified shock strength for each of the merger shocks we use. Definitionally, the speed of the shock in the low density medium is related to the initial shock speed by $v_{s,b} = v_{s,i}\ \mu/\sqrt{\delta}$. The speed of the CD, which is equal to the speed of the post-shock flow, is defined (via Pfrommer & Jones 2011) as:

$$v_{\rm CD} = \frac{3(\mu^2 M_i^2 - 1)}{4\sqrt{\delta}\mu M_i^2} v_{s,i}. \quad (3.5)$$

We plot the ratio of these speeds to the initial shock speed on the right side of figure 3.2. In all cases with $\delta < 1$, the propagation time of the shock is shorter through the low density medium than in the background, and the merger shock propagates fastest through regions with lowest density. As the density in the cavity decreases, the strength of the shock asymptotically approaches $M_b = 1$, though the actual speed of the shock increases. In Pfrommer & Jones (2011), they model a shock running over a spherical

bubble, encountering the midplane of the bubble first and traversing through the center faster than the periphery, which transforms the bubble into a stable toroidal vortex. The time to transform into a vortex ring is approximately the crossing time for the CD to cross the midplane of the bubble. As evident in figure 3.2, the CDs associated with our shocks all travel at speeds on the order of the incident shock speed; i.e., $v_{\rm CD} \approx 1.34 v_{s,i}$ for $M_i = 4$ and $\delta = 0.01$ while $v_{\rm CD} = (9/16) v_{s,i}$ for $M_i = 2$ and $\delta = 1$.

The cross section of our tails tends to be widest in the middle, so a similar dynamic is at work here though it is complicated by the inhomogeneity and more complex morphology. The densities in the tails vary greatly along a typical path through the tails, so the strength and speeds of each portion of the shock front evolve throughout the interaction. In spots where the shock advances ahead of the front in neighboring plasma, the enhanced pressure of the shocked plasma will induce the shock to propagate laterally and induces curvature in the shock front. Passing over the first tail greatly deforms and bulges the shock ahead of the rest of the merger shock plane. The curvature of the shock front leads on average to a divergent post-shock flow on top of enhanced vorticity, which weakens the shock. This results in the Mach numbers across most of the shock front being $\sim$ 5-10% weaker than the initial value. Regions that are extremely distorted can end up with significantly weakened shocks ($\sim$ 50%).

The tails can roughly be thought of as a series of plumes sequentially inflated by the jets. Each of these plumes is approximately transformed into a vortex ring, with smaller scale holes developing through volumes where the shock and CD propagate significantly faster. These effects are evident in figure 3.3, which displays the projected jet mass (the product of $C_j$ and $\rho$ in each zone) through one of our tails at the same point in time in **M3** and **N3**, $\sim$ 30 Myr after the shock has completed passage through the tail. Through much of the tail, jet plasma has been swept towards the edges by vortical motions, particularly from volumes that are initially lower density. For example, in the bottom image (absent a shock interaction) the right most plume of the tail has denser plasma toward the left (centered around $x \approx 640$ kpc) relative to the rest of the plume, thus the shock travels relatively slower through this region. As a result, much of the shocked plume is initially bifurcated into separate rings around this denser plasma.

Initially the tails are very turbulent, and this turbulence is enhanced by the passage of the shock. The smaller scale ring-like structures end up being relatively short-lived

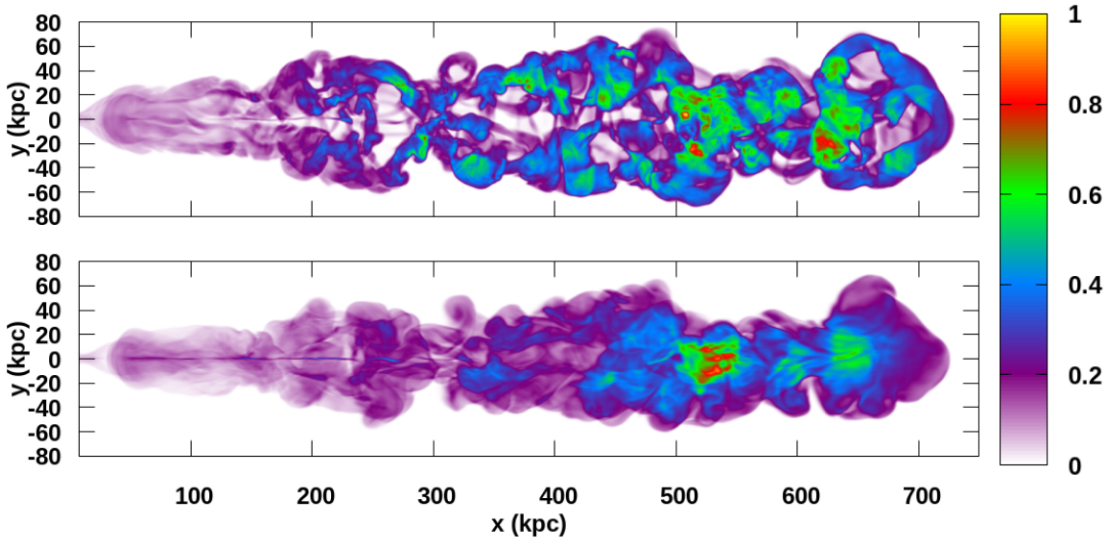


Figure 3.3 Jet mass projected along the $z$-dimension through the $-z$ tail at $t = 603.4$ Myr. Top image is from **M3** and bottom image from **N3**. The projected mass is scaled to the maximum value among the two images.

features that are torn apart by turbulent motions. The larger scale vortical motions are maintained, and in the long-term these sweep nearly all the jet plasma out of the midplane in the middle of the tail, such that a projected jet mass image like figure 3.3 evolves towards an outline of the original distribution. The transformation time towards this morphology is roughly the cooling time for radio luminous reaccelerated CRe ($\sim$ 100 Myr, see § 3.4), so it is less likely that such a structure would be observable. Also, while the configuration appears coherent viewed along the $z$-axis, by this time the jet plasma is not co-planar. Immediately after shock passage the $z$ extent of the tail is compressed, but turbulence gradually disperses tail plasma along the $z$-dimension into detached filaments that appear uncorrelated from other viewpoints.

### 3.3.3 Shocked Magnetic Field Strength and Topology

For a given plane, the cumulative distribution function of the angle $\phi$ between a randomly oriented vector and that plane is $F(\phi) = \sin\phi$, i.e., there is a 50% chance that $\phi \leq 30°$. Analysis of all magnetic field orientations in our unshocked tails shows the distribution appears to be random, but that stronger fields are more likely to be more

closely aligned with the $x$-$y$ plane. Relative to $x$-$y$ plane, the distribution of $F(\phi)$ for all $B$ values is close to $\sin\phi$, but tends to be skewed towards smaller $\phi$ for stronger fields; e.g. at $t = 610.0$ Myr in **N4**, $F(30°) = 49.0\%$ and $F(15°) = 27.6\%$ for all $B$ and $F(30°) = 56.3\%$ and $F(15°) = 30.6\%$ for $B \geq 1$ $\mu$G. The magnetic field in the AGN source is initially toroidal, but after the jets are bent by the wind the magnetic field in the coherent jets is dominated by the poloidal component, which is (mostly) parallel to the $x$-axis. Violent disruption events (which convert a portion of the kinetic energy from the jet-wind interaction into more magnetic energy) and turbulent flows in the tails reorient the fields, but a preferential alignment with the jet and wind flow is still partially maintained among the stronger fields. In particular, zones on the tail boundaries tend to have fields aligned with the $x$-dimension as a result of velocity shear stretching the fields along that direction. Synchrotron emissivity is dependent on the component of the magnetic field perpendicular to the line-of-sight ($j_\nu \propto B_\perp^2$), so fields that tend to be perpendicular to a given line of sight can stand out as compared with randomly oriented fields.

Compression only enhances the portion of the magnetic field perpendicular to the direction of the density gradient, so even a random distribution after being shocked will be preferentially aligned with the shock plane. Since we chose a particularly fortuitous alignment for our simulations, the stronger magnetic fields tend to have smaller inclinations with respect to the shock, and thus are enhanced by shock compression even more relative to the randomly oriented weaker fields; i.e. once the shock has passed through the $-z$ tail at $t = 610.0$ Myr in **M4**, $F(30°) = 61.4\%$ and $F(15°) = 37.3\%$ for all $B$, while $F(30°) = 68.5\%$ and $F(15°) = 42.0\%$ for $B \geq 1$ $\mu$G.

After the shock passes through a tail and the plasma has been compressed, magnetic fields continue to strengthen for 10's of Myr as a result of turbulent flows functioning as coherent dynamos in the immediate aftermath of the shock passage. Turbulence in the tails is not uniform or steady, but eddy speeds of about $\Delta v \approx 450$ km s$^{-1}$ are representative of the turbulent motions. The chaotic and heterogeneous environment in the tails ensures that the shock interaction is not simple and a detailed analysis of the post-shock turbulence is beyond the scope of this work, but the turbulent enhancement obviously increases with the strength of the shock. In our simulations magnetic field amplification ceases and the fields in the $-z$ tail reach maximum strength about 25, 20

and 13 Myr after the shock has completed passage through the tail for the **M2**, **M3** and **M4** cases, respectively. These times correspond to the maximum fluxes observed in our synthetic observations in § 3.4, and are roughly when the CDs have completed traversing the tail and post-shock vortex structures have formed (see § 3.3.2). After running over the first tail, the shock is weakened and very distorted. The interaction with the $+z$ tail is not as clean, and the turbulent flows that develop do not lead to as effective of a turbulent dynamo effect.

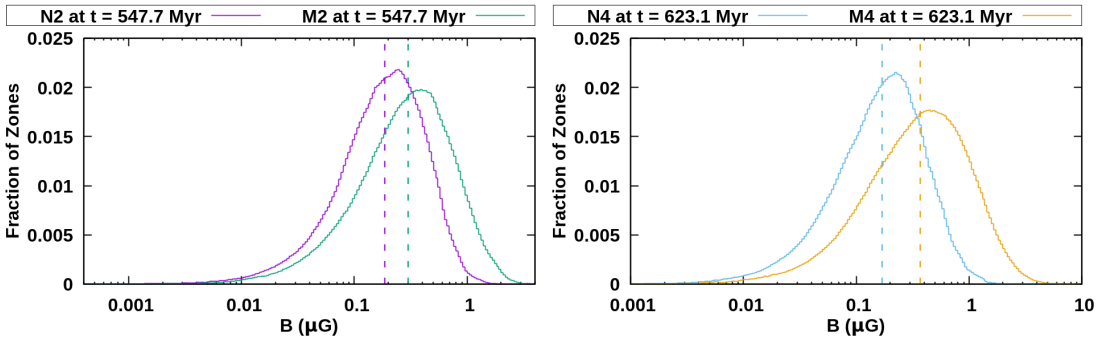


Figure 3.4 Histograms of magnetic field strength for zones in the $-z$ tail with $C_j \geq 0.01$ for shocked and unshocked cases. Zones are sorted into logarithmically spaced bins with 50 bins per dex. The dashed vertical lines show the median for each distribution.

The pre-shock distribution of magnetic field strength is approximately log-normal, after shock passage the distributions are more skewed toward stronger fields. The turbulent amplification has the effect of shifting the distribution to stronger field values, but mostly maintaining the shape of the distribution. Figure 3.4 shows the distributions of field strength in the $-z$ tail when they reach their maximum for the Mach 2 and Mach 4 shocks compared to the distributions at the same timepoints without the shocks. In both unshocked distributions, the ratio of mean strength to median strength is about 1.25, while in **M2** the ratio is about 1.35 and in **M4** it is about 1.45.

It is important to note that the degree of magnetic field strength amplification and the orientation of the fields after the shock passage is transient. Once the amplification has saturated, turbulent flows work steadily to rerandomize the field orientations and diffuse magnetic energy. By $t = 659.2$ Myr in **M4**, the distribution of $F(\phi)$ in the $-z$ tail is roughly $\sin\phi$ for all $B$ as well as just for $B \geq 1$ $\mu$G and the distribution of field strengths has shifted to lower values such that the median is approximately the

pre-shock value. Field strengths for the shocked tails decay slower in **M3** and **M2**, consistent with a turbulence-driven magnetic diffusion.

## 3.4 Analysis of Synthetic Observations of Shocked NAT

We used simulation data to compute and analyze synthetic radio images of synchrotron emission. We created spectral intensity, $I_\nu$, and spectral index, $\alpha_{\nu 1,\nu 2}$, maps using the same redshifted reference frequencies (150 MHz, 325 MHz, 600 MHz, 950 MHz and 1.4 GHz; frequencies are 20% higher in the emission rest frame) and following the same methods as in O'Neill et al. (2019a). We examined intensity and spectral index ($\alpha$) maps at two snapshots in time each from simulations **M2**, **M3** and **M4** (after the shock has passed through the $-z$ tail and after passing through both tails) in figures 3.6, 3.7, 3.9, 3.11, 3.13 and 3.14. Unless otherwise noted, these images are made with the image plane parallel to $x$-$z$ simulation plane (the same plane defined by the jet axis and the wind vector). We also use synthetic images from throughout the **M2**, **M3** and **M4** simulations, as well as complementary images from **N2**, **N3** and **N4**, to compute the time evolution of integrated radio fluxes and spectra in figures 3.5, 3.8 and 3.12.

If a population of CRe is a power law $f(p) \propto p^{-q}$ over a large enough momentum range, then the synchrotron emissivity of that population has a spectral index $\alpha = (q-3)/2$. As outlined in O'Neill et al. (2019a), our CRe are subjected to a mix of energy gains and losses after being released from the AGN source with a power law momentum distribution $f(p) \propto p^{-q_0}$ with $q_0 = 4.5$ (equivalent to $\alpha_0 = 0.75$). The CRe propagate through momentum space in response to compression or expansion in the bulk plasma, losses via synchrotron and inverse Compton (iC) radiation and gains from DSA. We model DSA using the equilibrium test-particle slope of a given shock strength, $q_s = 4M^2/(M^2-1)$. When a zone is shocked, if the pre-shock slope $q_i$ in a given momentum bin is steeper (larger) than $q_s$, the CRe in that bin are redistributed in momentum space with the test-particle slope. Otherwise, they are just subjected to the compressive effects of the shock, i.e., in 1D:

$$\frac{\partial f}{\partial t} = \frac{p}{3}\left(\frac{\partial u}{\partial x}\right)\frac{\partial f}{\partial p}. \tag{3.6}$$

For a negative velocity gradient in the bulk plasma, $\partial u/\partial x$, this has the effect of magnifying and shifting the CRe distribution to higher momenta but maintaining the slope $q_i$, increasing the density of CRe at a particular momentum value (provided the initial distribution $f(p)$ was monotonically decreasing). Neglecting the complications from other gains and losses, we can define an estimated Mach number required for a shock to accelerate CRe capable of emitting synchrotron radiation with an observed spectral index $\alpha$,

$$M(\alpha) = \sqrt{\frac{2\alpha + 3}{2\alpha - 1}}. \tag{3.7}$$

In $\mu$G scale fields, synchrotron radiation at radio frequencies $\nu \sim 0.1$-1 GHz requires CRe with Lorentz factors of roughly $\Gamma_e \sim 10^4$ – $3 \times 10^4$. Following Sarazin (1999), the loss functions, $b(\Gamma_e) = -d\Gamma_e/dt$, for iC and synchrotron radiation have similar functional forms, $b_i(\Gamma_e) \propto \Gamma_e^2 U_i$, where $U_i$ is the energy density of the CMB or the magnetic field. We can thus define a radiative lifetime as a function of energy and an effective magnetic field strength,

$$\tau_{\rm rad} = \frac{\Gamma_e}{b(\Gamma_e)} \approx 107.7 \left(\frac{10^4}{\Gamma_e}\right) \left(\frac{4.77\ \mu{\rm G}}{B_{\rm eff}}\right)^2\ {\rm Myr}, \tag{3.8}$$

where after $\tau_{\rm rad}$ all CRe at or above $\Gamma_e$ will have cooled to lower energies. Here $B_{\rm eff}^2 = B^2 + B_{\rm CMB}^2$ with $B_{\rm CMB} \approx (1+z)^2\ 3.24\ \mu{\rm G} = 4.67\ \mu{\rm G}$ as the equivalent strength of the CMB for our simulated redshift $z = 0.2$. In a 1 $\mu$G magnetic field, $B_{\rm eff} \approx 4.77\ \mu$G, and iC is the dominant cooling mechanism for CRe. After shock compression there are volumes where the field is about 5 $\mu$G, where iC and synchrotron cooling are roughly equal and the CRe lifetimes are cut in half. Fields approaching 10 $\mu$G are attained in **M4**, so the rate of cooling can be increased by a factor of about 5 in these spots, though these amplified fields are relatively short-lived (see § 3.3.3).

We found in O'Neill et al. (2019a) that, observationally, the NAT attains a roughly steady-state morphology once the NAT shape has formed and CRe released during the formation stage have cooled below detectability at our reference frequencies ($t \approx$ 200 Myr). For the duration of the jets' activity, it largely resembles figure 10 in that work, with the extent of the tails (in the $x$-dimension) of $\sim$ 400 kpc at 150 MHz and $\sim$ 300 kpc at 950 MHz. Older tail plasma downstream still contains CRe, but at lower energies incapable of radiating at our reference radio frequncies. Once the

shock front runs over the tails this plasma is able to radiate in radio again, both from reacceleration of CRe to higher energies and from magnetic field amplification shifting the the critical frequency $\nu_c$ of the synchrotron kernel for a CRe with a given energy to a higher frequency ($\nu_c \propto \Gamma_e^2 B_\perp$; see e.g., Rybicki & Lightman, 1979).

### 3.4.1 Synthetic Observations of Mach 2 Interaction

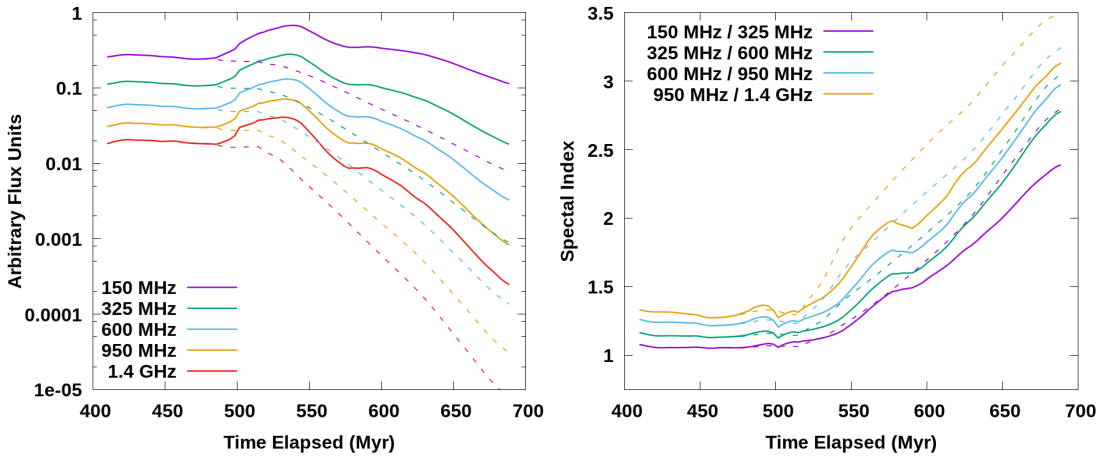


Figure 3.5 Evolution of integrated radio emission, solid lines are from **M2** and dashed lines are from **N2**. Left: Time evolution of integrated fluxes (arbitrary units) at 150 MHz, 325 MHz, 600 MHz, 950 MHz and 1.4 GHz. Fluxes are sampled every 3.279 Myr starting at $t = 409.9$ Myr. Right: Time evolution of integrated spectral indices, $\alpha_{\nu 1,\nu 2}$, between adjacent frequencies on the left, sampled at the same time interval.

The **M2** simulation has the weakest and thus slowest moving shock, so the shock reacceleration of CRe is only mildly able to counteract radiative cooling processes. The merger shock begins to encounter significant amounts of tail plasma around $t \approx 480$ Myr and finishes running over the first tail about 40 Myr later, shortly after the jet turns off at $t = 518.1$ Myr. Once the shock has passed through the $-z$ tail, it continues to brighten for another $\sim 25$ Myr mostly from magnetic fields amplifed via turbulent dynamo (see § 3.3.3), as well as from the shock running over young plasma released from the jet just prior to shutting off. Even while fluxes increase during this time, spectral indices begin to noticeably steepen as reaccelerated CRe resume cooling. The peak brightnesses of the five frequencies plotted in figure 3.5 are not exactly simultaneous

but occur within 7 Myr of each other, peaking first at 1.4 GHz and then at sequentially lower frequencies. Across the spectrum, the peak integrated fluxes in **M2** are about a factor of 3.8 greater than the comparable times in **N2**. From the time evolution of $\alpha$ on the right side of figure 3.5, the integrated spectrum can be seen to mostly maintain the same curvature throughout this first interaction.

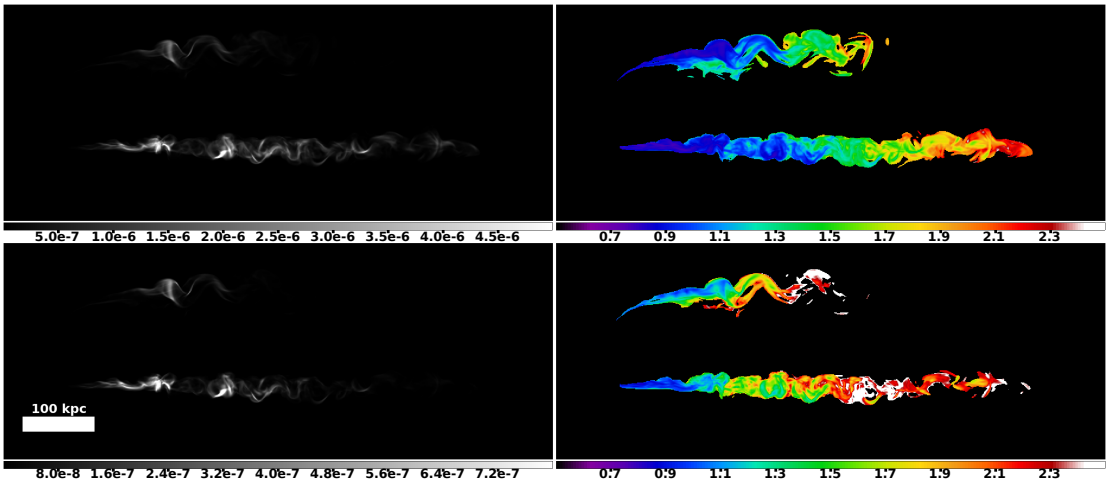


Figure 3.6 Radio images from **M2** at $t = 524.7$ Myr. Top Left: $I_{\nu,150}$. Bottom left: $I_{\nu,950}$. Top right: $\alpha_{150,325}$. Bottom right: $\alpha_{950,1400}$. Intensities are in arbitrary units. Brightest regions have been saturated to reveal fainter features. The $\alpha$ maps include only pixels having $I_\nu$ within a factor 500 of the brightest pixels at the higher frequency.

Figure 3.6 shows intensity and $\alpha$ maps after the shock has run over the $-z$ tail and recently released jet plasma upstream. The intensity maps are highly filamentary and are dominated by two bright spots at both low and high frequencies. The first one consists of the remains of the jet and the disruption zone, where relatively young plasma was in the midst of a disruption event when the shock came through. The other is a collection of filaments about 90 kpc downstream from the first, with enhanced magnetic fields from a previous major disruption event. Both of these bright spots can be identified with clumps of strong magnetic filaments in the unshocked tails on the right side of figure 3.1. Evident from the $\alpha$ maps is a spectral gradient tracing the age of jet plasma among the reaccelerated CRe, suggesting compression is the dominant mechanism and not DSA. Comparing $\alpha$ in the shocked tail with the still luminous portion of the unshocked tail, there is a slight offset consistent with compression shifting

the CRe distributions to higher energies. Individual brighter filaments stand out with slightly flatter spectra relative to adjacent emission as a result of lower energy CRe radiating at the same frequency in comparatively stronger magnetic fields. In the high frequency $\alpha$ map, the furthest downstream emission is actually slightly flatter though $I_\nu$ is relatively weak there since tail plasma there is denser such that the DSA slope of the shock is flatter than the pre-shock slope of the CRe. This corresponds to the dense clump of tail plasma discussed in § 3.3.2 (see figure 3.3). Portions of this clump have the same index of about $\alpha \sim 1.7$ across our reference frequency domain (consistent with DSA) which corresponds to a Mach number of $M \sim 1.6$. The Mach 2 shock has the highest ratio between the shock speed within the tails relative to the shock speed in the ICM (see § 3.3.2), so the tail shock pulls ahead of the merger shock in the ICM by $\sim$ 20 - 40 kpc.

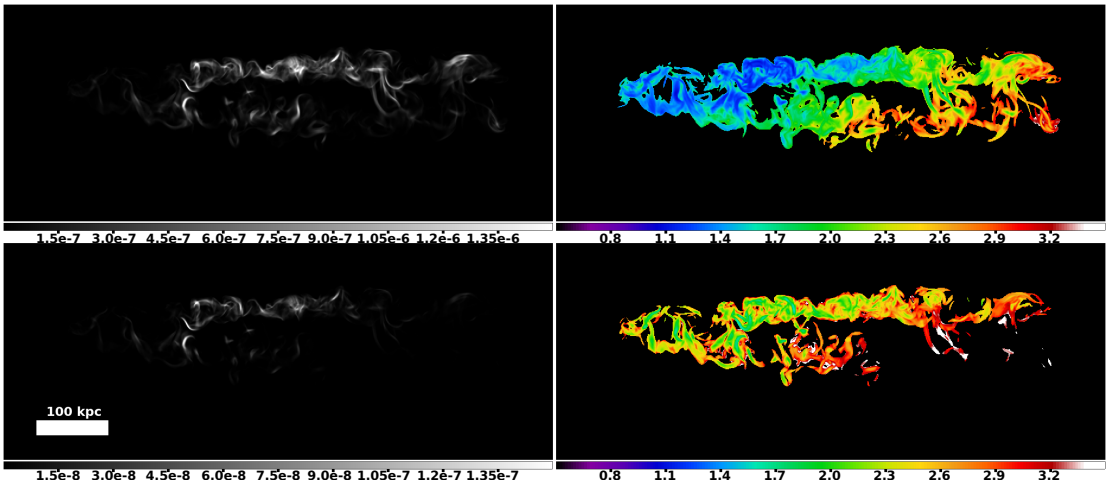


Figure 3.7 Same as figure 3.6 for **M2** at $t = 616.5$ Myr. Note the different color scale for the $\alpha$ maps on account of advanced cooling of the CRe.

After reaching the peak brightness, the cooling trend dominates while the shock is moving through the region between the tails. The highest frequencies (600 MHz and above) fade below their preshock fluxes by 565 Myr. When the shock begins encountering significant amounts of plasma in the $+z$ tail around 575 Myr, the fluxes stabilize and remain roughly constant, with new particle acceleration at the shock balancing radiative losses in the first tail and the as yet unshocked plasma. This pause in the

flux evolution ends once the shock has run through the bulk of the plasma in the upper tail. On the upwind side the unshocked tails are narrower and are composed of large volumes of nearly pristine jet plasma, so the front passes through substantially quicker. The CRe there are younger, still radio luminous and have relatively flat spectra still (at low energies) before the shock, so shocking this plasma accounts for most of the brightening of the interaction between the shock and the $+z$ tail.

By the time of figure 3.7 ($t = 616.5$ Myr), the shock has completely passed through the tails. The brightest patches of the shocked $+z$ tail in the intensity maps are only about a fourth as bright as those in figure 3.6, because the CRe have cooled and magnetic fields diffused in the $+z$ tail for an extra $\sim 100$ Myr prior to shock compression. Intensities are relatively more evenly distributed and not as dominated by a few magnetized filaments. The shock front is slightly weaker after having been curved and distorted by running over the first tail (see § 3.3.2), as a result the tail is not as cleanly and regularly compressed as the $-z$ tail was. The shock has a strength of about $M \sim 1.5$ throughout much of the plasma corresponding to $\alpha = 2.1$. Just prior to being shocked, higher energy CRe in the $+z$ tail have all cooled and the particle population no longer emits at our higher frequencies, so the high frequency emission we see in figure 3.7 is a product of DSA and largely consistent with this slope. The low frequency emission has mostly flatter spectra pre-shock, and an aging gradient is preserved after shock compression. On the downstream side after passing through the $-z$ tail, the shock is highly distorted by the shape of the plume at the end and from pulling far ahead while traversing the bridge between the tails (see figure 3.1), so it is significantly weakened here before encountering the $+z$ tail. As such, the high frequency emission has steeper spectra. The CRe in the $-z$ tail have clearly cooled and enhanced magnetic fields have also diffused in the $\sim 100$ Myr since shock passage, yielding an offset between the spectral gradients of the two tails in the low frequency $\alpha$ map. The few filaments that are still luminous from the shock acceleration have been dispersed and are more randomly oriented. High frequency emission in the $-z$ tail is largely absent aside from the youngest and most magnetized plasma.

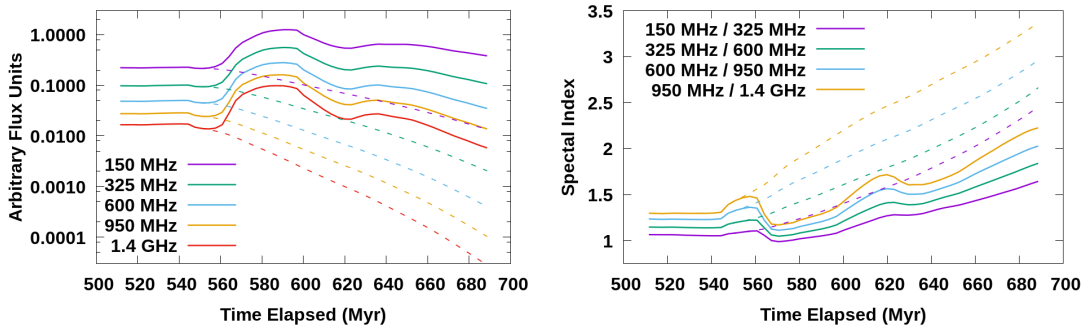


Figure 3.8 Same as figure 3.5 for **M3** and **N3** starting at $t = 508.3$ Myr.

### 3.4.2 Synthetic Observations of Mach 3 Interaction

For **M3**, the shock encounters the first bits of the $-z$ tail just prior to the jets turning off at $t = 546.6$ Myr. The shock begins to run over the bulk of the tail plasma around $t = 550.9$ Myr, where the **M3** and **N3** fluxes begin to deviate in figure 3.8. The shock runs though the tail in $\sim 20$ Myr. During this time the fluxes sharply increase and the spectra flatten at all frequencies, and the integrated spectrum becomes less curved; i.e., $\Delta\alpha$ between $\alpha_{950,1400}$ and $\alpha_{150,325}$ goes from $\Delta\alpha \approx 0.35$ at $t = 550.9$ Myr to $\Delta\alpha \approx 0.18$ at $t = 570.6$ Myr. Strongly magnetized filaments of young plasma around the disruption zone with fields as high as 7 $\mu$G dominate the fluxes with $\alpha_{150,325} \lesssim 0.8$ and $\alpha_{950,1400} \lesssim 1$. The fluxes continue to increase over the next $\sim 20$ Myr as the magnetic field strengths continue to grow. At peak brightness, the fluxes across the spectrum are about a factor of 6 greater than the unshocked NAT, and relative to the same time in **N3** range from a factor of $\sim 10$ greater at 150 MHz to a factor of $\sim 20$ at 1.4 GHz.

The integrated fluxes have essentially plateaued by the time of figure 3.9, $t = 583.7$ Myr, (the true maxima are about 7% brighter at low frequency, and less than 1% brighter at high frequency). The tail is noticeably narrower and more compressed than the shocked tail in figure 3.6. It can be divided into two regions, roughly corresponding to the initial extent of radio emission and the plasma that had ceased radio emission prior to shock reacceleration. The lower energy CRe in the upwind, younger portion of the tail have primarily been re-energized by compression; a subtle gradient is apparent in $\alpha_{150,325}$ up to roughly the middle of the structure. Downwind the average spectra are somewhat more stabilized around $\alpha \sim 1.3$ - 1.5 corresponding to DSA from shocks

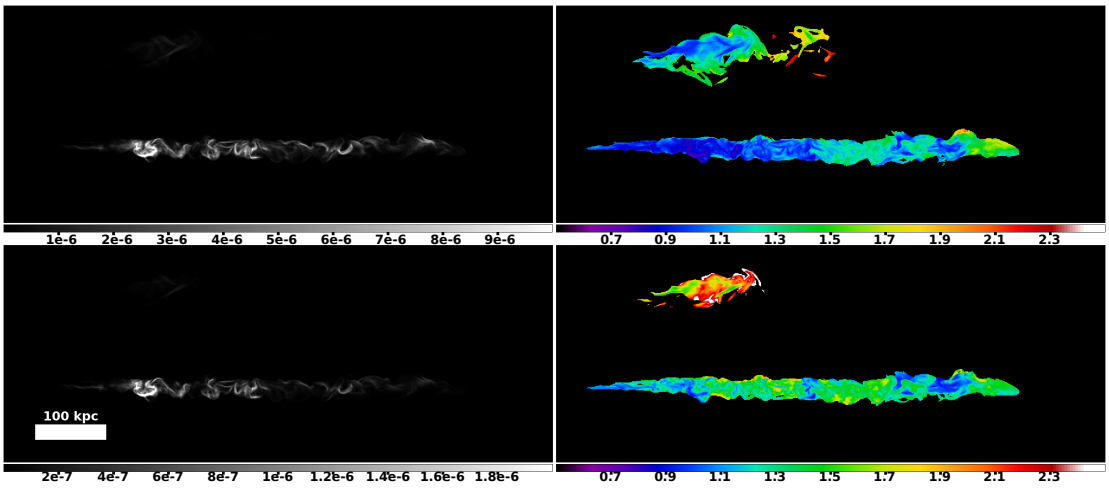


Figure 3.9 Same as figure 3.6 for **M3** at $t = 583.7$ Myr.

with strengths of $M \sim$ 1.7-1.9, with some steeper and flatter patches. For $\alpha_{950,1400}$, the first third of the tail has flat enough spectra pre-shock, such that compression is the dominant acceleration process. The plasma downstream is more consistent with DSA leading to indices mostly in the $\alpha \sim 1.3$ - 1.5 range. One exception is a strongly magnetized filament in the middle of the structure, leading to flatter spectrum emission. Much of the downstream half of the tail is made up of regions with consistent power law spectra across our frequency domain, as a result of shock acceleration by DSA. The patch of flatter spectrum emission with $\alpha \sim 0.9$ (corresponding to a shock strength of $M \sim 2.4$) about 100 kpc from the downstream edge in both $\alpha$ maps is emission from the same dense clump previously mentioned (cf. § 3.3.2 and § 3.4.1). This patch isn't especially bright, magnetic fields here aren't as strong as other regions, but the shock remains relatively strong compared to less dense plasma.

In figure 3.10, we have an $I_{\nu,150}$ map contemporaneous and coaligned to the plots of jet mass in figure 3.3. There are a few regions where the vortex ring morphology is apparent; in the center of the structure on the bottom half there is a coherent ring, and the disruption zone immediately downstream of the jet trail remnants has approximately been transformed into an outer ring and a less well defined, concentric inner ring. It is clear that the emission in much of the structure is segregated into regions of densely entwined magnetic filaments separated by voids mostly lacking in emission. It should

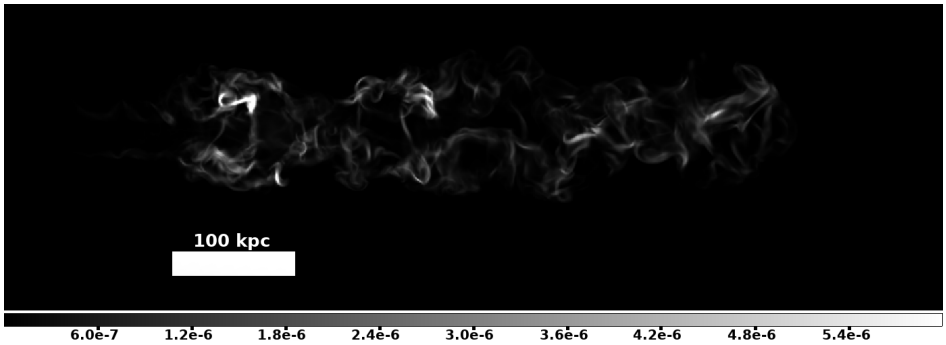


Figure 3.10 $I_{\nu,150}$ at $t = 603.4$ Myr with the image plane parallel to the $x$-$y$ simulation plane. Intensities are in arbitrary units. Brightest regions have been saturated to reveal fainter features.

be noted here our images are exceptionally high resolution, such a morphology would likely require a beam size equivalent to $\lesssim 10$ kpc in order to distinguish.

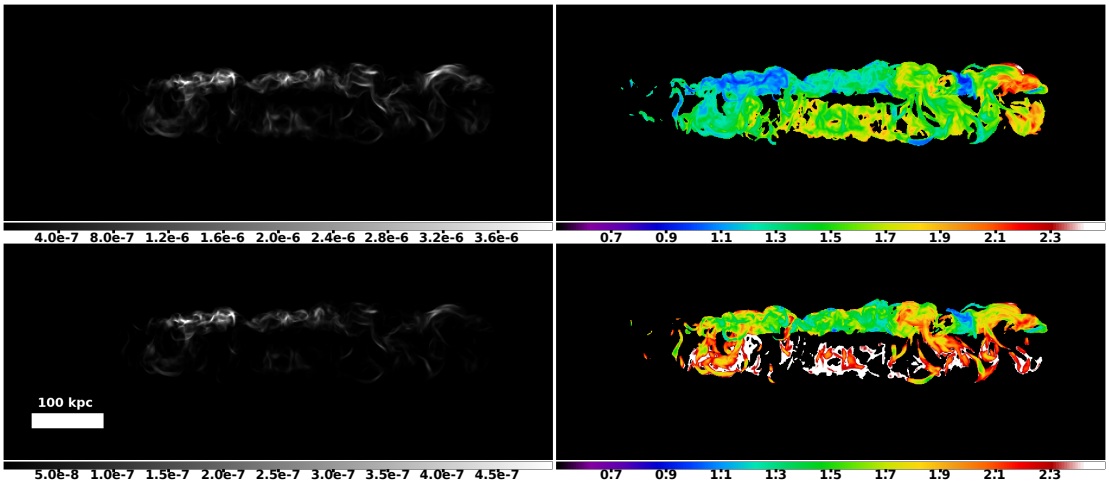


Figure 3.11 Same as figure 3.6 for **M3** at $t = 642.8$ Myr.

After the integrated fluxes reach peak brightness, fluxes sharply decline as magnetic fields diffuse and are randomly reoriented by turbulence (cf. figure 3.8). Spectral indices and spectral curvature increase as well from radiative cooling. The shock begins to run over the the $+z$ tail around $t \sim 620$ Myr. For the first $\sim 15$ Myr of the interaction, the shock counteracts the cooling trend and moderately increases fluxes and decreases spectral curvature across our reference frequencies from $\Delta\alpha = 0.45$ to $\Delta\alpha = 0.31$;

like the $+z$ tail in the **M2** case, this is mostly driven by the upstream plasma being shocked. Figure 3.11 shows the tails as they appear at $t = 642.8$ Myr after the shock has completed running over the whole structure. At 150 MHz, the brightest intensities are about a third of those in figure 3.9 and the integrated flux is about a half the peak reached after the first tail is shocked, while at 1.4 GHz intensities as well as the integrated flux are about a fourth as bright. The plasma in roughly the first third of the $+z$ tail is more pristine, low density jet material so the shock is very weak here. The relatively flatter low frequency emission is merely compressed, while the high frequency emission is accelerated via DSA to spectral indices of $\alpha \sim 1.5$ - 1.9. The central third is shock accelerated at high and low frequencies to slightly flatter indices ($\alpha \sim 1.3$ - 1.7). In the downstream third, aside from another clump of dense plasma leading to relatively flat spectra, much of the plasma is shock accelerated at steeper indices on account of the same distortion in the shock front discussed in § 3.4.1. This distortion is responsible for the relatively crooked, uneven compression compared to the first tail in figure 3.9.

### 3.4.3 Synthetic Observations of Mach 4 Interaction

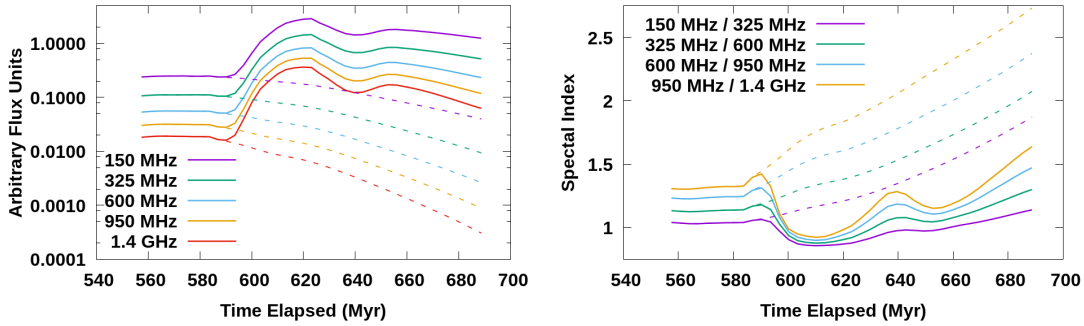


Figure 3.12 Same as figure 3.5 for **M4** and **N4** starting at $t = 557.5$ Myr.

Our **M4** simulation features our strongest, and therefore fastest moving shock. While the interaction in **M2** lasts $\sim$ 145 Myr, the shock here passes through both tails in about $\sim$ 65 Myr. However, magnetic fields are enhanced enough in portions of the tails such that cooling of newly accelerated material does still play a role. The shock begins to encounter the $-z$ tail around $t \sim 590$ Myr and quickly flattens the integrated spectra to about $\alpha \sim 0.9$ across the spectrum (equivalent to a $M \sim 2.4$ shock

acceleration). The curvature drops dramatically from $\Delta\alpha \approx 0.34$ at $t = 590.3$ Myr to $\Delta\alpha \approx 0.07$ at $t = 610.0$ Myr, making the integrated spectrum nearly a constant power law. Steady turbulent amplification of the magnetic fields continues to increase the brightness after the shock completes passage of the $z$ tail until about $t \approx 623$ Myr, while higher frequency emission begins to steepen and the spectrum curves. Compared to the unshocked NAT, the integrated fluxes at maximum brightness are about a factor of 11 greater at 150 MHz and a factor of 19 greater at 1.4 GHz.

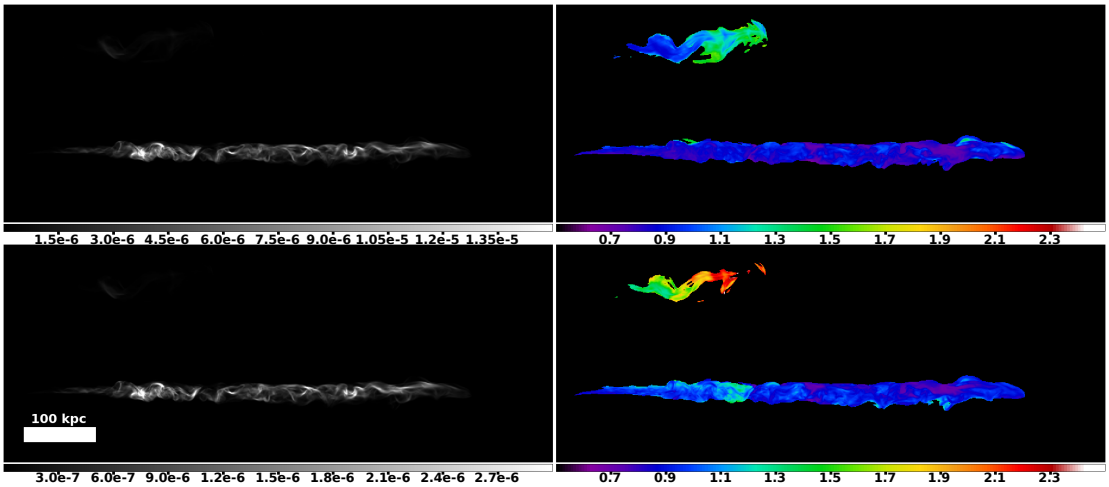


Figure 3.13 Same as figure 3.6 for **M4** at $t = 610.0$ Myr.

In figure 3.13, the shock has just completed running over the tail and compressed it to a maximum width of $\sim 25$ kpc. The brightest spots in the disruption zone dominate the maps of $I_\nu$ (magnetic fields approach 10 $\mu$G in filaments there), while intensities throughout the rest of the tail are fairly consistent averaging about half the brightness of the max intensity in both maps. Again, low densities in the upstream plasma ensure the DSA slope of the shock is steeper than the local CRe populations. Aside from the upstream third of the tail, DSA is the dominant particle acceleration process with consistent spectra between the high and low frequencies. Spectral indices range between $\alpha \sim 0.7$ - 0.9 ($M \approx 2.4$ - 3.3), mostly tracking density variations; this Mach number range is roughly consistent with the modified Mach numbers for density ratios $\delta \approx 0.1$ - 0.5 for a Mach 4 shock (cf. figure 3.2).

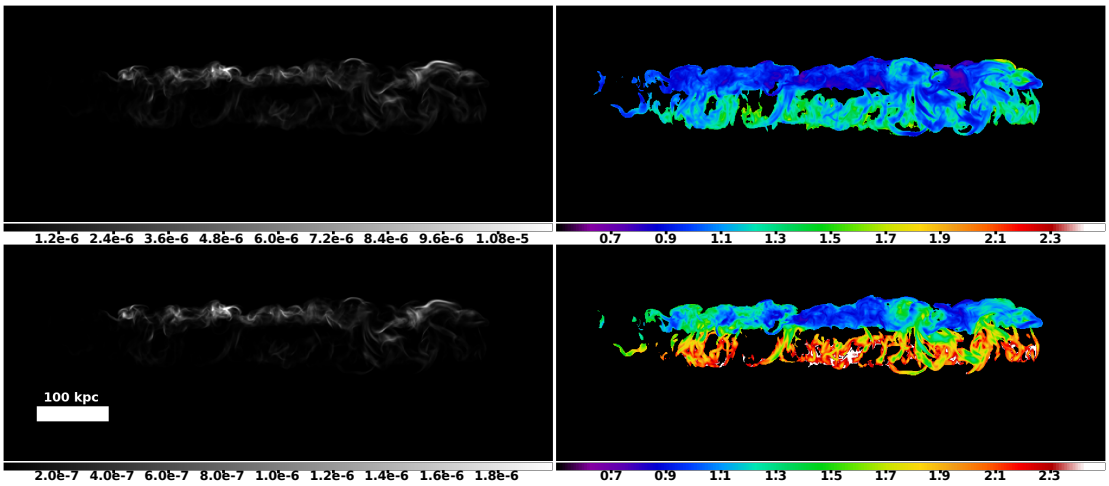


Figure 3.14 Same as figure 3.6 for **M4** at $t = 659.2$ Myr.

After shock passage, the integrated fluxes increase and then suddenly decrease tracking the same magnetic amplification and diffusion seen in **M3** and **M2**, but on a faster timescale (compare figure 3.12 and figure 3.8). The shock begins to run over the $+z$ tail around $t \sim 640$ Myr when radiative cooling and magnetic field decay have increased the spectral curvature such that $\Delta\alpha \approx 0.31$. By $t = 652.6$ Myr the shock has passed through the tail and this drops to $\Delta\alpha \approx 0.18$. In figure 3.14 a few Myr after passing through the whole structure, the compressed $+z$ tail is nearly as narrow as the $-z$ tail is in figure 3.13, but is not as straight and ordered on account of the irregular distorted nature of the shock after passing through the first tail. The patches with highest intensity at 150 MHz are about 80% as bright and at 950 MHz are about 70% as bright as those in figure 3.13. The character of the $\alpha$ maps is largely very similar those in figure 3.11 but with flatter spectra, as a result of the stronger shock and shorter cooling time for the CRe prior to reacceleration.

## 3.5 Summary

In this paper, we have presented a series of simulations studying the interaction between large-scale, weak shock fronts typical of galaxy cluster merger events and the elongated tails composed of cosmic ray electrons (CRe) and warm, low-density plasma released

by a narrow-angle tail (NAT) radio galaxy (RG). Various observations in recent years are suggestive of shocks reaccelerating fossil CRe associated with head-tail RGs, and investigating the interactions between motions in active intracluster media (ICM) and outflows from RGs provides another tool for extracting information about the ICM dynamics at work. In particular, our primary motivation was to explore the possibility that the extended tails of a NAT could provide the seed population potentially necessary to explain the properties of observed cluster radio shocks or radio relics. We utilize 3D MHD simulations with relativistic particle transport and use the results to create synthetic observations of synchrotron emission. This allows us to connect observables to the evolutionary dynamics of the plasma, magnetic fields and CRe particle populations. The principal insights from this investigation are as follows.

1. The heterogeneous character of the plasma that makes up the tails means the strength of our initially uniform merger shock will vary across the length of the tails. In cases where the shocked radio spectral index is a function of the Mach number, this results in spectral properties varying seemingly randomly throughout the shocked tail. This conflicts with observed radio relics with spectra that are very nearly constant across their shock surface and steepen consistently in the post-shock flow. Moreover, as our tails are almost entirely at lower densities than the surrounding ICM, shock strengths in the tails are uniformly weaker than in the ICM. The uneven nature of the tail plasma and the faster propagation speed relative to the ICM means the shock front is highly distorted after passing through the first tail of our NAT, causing certain portions of the shock to be significantly weaker prior to encountering the second tail and making the interaction with the second tail significantly less ordered than the first.

2. The morphology of the tails and their relatively low densities means that our ideally aligned merger shocks drive coherent vortical motions in the shocked tails. These vortical motions have the effect of clearing out much of the midplane of the tail on long enough timelines, and drive a turbulent amplification of the magnetic fields such that strengths continue to grow after shock compression for several Myr. This turbulent dynamo eventually gives way to a turbulent driven diffusion process, causing the magnetic fields strengths to weaken and randomizing their

orientations.

3. The radio intensity of our shocked tails tend to be dominated by one or more regions corresponding to clumps of strong magnetic filaments in the unshocked tails. In our NAT, the magnetic fields reach a maximum in what we dub the disruption zone, where the coherent jet is disrupted and transitions into the mixed tail plasma. The quasi-regular, episodic nature of major disruption events in the evolution of the NAT means relatively strong filaments are spaced out along the length of the tails. After disruption, subsequent random, unsteady turbulent motions drive diffusion of magnetic energy from stronger filaments to the rest of the tail plasma. This diffusion is certainly partly numerical, but also related to the character of turbulence in our simulated tails. The strongly asymmetric quality of the radio brightness in our tails is in contrast to observations of many radio relics. While a few cases have especially asymmetric radio brightness (e.g., Shimwell et al. 2015; van Weeren et al. 2016), some of the more remarkable relics have very consistent intensities across their $\gtrsim$ 1 Mpc lengths (notably the "Sausage"; van Weeren et al. 2010). The intensities in our synthetic observations are exceptionally filamentary (tracing the magnetic field topology), which is consistent with high resolution observations of multiple relics (van Weeren et al., 2019). As the shocked tails radiatively cool, a small number of stronger filaments tend to stand out and persist as the rest of the tail fades to obscurity.

4. The spectral properties in our shocked tails depend on the the strength of the shock involved, as well as multiple difficult to distinguish properties of the tail and the CRe populations. In our **M2** run, the strength of the shock is weak enough in the tails that the simple DSA slope is steeper than the compressed slope of the particle population almost everywhere and the initial aging gradient is preserved in the rejuvenated radio emission. In our stronger shock simulations, the local density of the tail plasma, strength of the magnetic fields and age of the CRe can determine whether the emission we see at a given frequency has spectral properties derived from DSA or the pre-shock particle population. In our simulations we have complete access to the properties that give rise to what we see in our synthetic observations, but in real world situations these effects can be

very hard to discern without complementary information.

This research was supported at the University of Minnesota by NSF grant AST1714205 and through resources provided by the Minnesota Supercomputing Institute. CN was supported by an NSF Graduate Fellowship under Grant 00039202. We acknowledge and appreciate the help and inspiration provided by Larry Rudnick and Avery F. Garon.

# Chapter 4

# Summary of Conclusions & Future Work

## 4.1 Summary

The goal of this dissertation was to use numerical simulations of plasma and relativistic particle outflows characteristic of radio galaxies (RGs) in active galaxy cluster environments in order to analyze the interactions and improve the efficacy of using radio sources as beacons to study the dynamics of the intracluster medium (ICM). To this end, in chapter 2 we performed the first extensive, high-resolution numerical study focused on the development and evolution of a narrow-angle tail (NAT) RG employing 3D magnetohydrodynamics (MHD) with energy-dependent transport of relativistic cosmic ray electrons (CRe). We follow this NAT from its inception as a RG with outflows aligned perpendicular to a strong, persistent wind and track its growth over 100's of Myr. The methods we employ allow us to evaluate the plasma and magnetic field dynamics as well as generate synthetic observations that accurately take into account the energy gains and losses of our particle populations in response to adiabatic bulk plasma flows, shocks and radiative cooling.

We found that our simulated RG goes through an extended formation stage before developing into an obvious NAT morphology. This includes a transient period where the jet growth outpaces the ram pressure induced bending reaction, leading to an appearance more reminiscent of a wide-angle tail radio galaxy with a structure that would lead an

observer to underestimate the magnitude of the ram pressure. We note that once the jets of the RG are sufficiently bent into trajectories roughly parallel to the wind, the jets still actively push downstream. This jet momentum powers the growth of the tails and ensures that they grow faster than than the wind speed throughout the activity of the RG.

We observe that our jets undergo quasi-periodic disruptions in response to turbulent flows induced in the wind by the jets themselves. These disruption events play a major role in the development of the tails and greatly enhance magnetic fields in disrupted jet plasma. We find the regularity of these disruption events and the consistency of the wind lead effectively to a steady-state where observationally, once our NAT is sufficiently developed and plasma released during the early stages is no longer radio-bright, the brightness and spectral properties remain remarkably steady and self-similar until the jets turn off. During this steady-state, the integrated spectrum of our source appears curved, in conflict with the common usage of spectral curvature as an age metric for initially power law sources of emission.

In chapter 3, we used this evolved NAT structure to explore the interaction between its extended fossil CRe populations released over the history of the jets activity and different shocks typical of those found in a cluster as a result of a merger event. Using the same numerical methods, we introduce in separate simulation runs shocks with Mach numbers $M = 2, 3$ and 4 on a boundary such that a planar shock front propagates into the domain with shock normal perpendicular to the wind and the jet axis and the shock sequentially runs over one tail after the other. The primary motivation behind this experiment is to investigate the potential that fossil CRe from a NAT could serve as the seed population for a radio relic.

We utilized a model based on a 1D analytical treatment to examine the nature of the shock front throughout the heterogeneous, lower density tail plasma and found measured shock strengths are largely in agreement. This model is also generally consistent qualitatively with the development of vortical motions that effectively sweep material out of the midplane of the tails on long enough timescales. These vortical motions also generate an ordered turbulent dynamo that works to enhance magnetic field strengths in tail plasma even after the shock front has completed passing through. These ordered turbulent flows eventually give way to disordered turbulence that quickly diffuses

enhanced magnetic fields.

We found the variable state of the plasma and CRe populations throughout the extent of our unshocked tails imprints inhomogeneous emission properties that are mostly inconsistent with observed radio relics. The brightness distribution of our shocked tails are highly asymmetric, dominated largely by plasma in the disruption zone that preshock is host to exceptionally strong magnetic fields. The plasma in our tails exhibits large variations in density from one location to another, which causes shock strength to vary greatly across the length of the shock. Observed radio relics tend to have very consistent spectral properties, while the variations in shock strength through our tails lead to large spectral variations atypical of radio relics.

## 4.2 Future Directions

There are many directions future work can take to expand on what has been accomplished in this dissertation.

The diffusivity of magnetic field strengths in our results is driven by turbulence in the simulation, but may be excessively amplified by numerical diffusivity inherent to the methods used. The TVD solver used to integrate the fluid state is dependent on a set of input user-defined dissipation constants which moderate fluxes along characteristics of the Riemann problem solved at each zone interface. Performing similar tests with different dissipation constants may have a noticeable effect on the evolution of the magnetic field. Alternatively, the newest version of the WOMBAT code used in this work is currently under development, and employs a higher-order solver for roughly the same computational cost. This may produce different, more accurate solutions if run with the same problems investigated here.

The obvious extension of the work in chapter 2 is to use a less idealized environment in which to evolve the NAT; embed a RG in a more realistic or more "interesting" ICM flow. In chapter 2, we used a constant, homogeneous wind flow across the RG jet axis, and a background containing no magnetic fields, in order to isolate the effects of the NAT-wind interplay. The consequences of turbulence or density inhomogeneities in the background wind on the development of the NAT, along with randomized background

magnetic field distributions, would be interesting to investigate. Also utilizing a time-dependent wind, where the NAT evolves in a consistent wind until some time, after which the wind flows in from another direction, in order to mimic changes in the bulk flow surrounding the RG would be an intriguing, realistic scenario to simulate.

Given that many of the discrepancies in chapter 3 between our shocked NAT and observed properties of radio relics emerge from the inhomogeneous state of the tail plasma and particle populations pre-shock, it would be interesting to evolve our NAT in roughly the same manner, then turn off the jets and allow the tails to evolve, mix more thoroughly with the background ICM and smooth out the variations prior to introducing a shock. This could be done with a larger computational domain, or perhaps more plausibly with an initially stationary background and a NAT generated by moving an AGN source across the grid. Additional scenarios involving shocks entering from different directions or moving at angles with respect to the NAT, as well as shocks that enter the domain with magnetic fields in their post-shock flow, shocks with relativistic particle injection at the shock front, along with fully consistent diffusive shock acceleration with non-passive CRe populations would be interesting ways to build upon the work done here.

# References

Balsara, D. & Norman, M. L., 1992, ApJ, 393, 631

Begelman, M. C., Rees, M. J. & Blandford, R. D., 1979, Nature, 279, 770

Bicknell, G. V., 1994, ApJ, 422, 542

Bodo, G & Tavecchio, F. 2018, A&A, 609, A122

Bonafede, A., Intema, H T., Brueggen, M., Girardi, M., Nonino, M., Kantharia, N., van Weeren, R. J. & Roettgering, H. J. A., 2014, ApJ, 785, 1

Brüggen, M., Bykov, A., Ryu, D., & Röttgering, H., 2012, Space Sci. Rev., 166, 187

Brunetti, G. & Jones, T. W., 2015, IJMPD, 23, 1430007-98

Brunetti, G. & Lazarian, A., 2011, MNRAS, 412, 817

Burns, J., Owen, F., Rudnick, L. & Greisen, E., 1979, ApJ, 229, 590

Clarke, A. O., Scaife, A. M. M., Shimwell, T., van Weeren, R. J., Bonafede, A., Heald, G., Brunetti, G., Cantwell, T. M., de Gasperin, F., Brüggen, M., Botteon, A., Hoeft, M., Horellou, C., Cassano, R., Harwood, J. J. & Röttgering, H., 2019, arXiv:1906.07792

de Gasperin, F., Intema, H. T., Shimwell, T. W., Brunetti, G., Brüggen, M., Enßlin, T. A., van Weeren, R. J., Bonafede, A. & Röttgering, H., 2017, Science Advances, 3, e1701634

Di Gennaro, G., van Weeren, R. J., Hoeft, M., Kang, H., Ryu, D., Rudnick, L., Forman, W., Röttgering, H. J. A., Brüggen, M., Dawson, W. A., Golovich, N., Hoang, D. N., Intema, H. T., Jones, C., Kraft, R. P., Shimwell, T. W. & Stroe, A., 2018, ApJ, 865, 24

Gan, Z., Li, H., Li, S. & Yuan, F., 2017, ApJ, 839, 14

Garon, A., Rudnick, L., Wong, O. I., Jones, T. W., Kim, J., Andernach, H., Shabala, S., Kapinska, A. D., Norris, R. P., de Gasperin, F., Tate, J. & Tang, H., 2019, AJ, 157, 17

Ha, Ji-Hoon, Ryu, D. & Kang, H., 2018, ApJ, 857, 26

Heinz, S., Brueggen, M., Young, A. & Levesque, E. 2006, MNRAS, 373, 65

Hoang, D. N., Shimwell, T. W., Stroe, A., et al, 2017, MNRAS, 471, 1107

Jones, T. W. & Kang, H., 2005, Astropart. Phys., 24, 75

Jones, T. W., Nolting, C., O'Neill, B. J. & Mendygral, P. J. 2017, Physics of Plasmas, 24, 41402

Jones, T. W. & Owen, F. N., 1979, ApJ, 234, 818

Kang, H. & Ryu, D., 2016, ApJ, 823, 13

Kang, H., Ryu, D., Cen, R., & Ostriker, J. P. 2007, ApJ, 669, 729

Laing, R. & Bridle, A., 2008, "Extragalactic Jets: Theory and Observation from Radio to Gamma Ray," (ASP Conference Series, Vol 386) (T. Rector & D. De Young, Eds.) p 70

Loken, C., Roettiger, K., Burns, J. & Norman, M. 1995, ApJ, 445, 80

Lynn, W. L., Quataert, E., Chandran, B. & Parrish, I., 2014, ApJ, 791, 71

Markevitch, M. & Vikhlinin, A., 2007, Phys. Rep., 443, 1

McNamara, B.R. & Nulsen, P.E.J., 2007, ARA&A, 45, 117

Mendygral, Peter John. (2011). PhD thesis. Simulations and Synthetic Observations of Active Galactic Nuclei Jets in Galaxy Clusters: Numerical Tools and Experiments.. Retrieved from the University of Minnesota Digital Conservancy, http://hdl.handle.net/11299/113253

Morsony, B., Miller, J. J., Heinz, S., Freeland, E., Wilcots, E. Brueggen, M. & Ruszkowski, M. 2013, MNRAS, 431, 781

Mroczkowski, T., Nagai, D., Basu, K., Chluba, J., Sayers, J., Adam, R., Churazov, E., Crites, A., Di Mascolo, L., Eckert, D., Macias-Perez, J., Mayet, F., Perotto, L., Pointecouteau, E., Romero, C., Ruppin, F., Scannapieco, E. & ZuHone, J., 2019, Space Sci. Rev., 215, 17

Miniati, F., Jones, T. W., Kang, H. & Ryu, D., 2001, ApJ, 562, 233

Morsony, B. J., Miller, J. J., Heinz, S., Freeland, E., Wilcotts, E., Bruggen, M., Ruszkowski, M., 2013, MNRAS, 431, 781

Nelson, D., Springel, V., Pillepich, A., Rodriguez-Gomez, V., Torrey, P., Genel, S., Vogelsberger, M., Pakmor, R., Marinacci, F., Weinberger, R., Kelley, L., Lovell, M., Diemer, B. & Hernquist, L., 2019, Computational Astrophysics and Cosmology, 6, 2

Nolting, C., Jones T. W., O'Neill, B. J. & Mendygral, P. J., 2019, ApJ, 876, 154

Nolting, C., Jones, T. W., O'Neill, B. J. & Mendygral, P. J., 2019 ApJ (in preparation)

Norman, M. L., Smarr, L., Winkler, K-H. & Smith, M. D., 1982, A&A, 113, 285

O'Neill, B. J., Jones, T. W., Nolting, C. & Mendygral. P. J., 2019, ApJ (in preparation)

O'Neill, B. J., Jones, T. W., Nolting, C. & Mendygral. P. J., 2019 ApJ (in preparation)

Owen, F. N., Rudnick, L., Eilek, J., Rau, U., Bhatnagar, S. & Kogan, L., 2014, ApJ, 794, 24

Pacholczyk, A. G. 1970, Radio astrophysics: Nonthermal Processes in Galactic and Extragalactic Sources

Perucho, M., 2013, arXiv:1308.6168v2

Pizzo, R. F. & de Bruyn, A. G., 2009, A&A, 507, 639

Porter, D. H., Mendygral, P. J. & Jones, T. W., 2009, AIPC, 1201,259

Pfrommer, C. & Jones, T. W., 2011 ApJ, 730, 22

Rudnick, L. & Owen, F. N., 1977, AJ, 82, 1

Russell, H. R., van Weeren, R. J., Edge, A. C., McNamara, B. R., Sanders, J. S., Fabian, A. C., Baum, S. A., Canning, R. E. A., Donahue, M. & O'Dea, C. P., 2011, MNRAS, 417, L1

Rybicki, G. & Lightman, A., 1979, "Radiative Processes in Astrophysics," Ch 6 (John Wiley & Sons) (New York)

Ryu, D., & Jones, T. W., 1995, ApJ, 442, 228

Ryu, D., Miniati, F., Jones, T. W. & Frank, A., 1998, ApJ, 509, 244

Ryu, D., Kang, H., Hallman, E. & Jones, T. W., 2003 ApJ, 593, 599R

Sarazin, C. L., 1999, ApJ, 520, 529S

Schuecker P., Finoguenov A., Miniati F., Böhringer, H. & Briel, U. G., 2004, A&A, 426, 387

Shimwell, T. W., Brown, S., Feain, I. J., Feretti, L., Gaensler, B. M. & Lage, C., 2014, MNRAS, 440, 2901

Shimwell, T. W., Markevitch, M., Brown, S., Farrar, G. R., Feretti, L., Gaensler, B. M., Johnston-Hollitt, M., Lage, C. & Srinivasan, R., 2015, MNRAS, 449, 1486

Simionescu, A.,ZuHone, J., Zhuravleva, I., Churazov, E., Gaspari, M., Nagai, D., Werner, N., Roediger, E., Canning, R., Eckert, D., Gu, L. & Paerels, F., 2019, Space Sci. Rev., 215, 24

van Weeren, R. J., Röttgering, H. , Brüggen, M. & Hoeft, M. 2010, Science, 330, 347

van Weeren, R. J., Brunetti, G., Brggen, M., et al., 2016, ApJ, 818, 204

van Weeren, R. J., Andrade-Santos, F., Dawson, W. A., Golovich, N., Lal, D.V., Kang, H., Ryu, D., Brueggen, M., Ogrean, G. A., Forman, W. R., Jones, C., Placco, V. M., Santucci, R. M., Wittman, D., Jee, M. J., Kraft, R. P., Sobral, D., Stroe, A. & Fogarty, K., 2017, Nature Astronomy, 1, 5

van Weeren, R. J., de Gasperin, F., Akamatsu, H., Brüggen, M., Feretti, L., Kang, H., Stroe, A. & Zandanel, F., Space Sci. Rev., 2019, 215, 16

Williams, A. G. & Gull, S. F., 1984, Nature, 310, 33

# Appendix A

# Chapter 2
# A Fresh Look at Narrow-Angle Tail Radio Galaxy Dynamics, Evolution and Emissions

## A.1 Modeling NAT Head Jet Trajectories

Here we outline and compare with simulations a simple, but flexible formalism for modeling the approximate, steady-state trajectories near their source of supersonic jets propagating in a crosswind for an arbitrary orientation between the jet flow at its source and the wind flow. The formalism is consistent with the classic jet bending treatment for orthogonal crosswinds Begelman et al. (1979); Jones et al (2017), but, because jet-wind alignments can take any orientation, and because 3D simulations reveal rather complex flow dynamics near the jets in this situation, the formalism is generalized and designed for easy empirical tuning. For simplicity, the jet velocity is assumed to have constant magnitude, $v_j$, while the direction of the jet flow, $\hat{v}_j$, is deflected by pressure gradients across the jet set up by the wind flow.

We apply a Cartesian coordinate system similar to that in the main text of this paper, in which the upwind, unperturbed wind has velocity $\vec{v}_w = v_w\hat{x}$, with an unperturbed

wind density, $\rho_w$. We express the interactions in terms of a uniform wind and steady jet sources, but because the model is "local" it is, in principle, straightforward to extend to nonuniform winds and time varying jet sources. We assume the jets emerge from their source with velocity, $\vec{v}_j = v_j(\cos\theta_{ji}\hat{x} + \sin\theta_{ji}\hat{z})$, with $i = 1, 2$ to account for two jets and with $0 \leq \theta_{ji} < 2\pi$. Thus, for $\theta_{ji} = 0$ ($\pi$) an emergent jet and the wind are aligned and parallel (anti-parallel), while for $\theta_{ji} = \pi/2,\ 3\pi/2$, the jet and wind flows are orthogonal. We assume for simplicity that the jet density, $\rho_j$, and jet radius, $r_j$, are constant along the jet; only the direction, $\theta$, of $\hat{v}_j$ varies as the jets propagate. Except at its source we hereafter drop the subscript $j$ from the jet propagation direction, $\theta$. That is, $\theta_{ji}$ always refers to a jet as it is launched. The first index, $j$, indicates a launching jet, while the second index, i = 1,2, discriminates between the two jets. In our model and its test simulations we include jet pairs satisfying $\theta_{j2} = \theta_{j1} + \pi$.

The incidence of a crosswind on a jet leads to a pressure enhancement on the upwind side of the jet relative to the downwind side. This pressure drop across the jet deflects the jet trajectory towards the downwind direction. For consistency with our assumption that the jet speed, $v_j$, is constant, we assume in our simple model that the pressure gradient induced by the crosswind is perpendicular to the local jet axis and in the jet-wind plane; that is in the direction $\hat{a}_\perp = \pm(\sin\theta\hat{x} - \cos\theta\hat{z})$, where the upper (lower) sign applies for $0 < \theta < \pi$ ($\pi < \theta < 2\pi$). Even though wind density and pressure distributions near the jets in our simulations are neither simple nor really steady, we still expect on average that the magnitude of the effective pressure gradient will scale approximately with the wind ram pressure, $\rho_w v_w^2$, and inversely with the jet radius, $r_j$, with allowance for influence of projection through $\theta$. We combine these considerations to produce an estimate for the effective pressure gradient across the jet, $\alpha\rho_w v_w^2 f(\theta)/r_j$, where $\alpha \sim 1$ is a parameter, perhaps somewhat dependent on the specific situation, while $f(\theta)$ is a function we will define below intended to account for local jet orientation with respect to the wind flow. Then the acceleration of jet plasma normal to its propagation is $|a_\perp| \approx \alpha\rho_w v_w^2 f(\theta)/(r_j\rho_j)$.

Using the above relations we can estimate an effective local bending radius for the jet, $R \approx\ v_j^2/|a_\perp| \approx\ \ell_b/(\alpha f(\theta))$ where we have defined $\ell_b$ as a characteristic "*bending length*",

$$\ell_b = r_j \frac{\rho_j v_j^2}{\rho_w v_w^2}. \tag{A.1}$$

We prefer the term "bending length" as a somewhat more appropriate concept in describing our model jet trajectories than "bending radius," since the trajectories are not generally circular arcs. Since, however, the effective acceleration is assumed normal to the local jet flow, we can use these results to establish the relation for the rate in time at which the local jet flow is deflected,

$$\frac{d\theta}{dt} = \pm\frac{\alpha v_j}{R} = \pm\frac{v_j}{\ell_b} f(\theta). \tag{A.2}$$

The upper (lower) sign applies when the deflection is clockwise (counter clockwise). Since we generally start with pairs of oppositely directed jets, $\theta_{j2} = \theta_{j1} + \pi$, unless $\theta_{j1} = 0$, we have one jet bending clockwise ($d\theta/dt > 0$) and one bending counter clockwise ($d\theta/dt < 0$). Since $dx/dt = -v_j \cos\theta$ and $dz/dt = v_j \sin\theta$, we can use equation A.2 to determine the trajectory of the jet in terms of $\theta$ as

$$x' - x'_j = \frac{x - x_j}{\ell_b} = -\frac{1}{\alpha}\int_{\theta_j}^{\theta} \frac{\cos\theta}{f(\theta)} d\theta = -\frac{1}{\alpha}\int_{\sin\theta_j}^{\sin\theta} \frac{d\sin\theta}{f(\theta)} = -\frac{1}{\alpha} I_x(\theta, \theta_j), \tag{A.3}$$

$$z' - z'_j = \frac{y - y_j}{\ell_b} = \frac{1}{\alpha}\int_{\theta_j}^{\theta} \frac{\sin\theta}{f(\theta)} d\theta = \frac{1}{\alpha} I_z(\theta, \theta_j), \tag{A.4}$$

where $(x_j, z_j)$ represents the jet source coordinates, and we have introduced the bending length normalized coordinates, $x' = x/\ell_b$, $z' = y/\ell_b$, while $I_x$ and $I_z$ encode the dependence of the model on $f(\theta)$. For the trivial, but unphysical case, $f(\theta) = 1$, $I_x = \sin\theta - \sin\theta_j$, $I_z = \cos\theta_j - \cos\theta$, and the trajectory becomes a circle of radius, $R' = R/\ell_b = 1/\alpha$, as one would expect. In interpreting equations A.3 and A.4 we should keep in mind that according to the conditions outlined above $\theta - \theta_j$ can be positive or negative.

Physically, we would expect the induced normal force to increase as the jet and wind flows become more nearly orthogonal; that is, as $|\hat{v}_j \times \hat{v}_w| = |\sin\theta|$ increases. Although we are not aware of any generally applicable physical form for $f(\theta)$, the simple form $f(\theta) = |\sin\theta^n|$ with $n = 1, 2, 3, ...$ provides a convenient, physically consistent form that is also easy to integrate to obtain $I_x$ and $I_z$. It is intuitively obvious that smaller values for $n$ lead to more sharply bent jets than larger values for $n$. Quantitatively the forms become, for $n = 1$, $I_x = \ln(\sin\theta/\sin\theta_{ji})$, $I_z = (\theta - \theta_{ji})$,

for $n = 2$, $I_x = (1/\sin\theta_{ji} - 1/\sin\theta)$, $I_z = \ln(\tan\theta/2/\tan\theta_{ji}/2)$, and for $n = 3$, $I_x = (1/2)\left[1/(\sin\theta_{ji})^2 - 1/(\sin\theta)^2\right]$, $I_z = (\cot\theta_{ji} - \cot\theta)$.

Figure A.1 illustrates the solutions to equations A.3 and A.4 for $\theta_{j1} = 90°, 45°, 30°$ and $15°$ with $n = 1, 2, 3$. The red curve and data points in each panel show the jet trajectories from 3D MHD test simulations for each $\theta_{j1}$, $\theta_{j2}$ in the domains where they remained steady in time after the jet termini extended into the tail regions. As discussed in §2.3.1, when jets in our simulations became strongly bent, they developed intermittent "flapping" behaviors, even though they typically remained coherent well into the tails. For each jet orientation and $n$ the $\alpha$ parameter in the plotted curve in Figure A.1 was set to yield the best empirical fit to simulation data with the same $\ell_b$ and $\theta_{j1}$. In general $1 \lesssim \alpha \lesssim 1.3$, with $\alpha$ increasing slowly from $\theta_{j1} = \pm\pi/2$ as $\theta_{j1} \to 0$. For validation, figure A.2 shows snapshot 2D views from simulated flows used to trace jet trajectories in the $\theta_{j1} = 45°$ and $\theta_{j1} = 30°$ orientations shown in figure A.1. Analogous simulation behaviors for $\theta_{j1} = 90°$ are available, for example, in figure 2.3 and for $\theta_{j1} = 15°$ in (Nolting et al., 2019a).

We conclude that these simple jet trajectory models provide reasonable matches to our simulation results over wide a range of jet orientations, with parameters $n \sim 2$ and $\alpha \gtrsim 1$, but caution that past the point where a jet has been deflected by $\Delta\theta \gtrsim \pi/2$ jet trajectories tend to be quite unsteady. Even then, the time average behaviors match the models reasonably well. Beyond what we show here, we have conducted multiple simulation tests in which we varied individual parameters, including jet density, $\rho_j$ and velocity, $v_j$, as well as wind density, $\rho_w$ and velocity, $v_w$. The steady jet trajectories cited here were robust, so long as they were expressed in terms of the normalized scales, $x'$ and $z'$ defined in this Appendix.

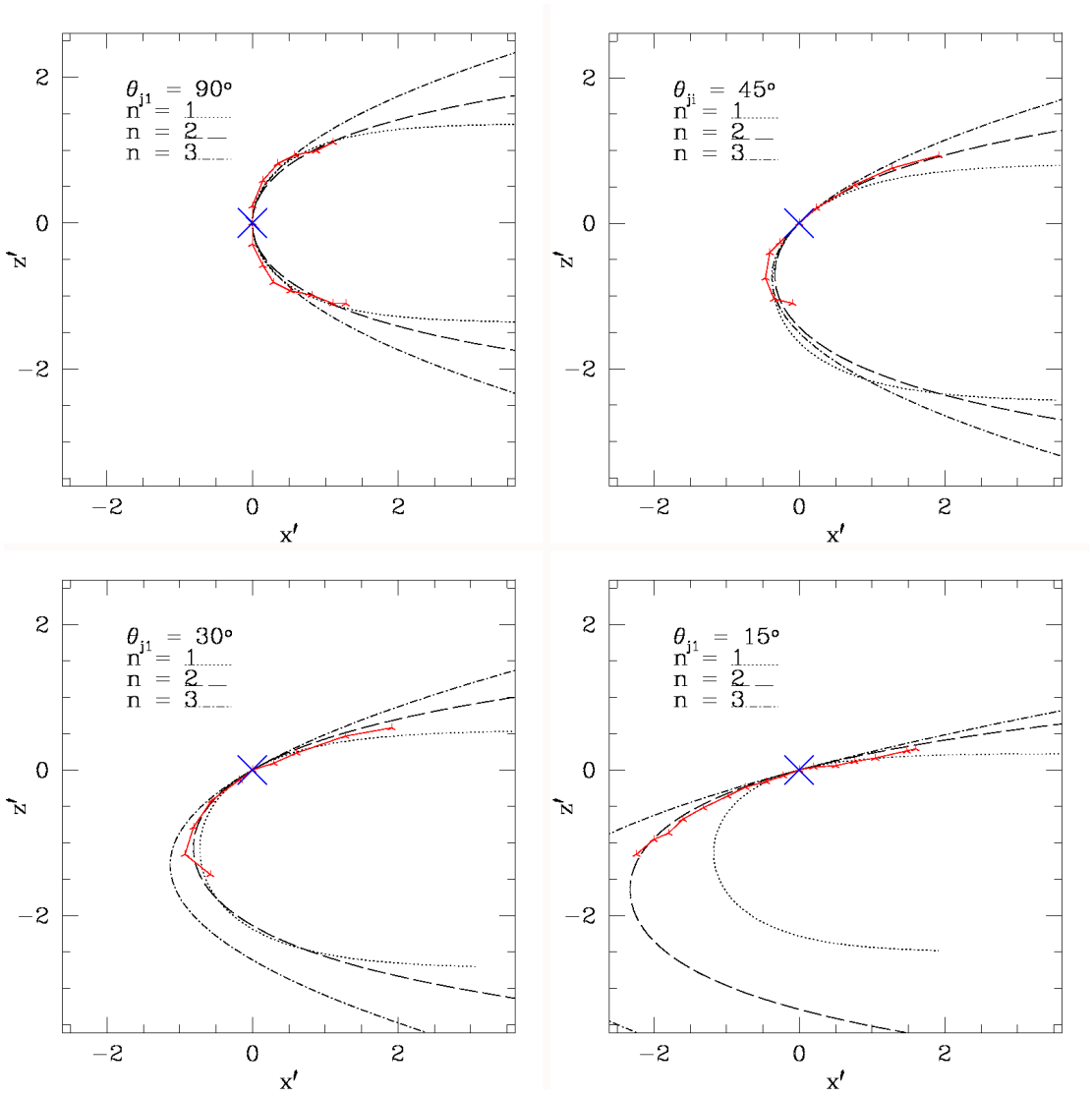


Figure A.1 Shapes in normalized coordinates, $x'$, $z'$ computed using equations A.3 and A.4 with $f(\theta) = |\sin\theta^n|$ with $n = 1, 2$ and 3 (black curves). The ram pressure efficiency factor, $1 \lesssim \alpha \lesssim 1.3$, depending on both $\theta_{ji}$ and $n$. The jet source is marked with an 'X'. Red points and curves trajectories measured from 3D MHD simulations similar to those described in §2.2 over portions of the "head region"empirically deemed quasi-steady after jets had propagated beyond the head into the tails.

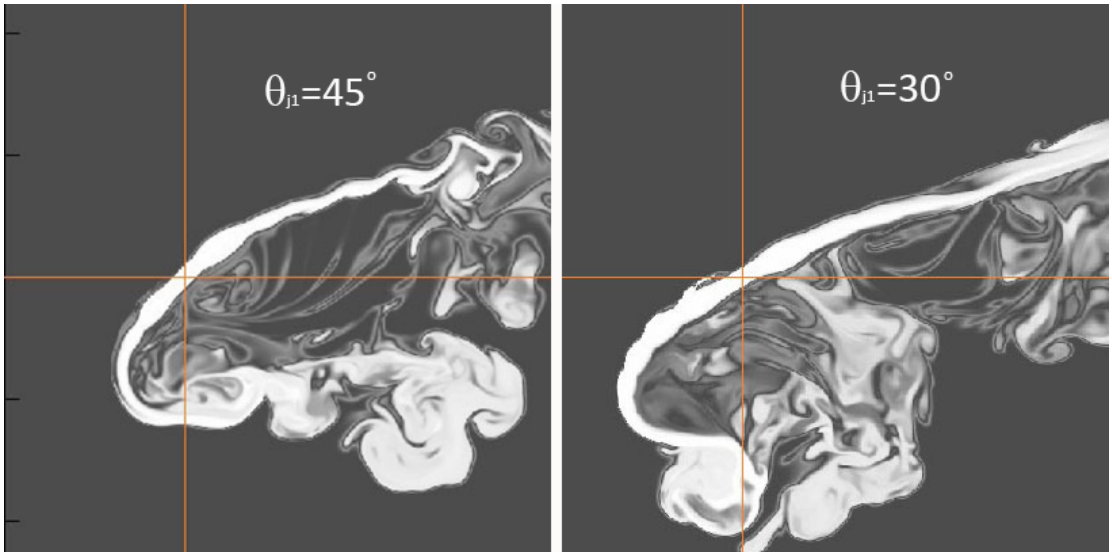


Figure A.2 2D (x-z plane) slices showing $C_j$ in two 3D MHD simulations used in comparing the model trajectories shown in Figure A.1. Cross hairs identify the jet source center. Simulation jet trajectory coordinates shown in Figure A.1 were measured from the ends of the jet launch cylinder to the center of the propagating jet.